UNIVERSITÀ DEL SALENTO

DIPARTIMENTO DI FISICA

DOTTORATO DI RICERCA IN FISICA – XXII CICLO

Off-line monitoring and data quality of Resistive Plate Chambers for the ATLAS experiment

Supervisors:
Prof. Edoardo Gorini
Dr. Gabriele Chiodini

Candidate:
Angelo Guida

Thesis submitted for the degree of Doctor of Philosophy

Io stimo più il trovar un vero,
benché di cosa leggiera,
che 'l disputar lungamente delle massime questioni
senza conseguir verità nissuna.

G. Galilei

Contents

Introduction

This thesis describes the developed software, the experimental techniques and the analysis results for monitoring and assessing data quality of ATLAS RPC trigger chambers.

ATLAS is an experiment currently running at the Large Hadron Collider (LHC) at CERN laboratory, in Geneva. LHC is the most energetic accelerator in the world. Its main features are three: *Luminosity*, and *Energy*. The LHC accelerator is designed to provide proton-proton collisions at the center of mass energy of 14 TeV at a luminosity of $10^{34} cm^{-2} s^{-1}$ with a bunch crossing rate of $25 ns$. At the time of writing it is providing collision at half of design energy but almost a factor of four higher than achieved in previous accelerators.

The main physics goal of the ATLAS experiment is the discovery of the Higgs boson. In the theoretical frame of the Standard Model the Higgs boson is responsible of the observed mass of elementary particles. In addition, ATLAS has a large capability to discover *new physics*, as for example *super-symmetric* particles, exploring the TeV energy scale range.

One of the two major experiments installed at the LHC is the ATLAS detector. It is a general purpose experiment designed to cover the full range of the physical processes that will be produced by LHC collisions. It is composed of several subdetectors with very well defined purpose: a central tracking system to reconstruct and define charged particle trajectories near the interaction point, a calorimetric system to measure energy and direction of electron, photon and hadronic particles and an air core muon spectrometer to identify muons and measure their momentum.

High momentum muon final states are amongst the most promising and robust signature of physics at LHC. To exploit this potential, the ATLAS Collaboration has designed a high-resolution muon spectrometer with stand-alone triggering and momentum measurements capability over a wide range of transverse momentum. The ATLAS muon spectrometer consist of muon chambers for precision measurements and dedicated fast muon detector to provide information muon candidates (*Trigger signal*). As described in the second chapter of this thesis, the trigger chambers are made of Resistive Plate Chambers (RPCs) in the barrel region and of Thin Gap Chamber (TGCs) in the end-cap regions. The ATLAS Lecce group, to which I belong, was involved in the production and test of the RPC chambers.

RPCs are gaseous detector providing typical space-time resolution of $1\,cm \times 1\,ns$.

In this work I developed the software and the technique to monitor offline the RPC detector. In addition, I implemented the algorithms to determine the data quality of the RPC detector during data taking. Finally, I applied the described tools during all ATLAS commissioning phase and cosmic runs to debug and characterize the RPC detector in the cavern.

The dissertation is organized in six chapters:

- Chapter 1: **The standard model of elementary particles** summarize the Standard Model theory and in particular the spontaneous symmetry breaking with the Higgs boson mass constraints coming from theory and experiments. An introduction to the physics beyond the Standard Model such as Supersimmetry is given. The possible experimental signatures of the Higgs boson in the SM framework are also presented.

- Chapter 2: **The ATLAS experiment at Large Hadron Collider** gives an overview of the Large Hadron Collider machine and a description of the ATLAS experiment with all its sub-detector. More emphasis is given to the Muon Spectrometer system.

- Chapter 3: **ATLAS RPC trigger chambers** gives a detailed description of the ATLAS RPC design, the RPC detector location in the Muon Spectrometer, the muon selection algorithm and the readout electronics.

- Chapter 4: **ATLAS RPC Offline Monitoring** describes in detail the structure of the offline monitoring code. The monitor of RPC system as well the algorithm used to correlate the trigger chamber response to the precision chambers are presented, together with the process to merge results from different runs.

- Chapter 5: **RPC Data Quality Monitoring Framework (DQMF)** presents the system developed to provide the Quality Assurance of the detector during the data taking. The RPC DQMF is built inside the more general ATLAS DQMF, which allows to apply automatically pre-defined algorithm to check reference histograms. In this chapter the strategy, the reference histograms and the algorithms developed for the RPC Data Quality are presented.

- Chapter 6: **RPC performance and results with offline monitoring** presents a series of results obtained by using the described offline monitoring and focused on the detector performances. In particular, a complete characterization of the detector analyzing cosmic rays data acquired in 2009 is given. Finally, the status of the detector at the time of the first ATLAS collisions

1

The standard model of elementary particles

1.1 The Standard Model

1.1.1 Particles and fundamental interactions

The Standard Model (SM) [1] of elementary particle is a re-normalizable theory based on the non-Abelian Gauge symmetry group:

$$SU(3)_{colour} \otimes SU(2)_{weak} \otimes SU(1)_{hypercharge}. \tag{1.1}$$

The subgroup $SU(3)_{colour}$ describes the colour, which is the charge of the strong interactions, whereas the subgroups $SU(2)_{weak}$ and $SU(1)_{hypercharge}$ are associated with the weak isospin and hypercharge respectively.
Elementary particles are divided into two types. The first type of particles are the fundamental constituent of the matter: these particles are *fermions*. The fermions have half-integer spin and are divided into two groups, called *leptons* and *quarks*, each group is divided in three families. Both groups are subject to electro-weak force, instead only the quarks feel the effects of the strong interaction.

Leptons and quarks are grouped in weak isospin multiplets (Tab. 1.1.1). The left-handed spinor components (marked with subscript *L*) realize one weak isospin doublet and the right-handed ones (marked with subscript *R*) realize two weak isospin singlets. This means that only left-handed particles feel the interaction associated to the weak isospin and this causes the symmetry parity breaking in the weak interactions. In the Standard Model, there are no theoretical limits on the number of the possible fermions families, but the existence of a fourth family of leptons and quarks with mass smaller than 100 GeV/c^2 (for charged leptons) and 250 GeV/c^2 (for quarks) is excluded experimentally [2].
Quarks have a further quantum number, called *colour*, that can take three values (red, green and blue). The colour charge has never been observed in nature, quarks exist only relegated in colour singlet composed particles called *hadrons*. The

Leptons	$\begin{pmatrix} e^- \\ \nu_e \end{pmatrix}_L$	$\begin{pmatrix} \mu^- \\ \nu_\mu \end{pmatrix}_L$	$\begin{pmatrix} \tau^- \\ \nu_\tau \end{pmatrix}_L$
	e_R^-	μ_R^-	τ_R^-
Quarks	$\begin{pmatrix} u \\ d \end{pmatrix}_L$	$\begin{pmatrix} c \\ s \end{pmatrix}_L$	$\begin{pmatrix} t \\ b \end{pmatrix}_L$
	u_R	c_R	t_R
	d_R	s_R	b_R

Table 1.1: Leptons and quarks divided in three families and weak isospin doublets and singlets.

hadrons are divided in baryons (fermions composed by three quarks) and mesons (bosons composed by a quark and an anti-quark).

The second type of elementary particles are represented by boson vectors: the carriers of the fundamental forces. All the fundamental interactions can be explained by the exchange of a boson vector between the interacting particles. The carrier of the electromagnetic force is the photon γ, the carriers of the weak interaction are the vector bosons $W^{\pm}$ e Z^0. Finally, the carriers of strong interaction are the gluons g_α, with $\alpha = 1, \ldots, 8$, and the carriers of gravitational interaction are the gravitons, hypothetical spin02 particles.

Experimentally the weak force is a short range interaction. This can be explained only if vector bosons have mass. In the Standard Model, the mass of the boson vectors is generated by introducing two complex scalar fields in the weak isospin doublet representations. By imposing a not zero expectation value in the vacuum state, automatically the electroweak symmetry is broken and boson vectors acquire an effective mass by interacting with the boson condensate (this is the so-called *Higgs mechanism*). Furthermore, the scalar field allows also the generation of fermions mass introducing the Yukawa potential.

In the Standard Model, a force is introduced by imposing to the Lagrangian describing the matter fields the invariance under a local (i.e. depending of the coordinates) transformation of internal symmetries group (gauge symmetry of internal group).

A gauge transformation is a transformation where the element of symmetry group depends on the point. The specific nature of the transformation is established by experiment. For example, the theory of Quantum Electrodynamics (QED) can be deduced if one imposes to field equation, that describes an electron, an invariance under a local phase transformation. The phase transformation belongs to the group $U(1)$, under which the wave function ψ transforms as $e^{i\theta(x)}\psi$. To preserve the phase local invariance, an interaction term with massless vector

boson (the photon) must be introduced.

For the weak interaction, we can proceed in the same way, but with a more complex transformation: in this case it is required that the Lagrangian is invariant under a transformation belonging to the $SU(2) \otimes U(1)$ group of the weak isospin and weak hypercharge.

The strong interaction is, instead, generated by requiring local invariance with respect to the group $SU(3)$ of the colour charge.

1.2 The Electro-weak theory

In 1961, S. L. Glashow [3] proved that the weak and electromagnetic interactions are not separated, but are two aspects of the same force: the electro-weak interaction. The theory of the electro-weak interactions is a Gauge theory based on a symmetry group $SU(2)_L \otimes SU(1)_Y$. The weak hypercharge Y, the third component of the weak isospin I and the electric charge Q are related by the Gell Mann - Nishima relation:

$$Q = I_3 + \frac{Y}{2}. \tag{1.2}$$

By requiring that the Lagrangian of the electro-weak interaction is invariant under the Gauge transformation $SU_L(2) \otimes SU_Y(1)$ and substituting the expression of the standard derivative with the covariant derivative:

$$D_\mu = \partial_\mu + ig_1 Y B_\mu + ig_2 \frac{\tau_i}{2} W_\mu^i, \tag{1.3}$$

(where $\vec{\tau}$ are the Pauli matrices and g_1, g_2 are the coupling constant of the interaction), four vector bosons are introduced: W_μ^i with $i = 1, 2, 3$ and B_μ. The Standard Model Lagrangian can be written as sum of four independent terms:

$$\mathcal{L} = \mathcal{L}_\mathcal{F} + \mathcal{L}_\mathcal{G} + \mathcal{L}_\mathcal{H} + \mathcal{L}_\mathcal{Y}, \tag{1.4}$$

where $\mathcal{L}_\mathcal{F}$ and $\mathcal{L}_\mathcal{G}$ describe respectively the kinetic term and the gauge interaction of fermions and bosons, whereas $\mathcal{L}_\mathcal{H}$ and $\mathcal{L}_\mathcal{Y}$ describe the mass generation of bosons and fermions by the introduction of Higgs scalar boson, in addition to the kinetic term and interaction of the Higgs particles.
The term $L_F = i\bar{\psi} D_\mu \psi$ is related to massless fermionic particles fields and to the interactions with gauge fields; the term

$$L_G = -\frac{1}{4} W_{\mu\nu}^i W_{\mu\nu}^i - \frac{1}{4} B_{\mu\nu} B_{\mu\nu}, \tag{1.5}$$

with

$$W_{\mu\nu}^i = \partial_\nu W_\mu^i - \partial_\mu W_\nu^i - g_2 \epsilon^{ijk} W_\mu^i W_\nu^k \tag{1.6}$$

and

$$B_{\mu\nu} = \partial_\nu B_\mu - \partial_\mu B_\nu \tag{1.7}$$

contains the kinetic term of gauge fields $\vec{W}$ and B and the self-interaction of fields $\vec{W}$ due to the fact that the group $SU(2)_{weak}$ is non abelian.
As explained in the following section, the mass eigenstates of the field $\vec{W}$ are:

$$W_\mu^\pm = \frac{1}{2}(W_\mu^1 \mp W_\mu^2), \tag{1.8}$$

whereas a combination of neutral bosons describes the photon A_μ and the Z_μ boson:

$$A_\mu = B_\mu \cos\theta_W + W_\mu^3 \sin\theta_W \tag{1.9a}$$

$$Z_\mu = -B_\mu \sin\theta_W + W_\mu^3 \cos\theta_W. \tag{1.9b}$$

The θ_W parameter is the weak mixing angle and experimentally we have that:

$$\sin\theta_W \approx 0.231,$$

furthermore, the coupling constants g_1 and g_2 are related with θ_W by the formula:

$$g_1 \sin\theta_W = g_2 \cos\theta_W = e. \tag{1.10}$$

Neglecting the self-interactions terms, the gauge term can be written as

$$L_G = -\frac{1}{4}F_{\mu\nu}F^{\mu\nu} - \frac{1}{2}F_{W\mu\nu}F_W^{\mu\nu} - \frac{1}{4}Z_{\mu\nu}Z^{\mu\nu}, \tag{1.11}$$

where $F_{\mu\nu}$ is the electromagnetic field tensor, $F_{W\mu\nu}$ is the weak charged field tensor and $Z_{\mu\nu}$ is the weak neutral field tensor given by expression similar to (1.6) and (1.7).

The Lagrangian described so far does not contain mass terms and, consequently, bosons and fermions are massless. This is because the presence of direct mass terms would destroy the invariance of the theory under the transformation $SU_L(2) \otimes SU_Y(1)$. To generate the bosons and fermions mass "inside" the theory and to be, therefore, consistent with experimental evidence, it is necessary to introduce a new scalar field and apply the *Higgs mechanism* [4], to generate boson masses, and the *Yukawa potential*, to generate fermion masses.

1.2.1 The spontaneous symmetry breaking mechanism

To generate the particles mass without destroying the invariance under the gauge transformation, it is possible to use a *spontaneous* (i.e. "implicit"[1]) breaking of the symmetry

[1] in this case, *spontaneous symmetry breaking* means that the Lagrangian is symmetric under a certain transformation, but the solutions of equation of motion are not.

This is done by introducing a complex scalar field that self-interact with a phenomenological potential:

$$V(\phi) = \mu^2 \phi^\dagger \phi + \lambda (\phi^\dagger \phi)^2, \tag{1.12}$$

where:

$$\phi = \phi_1 + i\phi_2 \tag{1.13}$$

and the parameters are chosen in such a way that the origin is a local maximum:

$$\mu^2 < 0, \quad \lambda > 0. \tag{1.14}$$

For simplicity, we consider first the breaking of the Abelian gauge group $SU(1)$. In order to have the Lagrangian invariant for a phase transformation like:

$$\phi \rightarrow e^{i\alpha(x)}\phi, \tag{1.15}$$

it is necessary to replace the standard derivative with covariant derivative:

$$D_\mu = \partial_\mu - ieA_\mu, \tag{1.16}$$

introducing the gauge field A_μ that transforms according to:

$$A_\mu \rightarrow A_\mu + \frac{1}{e}\,\partial_\mu \alpha. \tag{1.17}$$

Then, the gauge-invariant Lagrangian is given by:

$$\mathcal{L} = (\partial^\mu - ieA^\mu)\phi^*(\partial_\mu - ieA_\mu)\phi - \mu^2\phi^*\phi - \lambda^2(\phi^*\phi)^2 - \frac{1}{4}F_{\mu\nu}F^{\mu\nu}. \tag{1.18}$$

The potential $V(\phi)$ has a minimum in the points of space (ϕ_1, ϕ_2) belonging to a circle with radius v given by:

$$v^2 = \phi_1^2 + \phi_2^2 \qquad \text{with} \qquad v^2 = -\frac{\mu^2}{\lambda}. \tag{1.19}$$

Around a minimum energy point $(\phi_1 = v,\, \phi_2 = 0)$, we can write ϕ in terms of two real fields (η, ξ) defined by:

$$\phi(x) = \frac{1}{\sqrt{2}}\left[v + \eta(x) + i\xi(x)\right]. \tag{1.20}$$

By substituting (1.20) into (1.18), the last equation becomes:

$$\mathcal{L} = \frac{1}{2}(\partial_\mu \xi)^2 + \frac{1}{2}(\partial_\mu \eta)^2 - v^2\lambda\eta^2 + \frac{1}{2}e^2v^2A_\mu A_\mu \\ - evA_\mu\partial^\mu\xi - \frac{1}{4}F_\mu\nu F^\mu\nu + \text{ interaction terms.} \tag{1.21}$$

The equation (1.21) describes the dynamics of a massless boson ξ, a massive scalar boson η and a massive vector boson A_μ. The Lagrangian (1.21) has one degree of freedom more than the Lagrangian (1.18). Because a change of coordinates cannot change the number of degrees of freedom, we deduce that equation (1.21) contains an unphysical field not representing a real particle. It is possible to choice a specific gauge transformation by which the unphysical field disappears from the Lagrangian. Indeed, by writing:

$$\phi = \frac{1}{\sqrt{2}}\left(v + \eta + i\xi\right) = \frac{1}{\sqrt{2}}\left(v + h(x)\right) e^{i\theta(x)/v} \tag{1.22}$$

It is possible to choose a new set of real fields (h,θ) and a new boson field A_μ:

$$A_\mu \longrightarrow A_\mu + \frac{1}{ev}\partial_\mu\theta. \tag{1.23}$$

In this particular case, $\theta(x)$ is chosen such that h is real. Therefore we have the Lagrangian:

$$\mathcal{L}'' = \frac{1}{2}(\partial_\mu h)^2 - \lambda v^2 h^2 + \frac{1}{2}e^2 v^2 A_\mu^2 - \lambda v h^3 - \frac{1}{4}\lambda h^4 + \frac{1}{2}e^2 A_\mu^2 h^2 + v e^2 A_\mu^2 h - \frac{1}{4}F_{\mu\nu}F^{\mu\nu}, \tag{1.24}$$

in which we get two massive particles, the vectorial boson A_μ and the scalar h (the *Higgs boson*) and no off-diagonal terms, like the term $evA_\mu\partial^\mu\xi$ of (1.21).
For the case of the breaking of $SU(2)$ group symmetry, we start by considering a Lagrangian defined as:

$$\mathcal{L} = (\partial_\mu\phi)^\dagger(\partial^\mu\phi) - \mu^2\phi^\dagger\phi - \lambda^2\left(\phi^\dagger\phi\right)^2, \tag{1.25}$$

where ϕ is a complex scalar $SU(2)$ doublet.

$$\phi = \begin{pmatrix}\phi_\alpha \\ \phi_\beta\end{pmatrix} = \frac{1}{\sqrt{2}}\begin{pmatrix}\phi_1 + i\phi_2 \\ \phi_3 + i\phi_4\end{pmatrix}. \tag{1.26}$$

In order to make $\mathcal{L}$ invariant under the *local* gauge transformation defined by:

$$\phi \longrightarrow \phi' = e^{\,i\,\alpha_a(x)\tau_a/2}\phi, \tag{1.27}$$

it is necessary to use in equation (1.25) instead of the standard derivative the covariant derivative:

$$D_\mu = \partial_\mu + ig\,\frac{\tau_a}{2}\,W_\mu^a. \tag{1.28}$$

In this case, three gauge fields $W_\mu^a(x)$ (with $a = 1, 2, 3$) are introduced. Under the infinitesimal transformation:

$$\phi(x) \longrightarrow \phi'(x) = (1 + i\alpha(x) \cdot \tau/2)\phi(x) \tag{1.29}$$

these fields transform as:

$$W_\mu \longrightarrow W_\mu - \frac{1}{g}\partial_\mu \alpha - \alpha \times W_\mu. \tag{1.30}$$

Therefore the gauge invariant Lagrangian corresponding to equation (1.28) is:

$$\mathcal{L} = \left(\partial_\mu + ig\frac{1}{2}\tau \cdot W_\mu \phi\right)^\dagger \left(\partial^\mu + ig\frac{1}{2}\tau \cdot W^\mu \phi\right) - V(\phi) - \frac{1}{4}W_{\mu\nu} \cdot W_{\mu\nu}, \tag{1.31}$$

with

$$V(\phi) = \mu^2 \phi^\dagger \phi + \lambda(\phi^\dagger \phi)^2 \tag{1.32}$$

and

$$W_{\mu\nu} = \partial_\mu W_\nu - \partial_\nu W_\mu - gW_\mu \times W_\nu. \tag{1.33}$$

If $\mu^2 > 0$, the equation (1.31) describes a physical system of four scalar particles ϕ_i interacting with three massless gauge bosons W_μ^a. If $\mu^2 < 0$ and $\lambda > 0$, the potential $V(\phi)$ of (1.32) has a minimum at the points satisfying the conditions:

$$\phi^\dagger \phi = \frac{1}{2}(\phi_1^2 + \phi_2^2 + \phi_3^2 + \phi_4^2) = -\frac{\mu^2}{2\lambda}. \tag{1.34}$$

We can expand $\phi(x)$ in a neighbourhood of a chosen minimum:

$$\phi_1 = \phi_2 = \phi_4 = 0 \qquad \phi_3^2 = -\frac{\mu^2}{\lambda} \equiv v^2. \tag{1.35}$$

Therefore, by expanding $\phi(x)$ in the neighbourhood of the selected vacuum state:

$$\phi_0 = \sqrt{\frac{1}{2}}\begin{pmatrix} 0 \\ v \end{pmatrix} \tag{1.36}$$

and substituting the field

$$\phi(x) = \sqrt{\frac{1}{2}}\begin{pmatrix} 0 \\ v + h(x) \end{pmatrix}, \tag{1.37}$$

into the Lagrangian (1.31), we obtain that the only scalar field surviving is the Higgs field $h(x)$. Indeed, if we write $\phi(x)$ as

$$\phi(x) = e^{i\tau \cdot \theta(x)/v}\begin{pmatrix} 0 \\ \frac{v+h(x)}{\sqrt{2}} \end{pmatrix}, \tag{1.38}$$

with $\theta_1, \theta_2, \theta_3$ and h real fields the exponential term drop out from the Lagrangian. By substituting ϕ_0 (defined in (1.36)) into the Lagrangian, we obtains:

$$\begin{aligned} \left| ig\frac{1}{2}\tau \cdot W_\mu \phi \right|^2 &= \frac{g^2}{8} \left| \begin{pmatrix} W_\mu^3 & W_\mu^1 - iW_\mu^2 \\ W_\mu^1 + iW_\mu^2 & W_\mu^3 \end{pmatrix} \begin{pmatrix} 0 \\ v \end{pmatrix} \right|^2 \\ &= \frac{g^2 v^2}{8} \left[(W_\mu^1)^2 + (W_\mu^1)^2 + (W_\mu^1)^2 \right] \end{aligned} \tag{1.39}$$

and the mass of vector boson is given by $M = \frac{1}{2}gv$. Therefore, the Lagrangian describes three massive gauge fields and one massive scalar h.

1.3 Higgs boson mass constraints

The standard model does not predict the Higgs boson mass, however, it is possible to estimate lower and upper theoretical limits by imposing the internal consistency of the theory. In addition, in recent years, a huge amount of data are collected with experiments at LEP accelerator (electron-positron collider operated from 1989 to 2000 in CERN laboratories at Geneva, see ref ...) and at Tevatron accelerator (proton - antiproton collider build and still in activity at FNAL near Chicago, see ref ...) . From these data, it is possible to obtain experimental boundaries to Higgs boson mass.

1.3.1 Theoretical limits

In addition to understand the origin of particles mass, the existence of Higgs boson is fundamental even to guarantee the renormalizability of electro-weak theory. By requiring that the theory wold be renormalizable only at low energy ($\Lambda \sim 1$ TeV), the possible Higgs boson mass interval ranges about 7 GeV to about 10^3 GeV. The allowed mass interval becomes narrower if we require that the standard model would be consistent up to energy Λ. For a quark top mass m_t equal to 175 GeV, the allowed values of Higgs boson mass, as function of the energy Λ, are showed in figure 1.1.

1.3.2 Experimental limits

The precision reached on the measures of electro-weak observables by the experiments with e^+- e^- collisions amounts to about fractions of percent. These measurements indirectly impose limits to Higgs boson mass. The results of direct Higgs search at LEP experiments fix the lower mass limits to $m_H > 114.1 GeV/c^2$ with

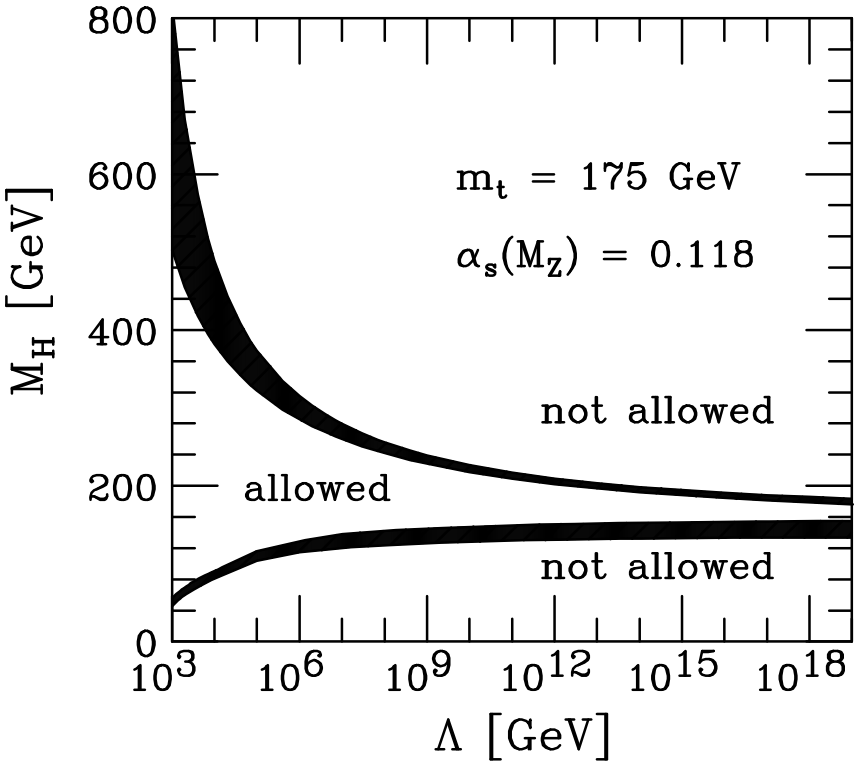

Figure 1.1: Higgs boson mass range vs energy scale to which the standard model is theoretically consistent.

95 % confidence level. After the precise measurements of top quark mass (equal to 171.2 ± 2.1 GeV [5]) made at Tevatron experiments, the observables of the standard model can be written as function of the Higgs boson mass only. The fit performed to the measured observables, leaving the Higgs mass m_H as free parameter has a χ^2 with a minimum at $m_H = 85$ GeV and an upper limit at $m_H < 212$ GeV with 95 % confidence level (this result is showed in Figure 1.2).

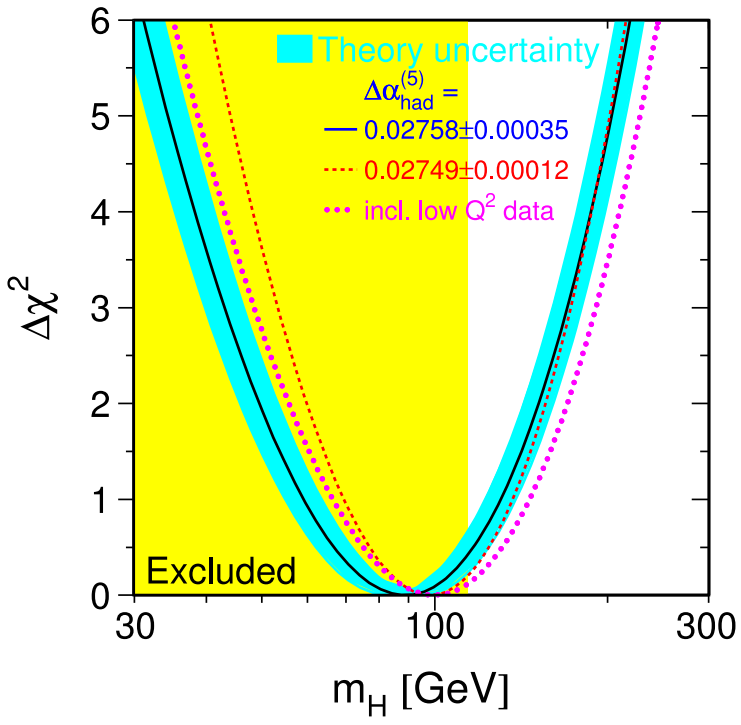

Figure 1.2: Change of $\Delta\chi^2$ of SM observables as a function of Higgs boson mass. The yellow band is the mass region excluded at LEP by direct searches.

Finally, data collected from experiments D_0 and CDF at Tevatron (proton - antiproton collision with a center of mass energy equal to 1.96 TeV) allow to exclude, with 95% confidence level, the mass range between 163 and 166 GeV/c^2 [6] [7]. A summary of allowed and excluded mass ranges is showed in figure 1.3: the variable used to discriminate over allowed and forbidden regions for Higgs mass is the ratio between the number of signals recorded (as function of mass m_H) and the number of signal expected in the background only hypothesis [8].

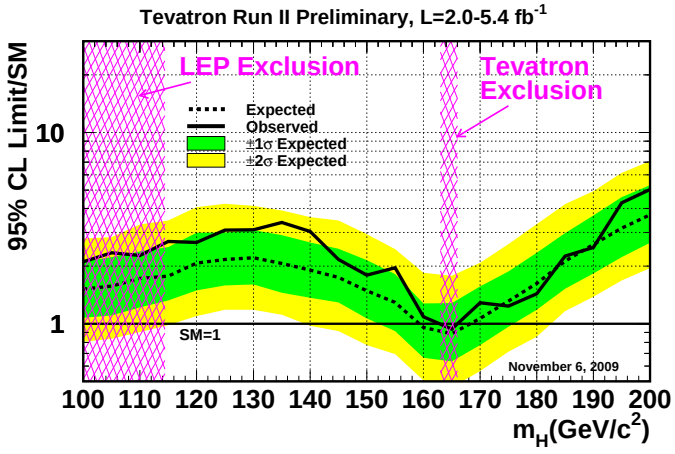

Figure 1.3: Ratio of experimental limits on Higgs boson production cross section to SM cross section as function of Higgs boson mass. The ratio is expressed in units of SM predictions. A value of the normalized ratio equal or less than one means that the corresponding Higgs boson mass is forbidden (with the 95% C.L.).

1.4 Supersymmetry

1.4.1 Open questions in standard model

The standard model has an excellent agreement (within a precision of about 0.1%) with results obtained from all experiments made up to now. However it contains several open and unsolved questions. Up to now, the Higgs boson, theoretically foreseen, has never been observed in accelerators experiments. Furthermore, it is very likely that the standard model is only an approximation (exact only at low energy) of a more general theory. In the standard model, weak and electromagnetic interactions are described in a unified theory, but strong force are not yet unified with electroweak force. It is thought that exist a higher energy scale at which all three fundamental forces are unified (*Great Unification Theory* or GUT).

In addition, particles quantum number are not quantitatively foreseen from theory, therefore the model contains 19 “free” parameters, whose values have to be inserted “by hand” in the model (the neutrino oscillations add three additional free parameters).

A further problem is the so-called “hierarchical problem”. The Higgs boson is the only scalar field foreseen inside the standard model. The particularity of a scalar field is that mass corrections have a square divergence with the cut-off

energy Λ^2, instead all other divergences are proportional to $log\Lambda^2$. This leads to the divergence of the Higgs mass. This problem can be resolved if the Higgs boson is embedded in a supersymmetric theory.

1.4.2 Supersymmetry

The supersymmetric theory (so-called *SUSY*) is one of the most promising extension of the standard model and will be, therefore, one of the most important research area for ATLAS and the other LHC experiments. Supersymmetry is the largest extension of the Lorentz group and starts from the existence of a symmetry between fermions and bosons. For each particle with integer spin, there must exist a particle with the same internal quantum numbers, but with half-integer spin (and, vice versa, for each particle with half integer spin there is a particle that has integer spin). According to the used nomenclature, supersymmetric particles associated to the know particles are designed with a tilde over the symbol (for example "ẽ"); supersymmetric boson have the same name of standard bosons, but with the prefix *s-*; instead supersymmetric fermions are designed with names of standard fermions followed by the suffix *-ino*.
The supersymmetric generator $\{Q, \bar{Q}\}$ satisfies the following commutation rules:

$$\{Q, \bar{Q}\} = -2\gamma_\mu P^\mu \tag{1.40}$$

$$[Q, P^\mu] = \{Q, Q\} = \{\bar{Q}, \bar{Q}\} = 0 \tag{1.41}$$

$$Q|bosons\rangle = |fermions\rangle \qquad Q|fermions\rangle = |bosons\rangle \tag{1.42}$$

(P^μ is the momentum operator and γ_μ are the Dirac matrix).
In the minimal extension of standard model (MSSM), each chiral fermion $f_{L,R}$ is associated to one scalar sfermion $\tilde{f}_{L,R}$ and each massless gauge boson A_μ with two elicity states ± 1 is associated to one massless gaugino with spin $-1/2$ and elicity ± 1. There are also two complex Higgs doublets and their own associated Higgsino. Interactions between supersymmetric particles are obtained from corresponding standard interactions by substituting line of each vertex with supersymmetric particles. Supersymmetry solves the hierarchical problem, due to the fact that bosons and fermions leads to the cancellation of square loop divergences. If the scale of the supersymmetric particles is about 1 TeV, Supersymmetry solves also the problem of the unification of fundamental (electro-weak and strong) interaction and provide a natural candidate for the dark matter.

Supersymmetry is obviously broken, because superparticles have never been observed and many mechanism to broke the symmetry, such as *mSugra*, are foreseen by the theory.

1.5 Higgs search at LHC

1.5.1 Standard Model Higgs

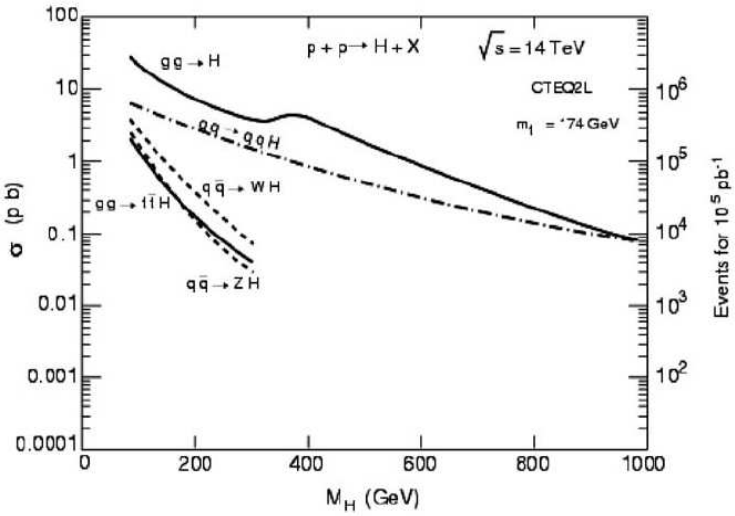

Figure 1.4: Production cross-sections for the SM Higgs boson as a function of its mass at LHC, for the expected production processes.

The standard model predicts various possible electroweak mechanisms for the production of the Higgs boson. In figure 1.4, the expected production cross sections, at LHC design energy for these process are reported as function of Higgs boson mass. As could be seen from the figure, the dominant process are the *gluon - gluon fusion* ($gg \rightarrow H$) and the *vector boson fusion* ($qq \rightarrow qqH$) whose Feynman diagrams are drawn in figure 1.5. The cross section are numerically small, therefore the Higgs search will be difficult because of the low rate production and the small signal/background ratio. The searches will be focused on different final states according to the possible values of the Higgs mass (figure 1.6): in the low mass region, the most important is the decay channel $H \rightarrow \gamma\gamma$; in the intermediate and high mass regions, the channel $H \rightarrow 4\ell$ and, at very high mass, the decay in $H \rightarrow 2\ell\nu\overline{\nu}$. In the next sections, it will be reported the details of the decay channels, classified depending the expected Higgs mass [9]. The branching ratios of the Standard Model Higgs boson decay channels as a function of Higgs mass are reported in figure 1.6

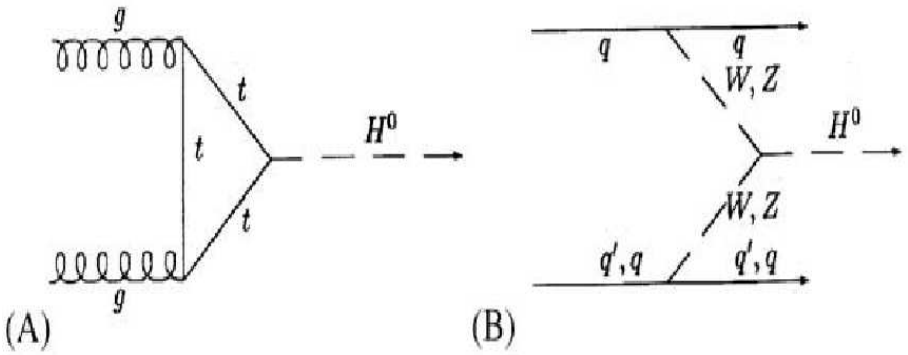

Figure 1.5: Feynman diagrams of the processes mainly contributing to the production of a SM Higgs boson at LHC: (a) g-g fusion, (b) WW and ZZ fusion.

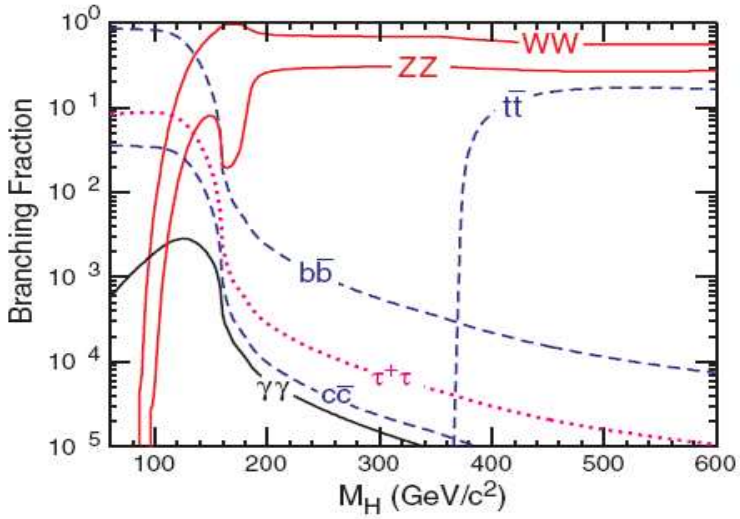

Figure 1.6: Branching ratios of the Standard Model Higgs boson decay channels as a function of its mass.

Low-mass Higgs

In the low mass region, the Higgs mainly decays into $b\bar{b}$, but the signal can neither be triggered or extracted out of the huge $b\bar{b}$ background due to standard QCD process. For this reason, the most promising channel is the decay into $\gamma\gamma$, which has a tiny branching ratio but a very narrow mass peak above the smooth QCD background (see figure 1.7). Excellent energy and angular resolution are needed to observe the narrow mass peak above the irreducible prompt $\gamma\gamma$ continuum. Powerful particle identification capability is also required to reject the large QCD jet background.

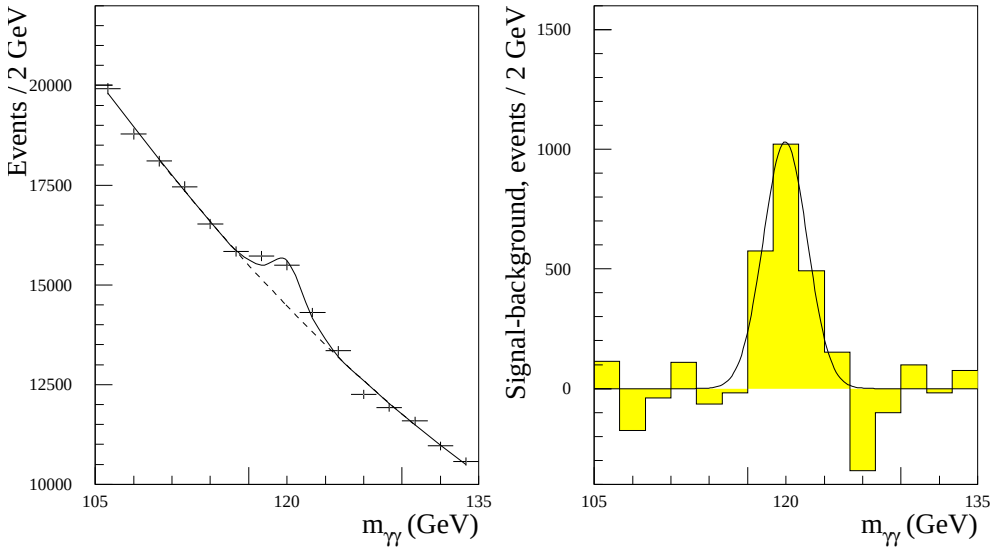

Figure 1.7: Simulated invariant mass distribution of the $\gamma\gamma$ candidates in ATLAS detector from a Higgs boson with mass of 120 GeV, superimposed to the background, at 100 fb^{-1}. In the right figure the signal is shown after background subtraction.

Intermediate-mass Higgs

In the range energy from 130 GeV to $2M_Z$, the decay $H \rightarrow ZZ^* \rightarrow 4l$ is favourite. The event rate is small and the background reduction is difficult because one of the Z is off-shell. In this mass region the Higgs natural width is small ($\leq$ 1GeV), then lepton energy and momentum resolutions are important. The irreducible background arises from the continuum $ZZ^{(*)}$ production. The $t\bar{t}$ reducible background can be suppressed by lepton isolation and by lepton pair invariant mass cuts, while the reducible background $Zb\bar{b}$ can be suppressed by

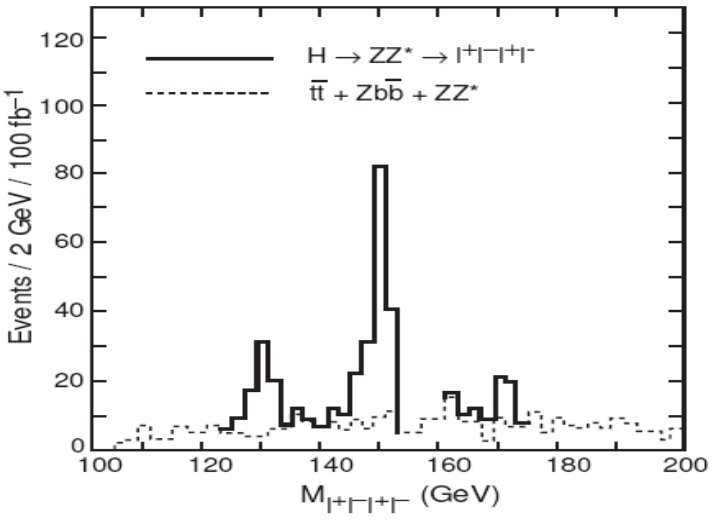

Figure 1.8: Simulated 4-leptons invariant mass distribution for various Higgs masses (130, 150 and 170 GeV) with the sum of all backgrounds for 100 fb^{-1} in ATLAS.

isolation requirements. The signals obtained are very significant (figure 1.8): ATLAS expects signals at the level of 10.3 (7.0), 22.6 (15.5) and 6.5 (4.3) standard deviation respectively for M_H = 130, 150, and 170 GeV in 100 fb^{-1} (30 fb^{-1}).

The decay $H \rightarrow WW^{(*)} \rightarrow l^+\nu l^-\overline{\nu}$ can provide valuable information in the mass region around 170 GeV. The dominant background arises from the production of W pairs surviving the cuts used to remove the $t\overline{t}$ background.

High-mass Higgs

The "golden" decay mode $H \rightarrow ZZ \rightarrow 4l$ has a signal excess of six standard deviation over a wide range of Higgs masses from $2M_Z$ to about 600 GeV at 100 fb^{-1}.

Electron and muon resolutions and selection cuts are similar as for the ZZ^* channel. As the Higgs mass increases, its width increases and its production rate falls. Decay channels with larger branching fraction are $H \rightarrow WW/ZZ \rightarrow ll/\nu\overline{\nu} + jets$. The enormous $W + jets$ and $Z + jets$ background must be reduced tagging on one or two forward jets associated to the boson fusion production.

1.5.2 Supersymmetric Higgs

The Higgs sector of the Minimal Supersymmetric Standard Model (MSSM) foresees two charged physical states ($H^{\pm}$) and three neutral states (h, H, A). This lead

to a large spectrum of possible signals and makes difficult the search of an evidence of a supersymmetric Higgs boson [9].
All the mass and the coupling constants of Higgs boson can be parametrized in term of the mass of the CP-odd boson m_A and the ratio between the vacuum expectation value of Higgs doublets, written as $tan\beta$. Theoretical and experimental studies ([10], [11]) on the detection of the MSSM Higgs boson at the LHC have selected sets of parameters, for which supersymmetric particle masses are large. This forbids kinetically the Higgs boson decay in SUSY particles. Therefore, will be investigated decay mode accessible also in case of SM Higgs boson: $H \rightarrow \gamma\gamma$, $H \rightarrow b\bar{b}$, $H \rightarrow ZZ \rightarrow 4l$ (other possible channels are $H/A \rightarrow t\bar{t}$, $A \rightarrow Zh$, $H \rightarrow hh$). At large $tan\beta$ the most probable modes are $H/A \rightarrow \tau\tau$ and $H/A \rightarrow \mu\mu$.
Instead, if susy particles are enough light, decay mode to supersymmetric particles are allowed [12]. In conclusion, the all range 50-500 GeV and $\tan\beta = 1-50$ should be reachable for the Higgs boson discovery at ATLAS experiment.

2

The ATLAS experiment at Large Hadron Collider

2.1 The Large Hadron Collider

The Large Hadron Collider (LHC) is the new superconducting proton-proton accelerator [13] installed at about 100 m deep below the countryside of Geneva (Switzerland) at the CERN laboratory (*"European Organization for Nuclear Research"*). It is now in its initial operating phase at half designed energy and it is made by two coaxial rings housed in the 27 km tunnel previously constructed for the Large Electron Positron Collider (LEP). The accelerator has been designed to provide proton-proton collisions with the unprecedented luminosity $\mathcal{L}$ of 10^{34} $cm^{-2}s^{-1}$, where $\mathcal{L}$ is given by the formula:

$$\mathcal{L} = f\frac{N_1 N_2}{4\pi\sigma_x\sigma_y}F \tag{2.1}$$

with: N_1 and N_2 the number of protons per bunch and per beam, *f* the bunch collision frequency, σ_x and σ_y the parameters characterize the Gaussian beam transverse profile in the horizontal and vertical directions respectively, *F* the geometric reduction factor due to the beam crossing angle. In the final operational configuration, the proton beams will collide with an energy of 7 TeV per beam, providing a center-of-mass energy of 14 TeV, which is one order of magnitude higher than the one reached in any previous collider. The main design parameters of the LHC machine are shown in table 2.1.

In addition to the p-p operation, LHC will be able to collide heavy nuclei, e.g. Pb-Pb, with a center-of-mass energy of 2.76 TeV/nucleons at an initial luminosity of 10^{27} $cm^{-2}s^{-1}$.

Two main luminosity scenarios are foreseen for the LHC in p-p operation:

- an initial "low luminosity scenario" with a peak luminosity of about 10^{33} $cm^{-2}s^{-1}$, corresponding to an integrated luminosity of about 10 fb^{-1} per year.

Circumference	26.7 km
Design peak luminosity	$10^{34} cm^{-2} s^{-1}$
Beam energy at collision	7 TeV
Beam energy at injection	0.45 TeV
Dipole field at 7 TeV	8.33 T
Coil aperture	56 mm
Peak beam current	0.56 A
Protons per bunch	1.1×10^{11}
Number of bunch	2808
Nominal bunch spacing in time	24.95 ns
Bunch spacing	7.48 m
Normalized transverse emittance	3.75 μm
R.M.S. bunch length	75 mm
Filling time per ring	4.3 min
Luminosity life time	10 h
Total crossing angle	300 μrad
Energy loss per turn	6.7 keV
Radiated power per beam	3.8 kW
Stored energy per beam	350 MJ
Stored energy in magnets	11 GJ
Operating temperature	1.9 K

Table 2.1: Main design parameters of the LHC.

- the design "high luminosity scenario" to be reached approximately 3 years after the startup, with a peak value of about 10^{34} $cm^{-2}s^{-1}$, corresponding to an integrated luminosity of 100 fb^{-1} per year.

At high luminosity, the beam will be arranged in 2808 bunches of 1.1×10^{11} protons per bunch, which will collide each 25 ns in the interaction regions (IR). Given a predicted p-p inelastic cross section of about 100 mb at 14 TeV, about 23 p-p interactions per crossing and a total of about 700 charged particles with $P_T >$ 150 MeV will be produced.

Figure 2.1 shows the injection system layout for LHC. Protons are produced and accelerated up to 50 MeV by a proton linac before being injected into the 1.4 GeV Proton Synchrotron Booster (PSB). A Proton Synchrotron (PS) will accelerate protons up to 26 GeV and, finally, the 450 GeV Super Proton Synchrotron (SPS) will inject protons into LHC, where they will be finally accelerated up to 7 TeV.

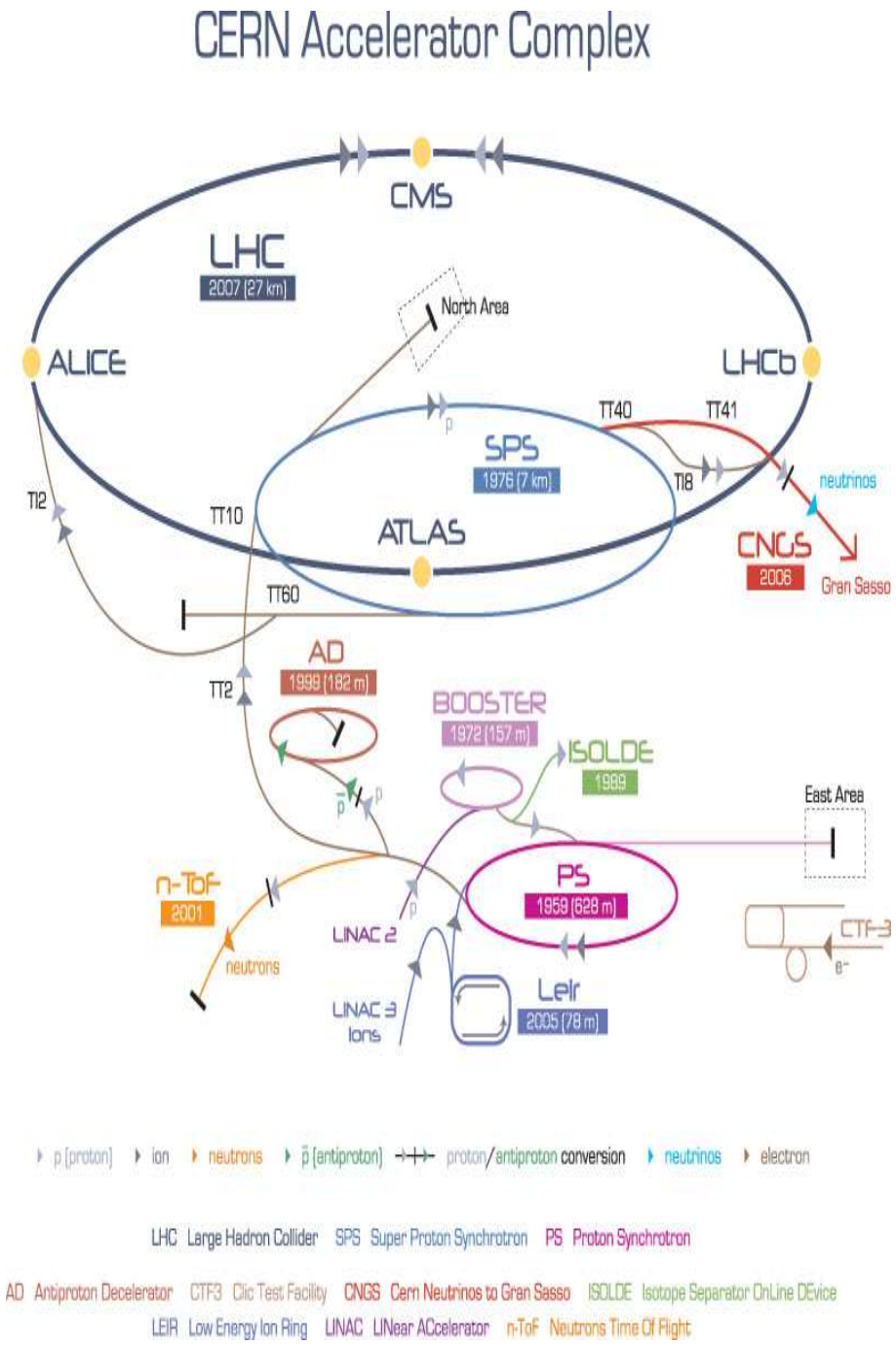

Figure 2.1: Accelerator complex at CERN.

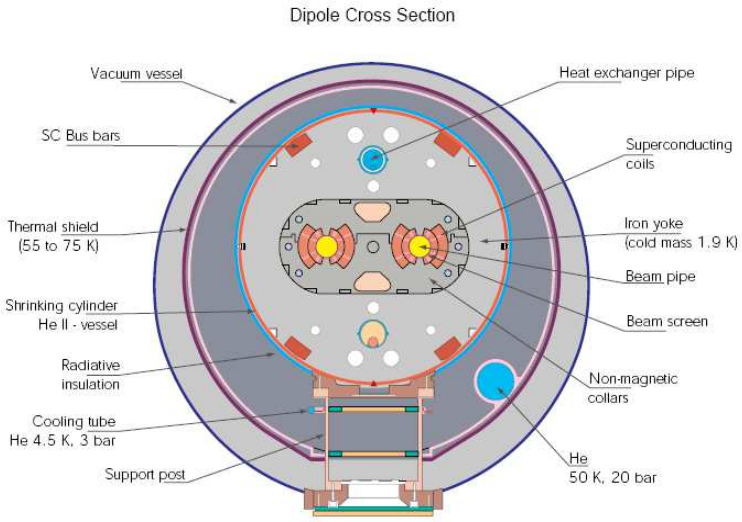

Figure 2.2: Cross section of a twin-bore magnet for LHC.

The request for very high luminosity excluded the use of a p-$\overline{\text{p}}$ (since an anti-proton beam would require several hours to cool and accumulate anti-protons before injection), consequently, a common vacuum and magnet system for both circulating beams was not possible. In fact, to collide two beams of equally charged particles requires opposite magnet dipole fields. Therefore, LHC is designed as a proton-proton collider with separate magnetic fields and vacuum chambers in the main arcs and with common pipes, about 130 m long, at the intersection regions (IR), where the experimental detectors are located. The two beams are separated along the IR in order to avoid parasitic collision points.

Since there was not enough space in the LEP tunnel to accommodate two separate rings of magnets, LHC uses twin bore magnets, which consists of two sets of coils and beam channels within the same mechanical structure and cryostat (see figure 2.2). 7 TeV peak beam energy implies a 8.33 T peak dipole field and the use of a superconducting magnet technology.

Along the accelerator ring, there are four interaction points when proton beams will collide. In the underground caverns built around those points, the detectors ATLAS, CMS, ALICE and LHCb are installed. ATLAS (in detail described in section 2.2) and CMS are general purpose experiments, developed to investigate the largest range of physics possible, whereas LHCb and ALICE are specialized detector to investigate specific phenomena.

2.2 The ATLAS experiment at LHC

The ATLAS (A Toroidal LHC ApparatuS) experiment is the result of the efforts of a world-wide huge collaboration, composed of about 2800 researchers from 173 universities and laboratories of 39 countries. The ATLAS detector layout is shown in figure 2.3 [14].

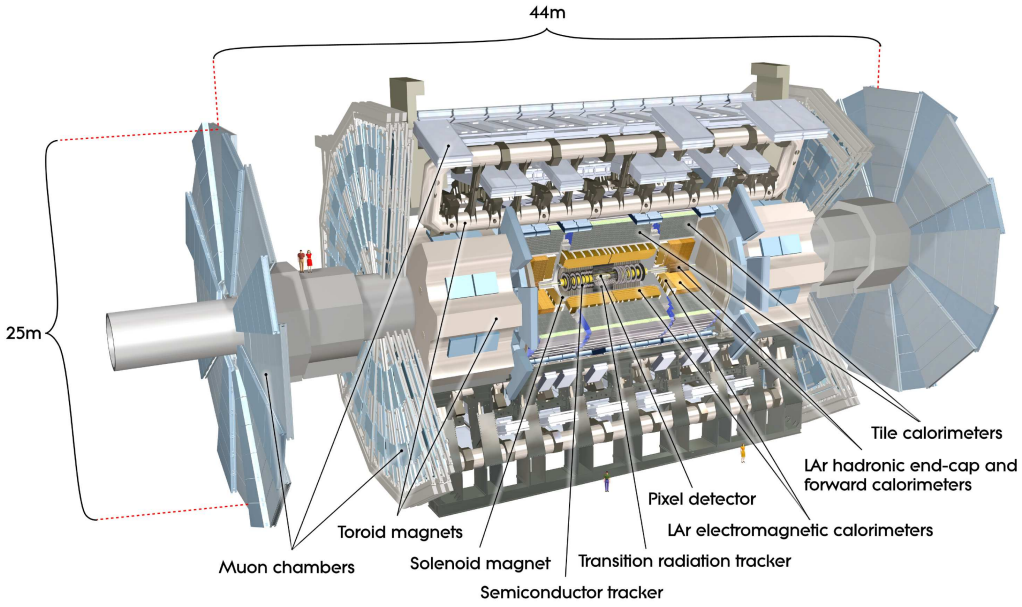

Figure 2.3: Overall view of the ATLAS detector displaying various sub-detectors.

The detector has a typical onion structure around the beam pipe. It is composed by many different sub-detectors: inner detectors, calorimeter detectors and muons detectors. Several of these detectors are surrounded by a magnetic field generated by four magnetic systems.

In the right-handed coordinate system used, the nominal interaction point (IP) is defined as the origin of the coordinate system, the z axis coincides with the beam axis, the positive x axis points to center of LHC ring from IP and the positive y axis is oriented upwards. The coordinate system mostly used are the coordinate z, ϕ (azimuthal angle measured around beam axis) and θ (polar angle). The *pseudo-rapidity* is defined as $\eta = -\ln\tan(\theta/2)$.

2.2.1 Magnet system

To measure the charged particle momentum, ATLAS uses a magnet system made of a central solenoid, an air-core barrel toroid and two air-core end-cap toroids.

The dimensions of the overall system are 26 m of length and 22 m of diameter and it stores an energy of 1.6 GJ [15].

The central solenoid is aligned with the beam axis and provide a 2 T axial magnetic field for the inner detector. Because the solenoid lies inside the calorimeter volume, it has been designed to keep the material thickness in front of the calorimeter as low as possible. In particular, the solenoid windings and the Liquid Argon calorimeter share a common vacuum vessel.

The barrel toroid is made of eight flat coils assembled radially and symmetrically. In the windings coils, built with aluminium stabilized Nb/Ti/Cu superconductor and cooled at 4.5 K, a current of 20.5 kA circulates. The barrel toroid provides a field of approximately 0.5 T (depending on η) in the region $|\eta| <$1.3.

Two end-cap toroids are lined with the central solenoid and generate the magnetic field required for optimising the bending power in the end-cap regions of the muon spectrometer system. Each toroid is made of eight flat coils (rotated by 22.5° with respect the barrel toroid coils) located in one large cryostat. The field provided by end-cap toroids is approximately 1 T in the pseudo-rapidity range 1.6 $< \eta <$ 2.7. The geometry of the magnet coils system is schematized in figure 2.4.

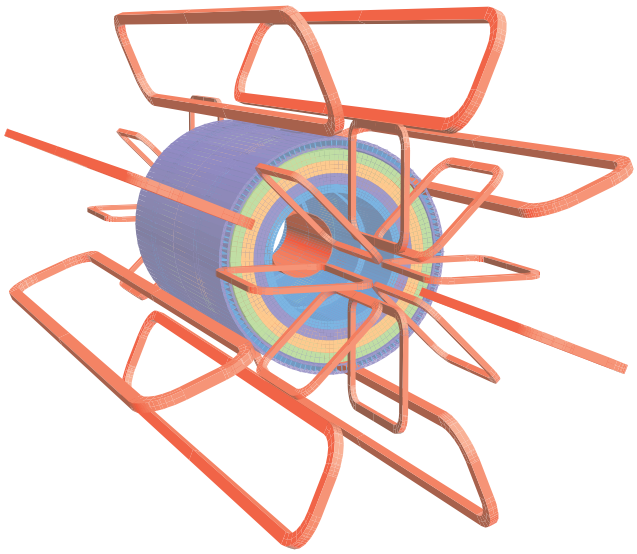

Figure 2.4: Geometry of magnet windings and tile calorimeter steel.

2.2.2 Inner detector

The ATLAS Inner Detector (ID) [16, 17] is contained in a cylinder about 7 m long and with radius of 1.15 m, within a solenoidal magnetic field of 2 T. The goal of

the ID is to provide a hermetic and robust, in the very high rate environment of the LHC accelerator, pattern recognition, an excellent momentum resolution and a measure of primary and secondary vertexes. For all those purposes, a tracker system consisting of three independent and complementary sub-detectors (from inner to outer radii silicon pixels, silicon strips and straw tube) has been developed.

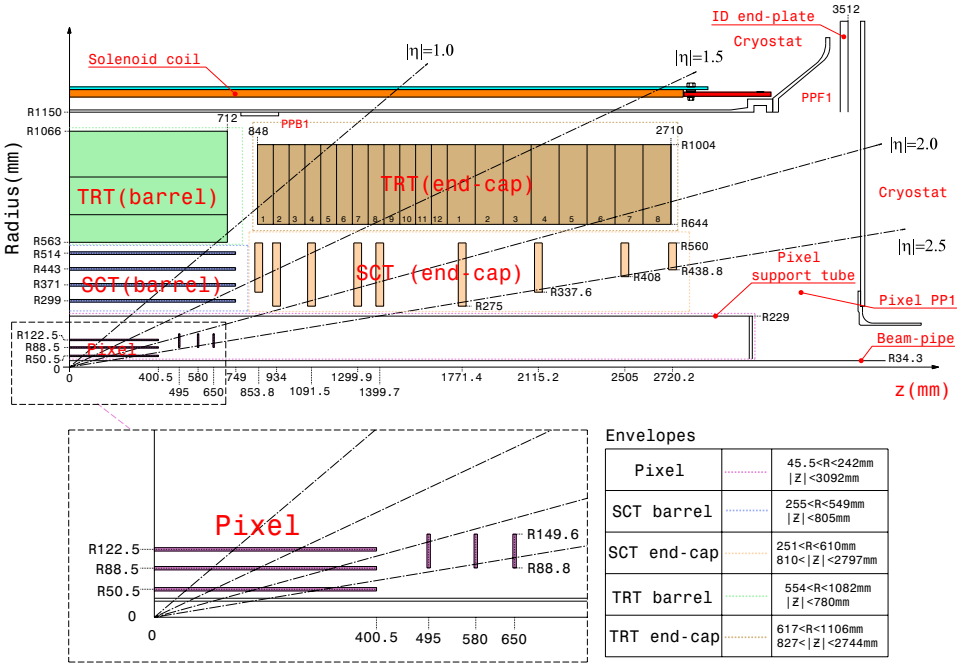

Figure 2.5: Schematic view of a quarter section of the ATLAS Inner Detector.

Silicon pixels [18] are arranged on three coaxial layers in the barrel region and on end-cap three disk (on each side), in total, 1744 pixel modules are installed. The fine granularity (10 μm in $R-\phi$ plane and 115 μm in z) allows to have three high precision points for pattern recognition near the interaction region and, therefore, to reconstruct primary and secondary particles decay vertex.

The Silicon Strips detector (SCT) is made by four layers in barrel region and nine wheels for each end-cap. There are a total of 15912 sensors with 768 strips of 12 cm length per sensor, with a pitch of 80 μm. The detector has an intrinsic resolution of 17 μm (in $R-\phi$ plane) and of 580 μm (in z) and provides at least four precision measurements for each track.

The Transition Radiation Tracker (TRT) is made of polyamide drift (straw) tubes of 4 mm diameter interleaved with transition radiation material. It enhances the pattern recognition with an average of 36 point per track and improves the momentum resolution, without introducing a large amount of materials in front of the calorimeter. By detecting the transition radiation it can discriminate and reject

electrons and pions. TRT tubes (which have an intrinsic resolution of 130 μm) are parallel to beam pipe in barrel region and arranged in 16 disks in the end-cap regions.

2.2.3 The calorimeter system

The ATLAS calorimeters are crucial for the reconstruction of the most important physics channels. In particular, high accuracy on the measurements and identifications of electrons and photons and a full coverage hadronic calorimetry, for accurate jet and missing transverse energy measurement, are fundamental. The ATLAS calorimeter system is composed of an Electromagnetic Calorimeter, a Hadronic Calorimeter and a Forward Calorimeter [19, 20]. Figure 2.6 reports a general view of ATLAS calorimeters. The electromagnetic calorimeter is separated in a barrel component (η<1.475) and in two end-cap components (1.375<η<3.2) and is constituted of a sampling lead-liquid argon detector, with accordion shaped kapton electrodes and lead absorber plates. Major physical requirements for the detector are a largest possible acceptance, a good electron reconstruction and an excellent energy resolution in a large range (10-300 GeV).

The hadronic calorimeter is composed of:

Tile calorimeter Is the outer part of the system, separated in barrel and end-cap regions. It uses steel as absorber and scintillating tiles as the active material.

LAr hadronic end-cap calorimeter Is made of two independent wheels per end-cap and uses the copper-liquid argon sampling technique with flat plate geometry and GaAs preamplifiers in argon.

LAr forward calorimeter The FCal is approximately 10 interaction lengths deep and consists of three modules in each end-cap: the first, made of copper, is used for electromagnetic measurements, while the other two, made of tungsten, measure the energy of hadronic interactions.

2.2.4 The ATLAS Muon Spectrometer

The ATLAS Muon Spectrometer [21] design, based on a system of three large superconducting air core toroids, was driven by the need of having a very high quality stand-alone muon measurement, with large acceptance both for muon triggering and measuring, in order to achieve the physics goals discussed in the first chapter.

Precision tracking in the Muon Spectrometer is guaranteed by the use of high precision drift and multi-wire proportional chambers. Great emphasis has been

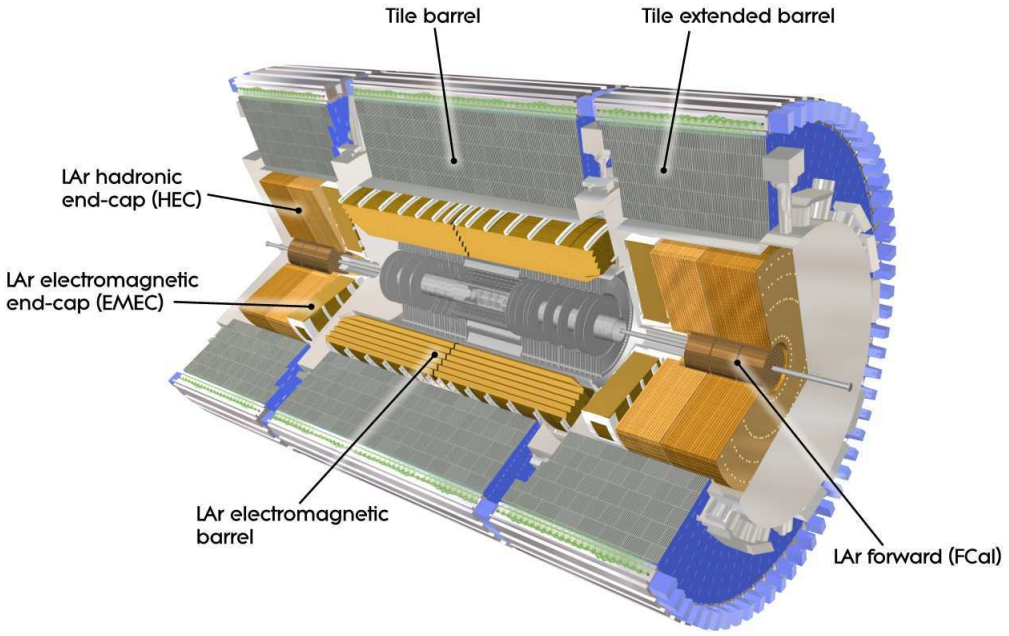

Figure 2.6: Schematic view of the ATLAS calorimeters system.

given in the design phase to system issues such as the alignment of the tracking detectors. Triggering is accomplished using dedicated fast detectors, that allow bunch crossing identification, with limited spatial accuracy. These detectors provide also the measurement of the coordinate in the non-bending plane in the barrel region, where drift chambers measure only the bending plane coordinate.

In the following sections we will discuss the spectrometer design, the trigger system and the tracking system with their different detector technologies.

Muon Spectrometer Design

As discussed in the first chapter, the experiments at LHC have a very rich physics potential related to the discovery of the Higgs bosons and supersymmetric particles, and to the accurate study of CP violation in the Beauty sector [22]. Most of these processes imply the presence of muons in the final states and the ATLAS Muon Spectrometer is an essential device to enhance the physics reach of the experiment. The momentum range spanned by the interesting reactions is very wide, going from few GeV/c of the muons produced in B decays to few TeV/c of the muons produced in new heavy gauge bosons decays. For these reasons the muon system needs to satisfy the following requirements:

- a transverse-momentum resolution of few percent in the low p_T region. This limit is set by the requirement to detect the $H \rightarrow ZZ^*$ decay in the muon channel with high background suppression;
- at the highest p_T the muon system should have sufficient momentum resolution to give good charge identification for $Z^{'} \rightarrow \mu^+\mu^-$ decay;
- a pseudo-rapidity coverage $\mid \eta \mid < 3$. This condition guarantees a good detection efficiency for high-mass objects decaying into muons with all of them within the acceptance region;
- a hermetic system to prevent particles escaping through detector cracks;
- a 3-dimensional measurement of spatial coordinates;
- a low rate of both punch-through hadrons and fake tracks;
- a trigger system for almost all physics channels. For B physics a maximal coverage and efficiency for muons with transverse momentum down to 5 GeV is required.

The spectrometer design has been optimized to reach a high resolution and robust stand-alone muon identification and it is illustrated in figure 2.7.

Figure 2.8 shows the different contributions to the muon transverse momentum resolution.

For momenta below 10 GeV/c, the energy loss fluctuation, for muons crossing the calorimeters, limits the resolution to about 6-8$\%$. The multiple scattering in the materials limits the resolution to about 2$\%$. While, for higher momenta, the intrinsic spatial accuracy of the chambers and the knowledge of their calibration and alignment give the largest contribution to the resolution. At 1 TeV/c momentum muon is measured with 10$\%$ resolution, which was one of the more stringent requirements on the spectrometer design.

Muon momentum resolution at low momenta (below 100 GeV/c) can be improved by using a combined reconstruction of the muon trajectory exploiting also the inner tracker measurements. In this case the Muon Spectrometer is used mainly for the identification of the muon. In figure 2.9 the stand-alone and the combined momentum resolutions are combined as a function of the transverse momentum in the region $\mid \eta \mid < 1.1$. In ATLAS the muon momentum is measured with a precision of about 4$\%$ up to 250 GeV/c.

The spectrometer is divided into three regions: the Barrel, covering the rapidity region $\mid \eta \mid \leq 1$ and two End-Caps, covering the rapidity regions $1 < \mid \eta \mid < 2.7$. In the Barrel, the toroidal field is produced by eight very large superconducting coils arranged in a open geometry (figure 2.10).

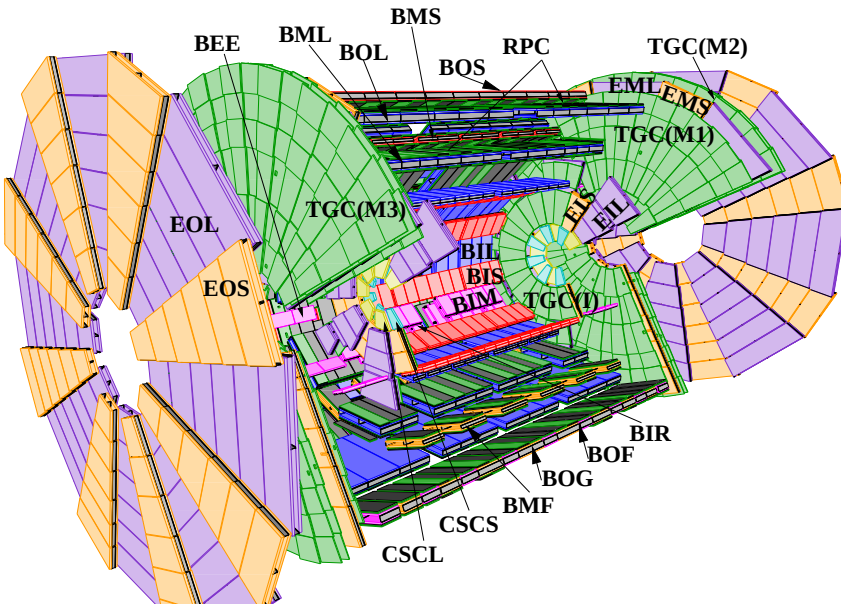

Figure 2.7: Configuration of the muon spectrometer.

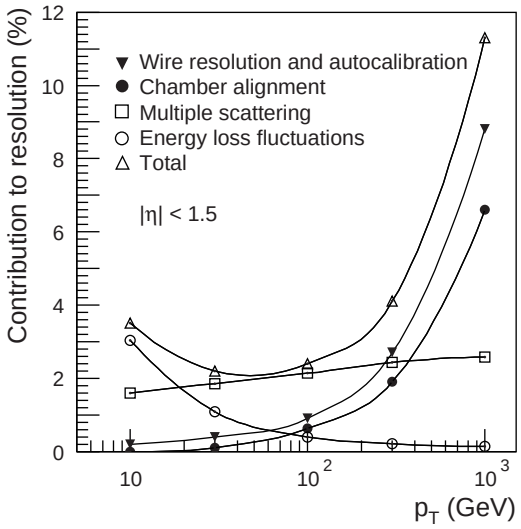

Figure 2.8: Contributions to the resolution as function of the muon momentum.

The field integral in the Barrel varies between 2 and 5 T m, with large variations as a function of the azimuth angle. The muon trajectory is sampled in three high precision measuring stations placed inside the toroid, equipped with

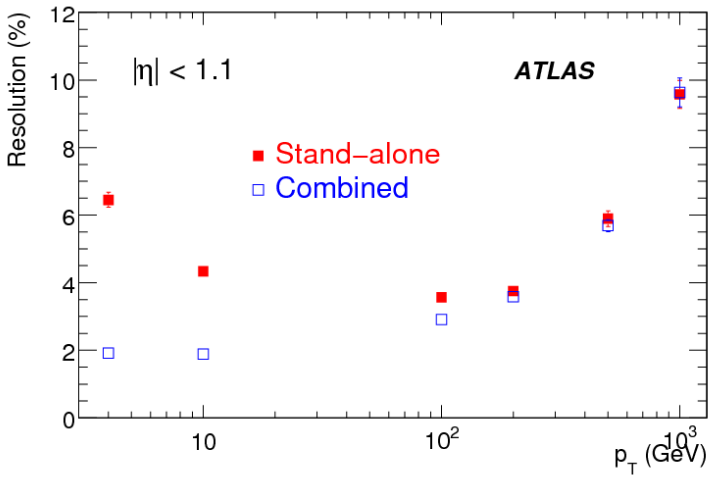

Figure 2.9: Stand-alone and combined fractional momentum resolution as a function of the transverse momentum.

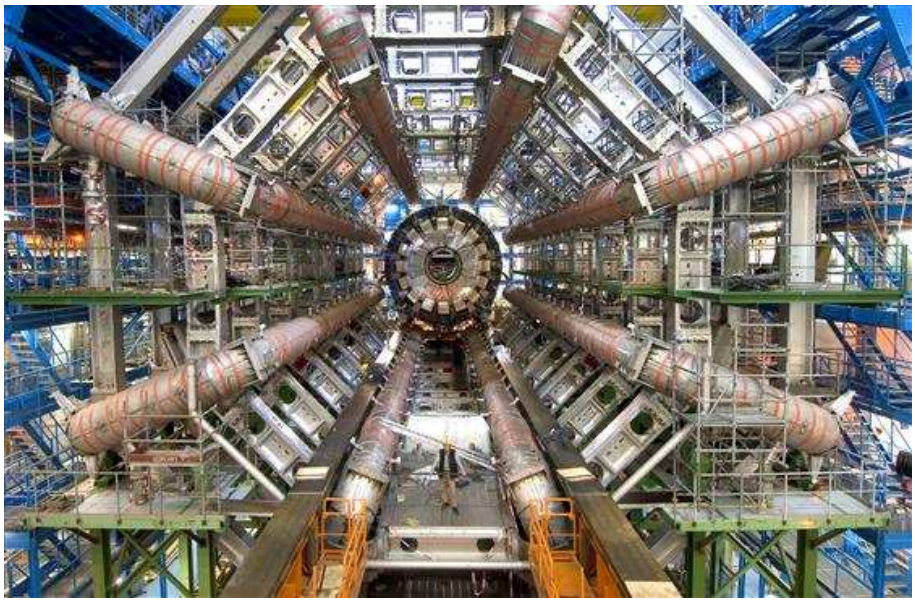

Figure 2.10: The eight barrel toroid magnets photographed in November 2005 during the detector installation phase.

Monitored Drift Tubes (MDT, see section 2.2.4) and arranged in three cylindrical layers around the beam axis. Each station measures the muon positions with a precision of about 50 μm in the bending plane. In the two outer stations of the Barrel spectrometer, specialized trigger detectors (Resistive Plate Chambers,

RPCs) are present. In the middle station two layers, each comprising two RPC detectors (RPC doublet), are used to form a low-p_T trigger ($p_T > 6$ GeV/c). In the outer station only one layer with one RPC doublet is used to form the high-p_T trigger ($p_T > 10$ GeV/c) together with the low-p_T station. RPCs measure both the bending and non-bending coordinate in the magnetic field. Trigger formation requires fast (< 25 ns) coincidences pointing to the interaction region both in the bending and non-bending planes.

In the End-Cap regions, two identical air core toroids are shown in figure 2.11 and are placed on the same axis of the barrel toroid (corresponding to the beam direction).

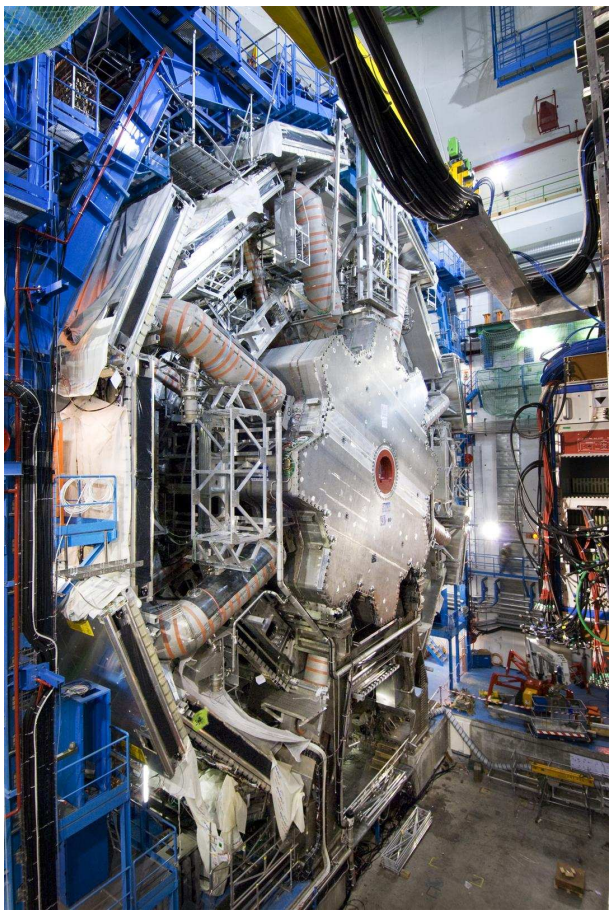

Figure 2.11: View of the ATLAS Cavern with the EndCap Magnets in place (July 2007).

The measurement of the muon momentum in the End-Cap region is accomplished using three stations of chambers mounted to form three big disks called 'wheels'. These are located normal to the beam direction, and measures the angular displacement of the muon track when passing in the magnetic field (the toroids

are placed between the first and the second tracking stations).

In the End-Cap regions the toroids volume are not instrumented and a sagitta measurement is not possible but an angular measurement is performed. MDT chambers are used for precise tracking in the full angular acceptance, with the exception of the inner station where the region $2 < \mid \eta \mid < 2.7$ is equipped with Cathode Strip Chambers (CSC, see section 2.2.4) which exhibit a smaller occupancy. The CSCs have spatial resolution in the range of 50 μm.

The trigger acceptance in the End-Caps is limited to $\mid \eta \mid < 2.4$ where Thin Gap Chambers (TGC, see section 2.2.5) are used to provide the trigger. The TGCs are arranged in two stations: one made of two double gap layers, used for the low p_T trigger, and one made of a triple gap, used in the high p_T trigger in conjunction with the low p_T stations. The high p_T station is placed in front of the middle precision tracking wheel and the low p_T station is behind it. The TGCs provide also the measurement of the second coordinate and for this reason there is a TGC layer also in the first tracking wheel.

Tracking Chambers

Monitored Drift Tubes: MDT

The precision tracking is performed, in almost the whole spectrometer, by the Monitored Drift Tubes (MDTs). The basic detection element is an aluminium tube of 30 mm diameter and 400 μm wall thickness, with a 50 μm diameter central W-Re wire [23]. The lengths of the tubes vary in the spectrometer from 0.9 to 6.2 m. In each measuring station (barrel or end-cap), tubes are assembled in two multi-layers, which are kept separated by a rigid support structure (spacer frame) that provides accurate positioning of the drift tubes with respect to each other and support to the components of the alignment system (see figure 2.12).

Multi-layers are made of 3 or 4 tube layers, with four-layer chambers being used in the inner stations. The mechanical accuracy in the construction of these chambers is extremely tight to meet the momentum resolution requirements of the spectrometer. Using an X-Ray Tomography [24], which measure the wire position with an accuracy of less than 5 μm, the precision in wire position inside a chamber has been checked to be higher than 20 μm r.m.s. The required high p_T resolution crucially depends also on the single tube resolution, defined by the operating point, the accurate knowledge of the calibration and the chambers' alignment.

The MDT chambers use a mixture of Ar-CO_2 (93% – 7%), kept at 3 bar absolute pressure, and operate with a gas gain of 2×10^4. These parameters were chosen in order to match the running condition of the experiment: the MDTs can sustain high rates without ageing effects [25], and with little sensitivity to space

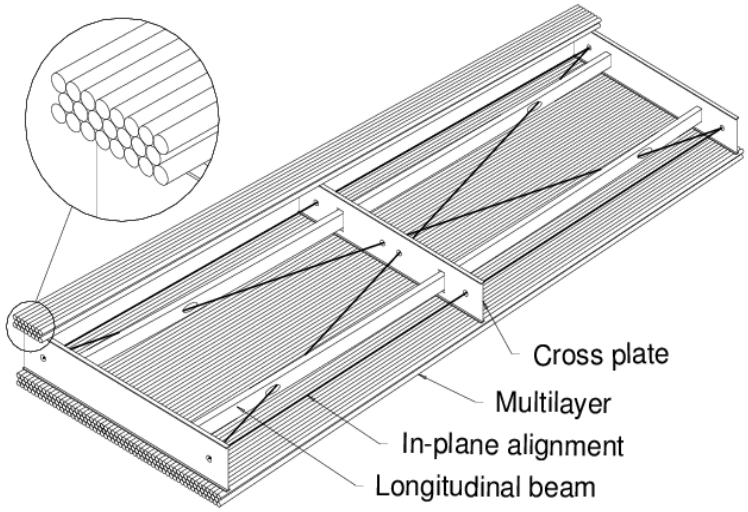

Figure 2.12: Scheme of a Monitored Drift Tube chamber.

charge. The single tube resolution is below 100 μm for most of the range in drift distance, and the resolution of a multi-layer is approximately expected equal to 50 μm.

In order to take advantage of such tracking accuracy, covering a surface per chamber up to 10 m^2, an extremely accurate mechanical construction is needed. Furthermore, precise monitoring of the operating conditions is required for best performance. Among these issues, very important is an excellent alignment system that enables the monitoring of the position of the different chambers in the spectrometer with a precision higher than 30 μm. Regarding this system, the aluminium frame supporting the multi-layers is equipped with RASNIK [26] optical straightness monitors. These monitors are formed by three elements along a view line: a laser that illuminates a coded target mask at one end, a lens in the middle and a CCD (Charged Coupled Device) sensors at the other end. This system provides a very accurate measurement of the relative alignment of three objects (1 μm r.m.s.) and is used both for checking the chamber deformation (in-plane alignment) and the relative displacement of different chamber (projective alignment). The chambers are also equipped with temperature monitors (in order to correct for the thermal expansion of the tubes, and for the temperature of the gas), and with magnetic field sensors (in order to predict the E$\times$B effect on the drift time).

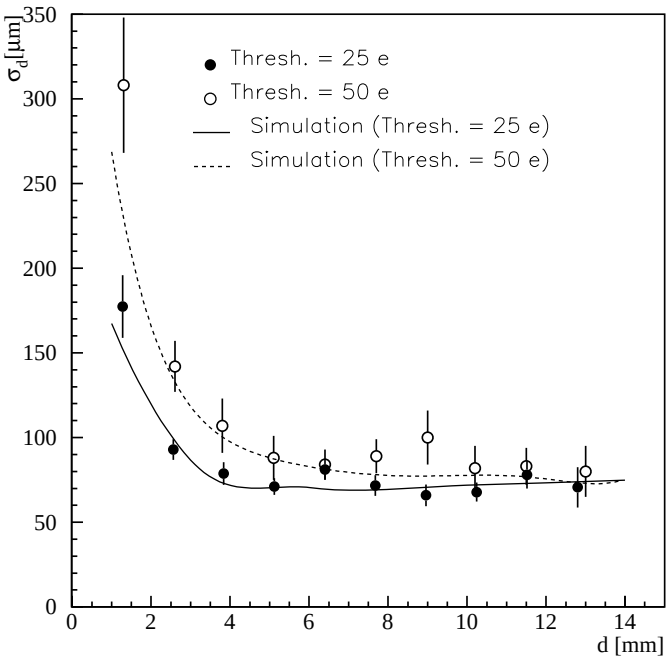

Figure 2.13: MDT resolution as a function of the drift distance. The curves correspond to two discriminator threshold settings.

Cathode Strip Chambers: CSC

The background rate in $2 < \mid \eta \mid < 2.7$ region of the inner tracking wheel of the End-Cap is large enough to demand the use of a precision detector with high granularity. A multi-wire proportional chamber with cathode strip read-out is used (the Cathode Strip Chamber). The anode wire pitch is 2.54 mm, and the pitch of the read-out strip is 5.08 mm. Cathode planes are equipped with strips orthogonal to the wires and the precision coordinate is obtained by measuring the charge induced on the strips making charge interpolation between neighbouring strips (the structure is shown in figure 2.14). Typical resolution obtained with this readout scheme is about 50 μm. The smallness of the basic cell implies also small maximum drift time (about 30 ns) which is beneficial to keep the chamber occupancy low. The gas mixture is composed of Ar (30$\%$), CO_2 (50$\%$) and CF_4 (20$\%$) and the wires are supplied by 2.6 kV, resulting in a gas gain of about 10^4. In ATLAS the CSCs are arranged in two layers, each containing 4 layers of cells, enabling 8 high precision measured points on a single track.

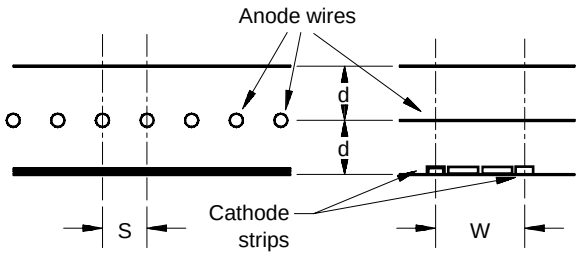

(a) Schematic diagram of the cathode strip chamber.

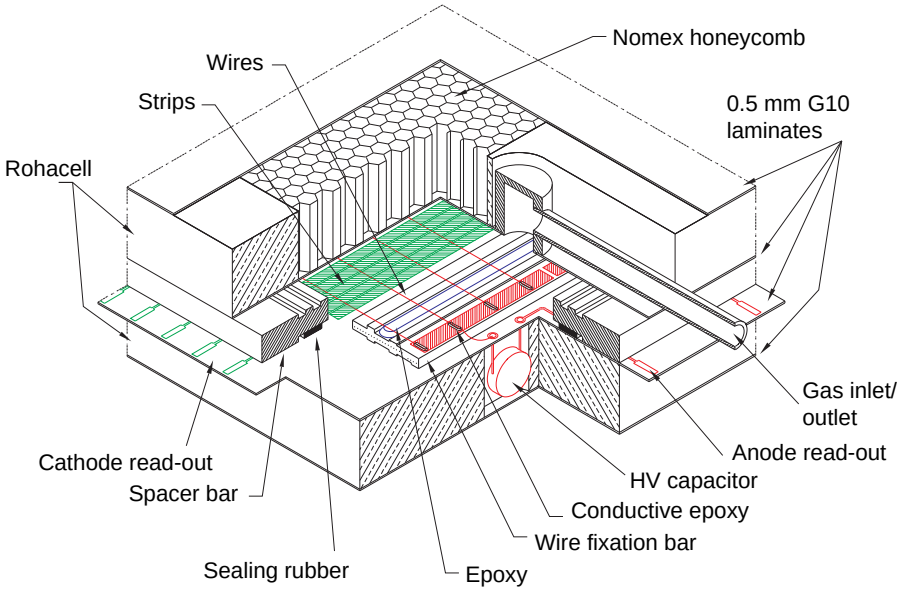

(b) Cutout view of a single CSC layer showing the construction details.

Figure 2.14: Structure of the cathode strip chambers.

2.2.5 Trigger Chambers

The ATLAS physics program demands for a highly flexible trigger scheme with different programmable transverse momentum thresholds. At low luminosity a 6 GeV/c threshold for two or more muons is adequate for Beauty physics, while higher transverse momentum thresholds (20 GeV/c) will be used for Higgs search and high p_T physics measurements. The muon trigger in ATLAS is organized in three level. The first level trigger (LVL1), implemented in hardware, uses reduced-granularity data, coming only from the trigger detectors. The second level (LVL2) trigger uses software algorithms exploiting the full granularity and precision data from most of the detectors, but examines only the detector region flagged at the LVL1 as containing interesting information (Region of Interest, RoI). The third level trigger or Event Filter (EF) reconstructs muons applying the same refined algorithms of the offline reconstruction in the RoI identified by LVL2. Typical rates at the three trigger levels are 75 kHz (LVL1), 1 kHz (LVL2) and 100Hz (EF).

The LVL1 trigger uses specialized trigger detectors: RPCs in the Barrel and TGCs in the End-Caps. They are both characterized by fast response, needed to handle background and to associate tracks to the LHC bunch crossing. The trigger scheme used in both the Barrel and the End-Caps is illustrated in figure 2.15.

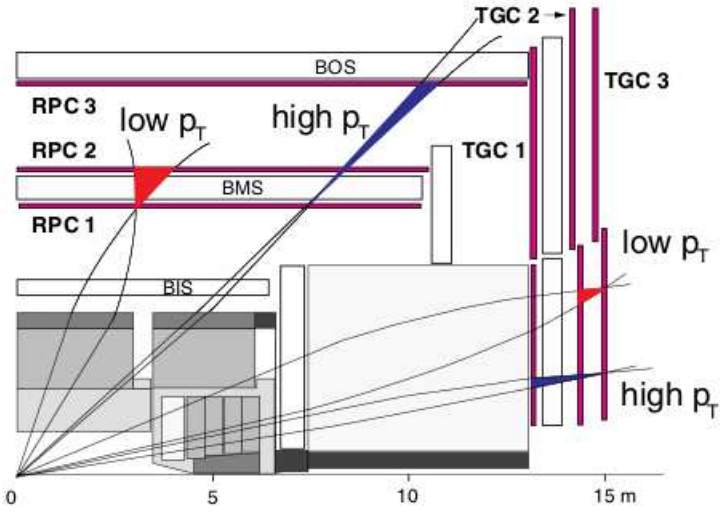

Figure 2.15: Trigger scheme for high and low p_T thresholds in the Barrel and in the End-Caps.

In the barrel, three double layers of detectors are used by the trigger system. The low p_T trigger uses predefined coincidence patterns in both projections, con-

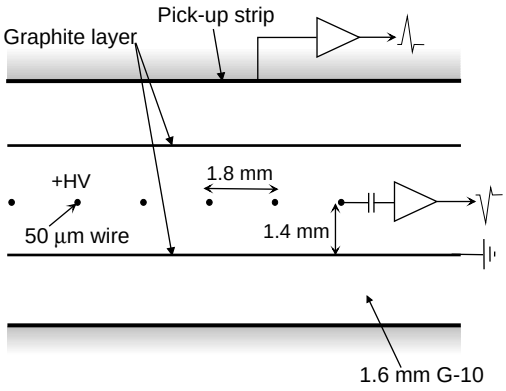

Figure 2.16: TGC structure showing positions of anode wires, graphite cathodes, G-10 layers and a pick-up strip, orthogonal to the wires.

sidering the RPC middle station only. The momentum resolution is about 20% and is limited mainly by multiple scattering and by fluctuation of the energy loss in the calorimeters. The high p_T trigger requires a spatial coincidence pattern considering the two RPC stations. At p_T of 20 GeV/c the momentum resolution is about 30% and is limited by the axial length of the interaction region and by multiple scattering in the central calorimeters. The same logic is applied to the trigger scheme in the End-Caps. The p_T threshold is defined by the width of the coincidence patterns and can be programmed. This width depends on the rapidity, and for a 20 GeV/c threshold it varies from about 40 cm in the Barrel to about 5 cm in the End-Caps.

Thin Gap Chambers: TGC

The Thin Gap Chambers are multi-wire proportional chambers with a smaller distance between the cathode and the wire plane compared with the distance between wires [27]. In fact, the distance between the cathode and the wires is 1.4 mm to be compared with the wires pitch, that is 1.8 mm, while the wire diameter is 50 μm (see figure 2.16).

The gas mixture is 55% CO_2 and 45% "n"-pentane, which results in a highly quenching gas mixture that permits the operation in saturated avalanche mode (see next chapter for detailed description of the gas detectors operation modes). Due to this operation mode, these detectors are not very sensitive to small mechanical deformations, which is very important for large detector as ATLAS [28]. The saturated mode has also two more advantages: the signal produced by a minimum ionizing particle has only a small dependence on the incident angle up to 40 degrees angle and the tails of the pulse-height distribution is less than 2% of the total. The chambers operate at a high voltage of about 3 kV. The operating conditions

and the electric field configuration provide a short drift time (< 30 ns), enabling a good time resolution. The readout of the signal is done both from the wires (which are grounded together in a variable number, according to the desired trigger granularity as a function of the pseudo-rapidity) and from the pick-up strips plane placed on the cathode. The wires and the strips are perpendicular to each other enabling the measurement of the orthogonal coordinates, however only the wire signal are used in the trigger logic.

Tests performed at high rate have shown single-plane time resolution of about 4 ns with 98% efficiency, providing a trigger efficiency of 99.6% [29].

Resistive Plate Chambers: RPC

The RPC are gaseous detectors providing a typical space-time resolution of 1 cm $\times$ 1 ns with digital readout. The active element of the RPC unit is a narrow gas gap formed by two parallel resistive Bakelite plates, separated by insulating spacers. The primary ionization electrons are multiplied in avalanches by a high, uniform electric field of typically 5 kV/mm. The gas mixture has been chosen in order to operate in saturated avalanche mode and is composed of three gases: 94.7% $C_2H_2F_4$, 5% C_4H_{10}, 0.3% SF_6. Tetrafluoroethane ($C_2H_2F_4$) has been chosen as main component since, in addition to satisfy safety requirements, exhibits moderately high primary ionization at low operating voltage. Moreover, the mixture contains isobutane (C_4H_{10}) as photons quencher and SF_6, in order to reduce the amount of delivered charge and inhibit the streamer development.

Amplification in avalanche mode produces pulses of typically 0.5 pC. Signals are readout via capacitive coupling by metal strips on both sides of the detectors. In ATLAS, RPC are mounted on MDTs with a mechanical structure that fix the relative position between chambers. In one readout plane strips (η strips) are parallel to the MDT wires and provide the bending view, while in the other plane strips (ϕ strips) are orthogonal to the MTD wires, providing the second-coordinate measurement which is also required for the pattern recognition. RPC detectors will be extensively described in the next chapter.

2.2.6 Trigger and data acquisition system

The 40 MHz proton-proton collision rate of LHC produces a huge amount of readout signals in ATLAS detector: a trigger system organized on three distinct levels (*Level-1*, *Level-2* and *Event filter*) has been implemented to select potentially interesting events (see figure 2.17).

The first level trigger

The first level (L1) trigger (schematized in figure 2.18) is implemented on detector with custom made electronics board and it uses data from calorimeters and muon trigger chambers.
The calorimeter trigger uses reduced granularity informations from all the calorimeters and searches electrons, photons, jets with high E_T or events in which there is a large E_T^{miss} and a large total transverse energy. The trigger algorithm is based on the multiplicity of hits from clusters found in the calorimeters and from global energy deposition.
The level 1 muon trigger uses signals of muon trigger chambers RPC and TGC and searches for coincidence of hits in trigger station consistent with high-p_T muons coming from interaction point. There are six independently programmable p_T thresholds. Information from all muon trigger sectors are combined by the Muon Central Trigger Processor Interface (MUCTPI).
Informations from calorimeter and muon triggers are combined by the Central Trigger Processor (CTP) which makes the overall L1 trigger accept decision. The detector read-out system can handle a maximum L1 accept rate of about 100 kHz.

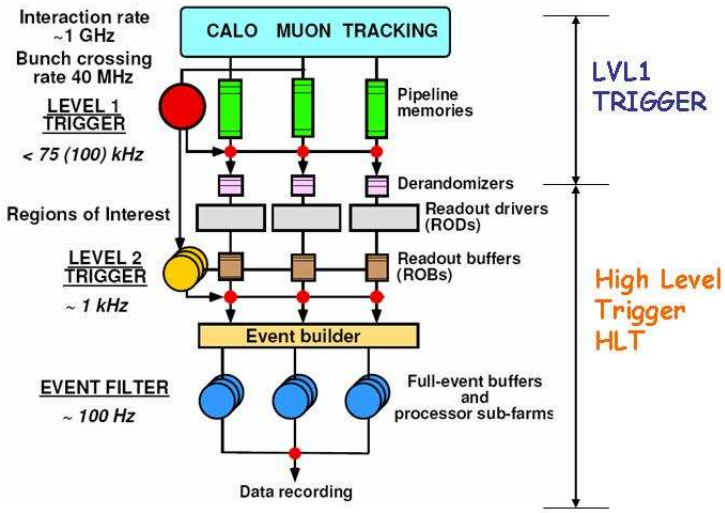

Figure 2.17: General view of three levels of the ATLAS trigger system.

The level-1 trigger must operate with a maximum latency of 2.5 μs and has to identify without ambiguity the bunch crossing of interest. Data of all detectors channels are retained in pipeline memories (located on or near the detectors) while the trigger decision is being formed. If an event is accepted by level-1 trigger, the *region of interest* (RoI), i.e. the information about the geometry location of trigger object is delivered to level-2 trigger.

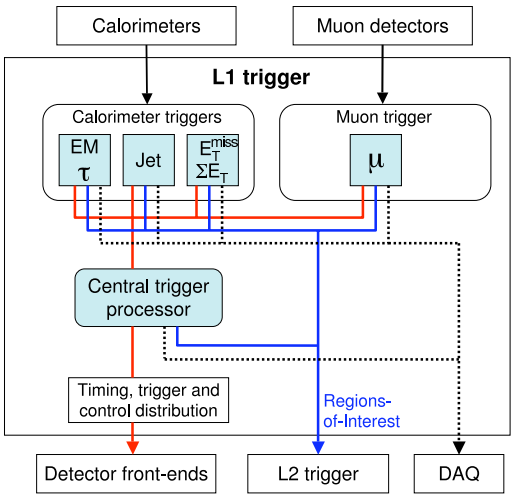

Figure 2.18: Block diagram of the level-1 trigger. Red, blue and black lines are, respectively, the output path to detector front-ends, L2 trigger, and data acquisition system.

High level trigger and data acquisition system

The second level of the trigger uses informations from all the subdetectors with full granularity and precision, in the regions of interest defined by level-1 trigger (in this way the amount of data analyzed is about 2% of the total). The level-2 trigger has an average event processing time of about 40 ms and reduces the trigger rate to approximately 3.5 kHz.

After that, all event data (associated with a given event) are collected and assembled in a formatted structure by the *sub farm input* (SFI) application. Built events are processed by the event filter processing farm. In this step, unlike the L2 trigger, the standard ATLAS analysis and reconstruction program is used. In this final state, the event rate is reduced to roughly 200 Hz and selection procedure has an average event processing time of about four seconds. Data of events which passed the event filter selection criteria are received by the *event filter output nodes* (SFO) and are written on files located on CERN central data recording facility. Data are separated on various *streams* and written on different files depending of the trigger signature (e.g. muons stream, minimum bias stream, etc.). Special streams are the *calibration stream* and the express stream. The calibration stream is not recorded at the end of the full trigger chain but at level-2 step and it is used for detector calibration. The express stream contains a subset of the events selected by event filter (in fixed percentage for every streams) and it is reconstructed and analysed promptly as soon as SFO closes the data files on disk. This allows to have a quickly feedback of the quality of data taken and the detector status.

3
ATLAS RPC trigger chambers

3.1 Resistive Plate Chambers

Resistive Plate Chambers (RPC) have been developed in 1981 by R. Santonico and R. Cardarelli [30]. They are gaseous parallel plate detectors with a time resolution of $\sim$ 1 ns, consequently attractive for triggering and Time-Of-Flight applications.

Their main advantages, compared to other technologies, consist in their robustness, construction simplicity and relatively low cost of the industrial production. They are ideal to cover large areas up to few thousand square meters.

RPCs were originally used in streamer mode operation [31], then providing large electrical signals, requiring low gain read-out electronics and not stringent gap uniformity. However, high rate applications and detector ageing issues made the operation in avalanche mode absolutely necessary. This was possible thanks to the use of new highly quenching $C_2H_2F_4$-based gas mixture instead of the traditional Ar-based mixture and to the development of high gain read-out electronics.

RPC, similarly to Spark Chambers and Parallel Plate Avalanche Chambers, consist of two parallel plate electrodes made with high resistivity material, typically glass or bakelite.

The fundamental processes underlying RPCs are well known. A charged particle produces free charge carriers in the gas, which drift towards the anode and are multiplied in a uniform electric field induced by an external high voltage applied to the electrode plates. The propagation of the growing number of charges induces an electric signal on the read-out strips, which is amplified and discriminated by the front-end electronics.

The charge Q_0 reaching the electrode surface is locally removed from the electrode itself following an exponential law:

$$Q(t) = Q_0 e^{-t/\tau} \text{ with } \tau = \rho\varepsilon_0\varepsilon_r \tag{3.1}$$

where ρ is the electrode volume resistivity and ε_r and ε_0 are the relative permittivity of the resistive material and of the vacuum respectively. τ is defined as the time needed by the electrode to get charged again thus recovering the initial voltage in

the gap and varies from $\tau \approx 1$ s for glass resistive plates (for which the volume resistivity is $\rho \approx 10^{12}\ \Omega$ cm) to $\tau \approx 10$ ms for plastic-laminated plates (for which $\rho \approx 10^{10}\ \Omega$ cm).

3.2 The ATLAS RPC

The RPC gas volumes are made of two parallel bakelite plates, having a volume resistivity $\rho \simeq 10^{10\pm1}\ \Omega$ cm. They delimit a 2 mm gas gap filled with a gas mixture at atmospheric pressure. These plates are coated, on the external side, with a thin graphite layer with a surface resistivity ranging from 100 to 300 kΩ/cm^2. The graphite layer allows to uniformly apply the high voltage to the electrodes without screening the avalanche signal induced on metal strip readout panels. Moreover, the assembled RPC gas volume is filled with linseed oil, which is then slowly taken out. The resulting effect is the deposition of a thin layer of polymerized oil which smooths the inner bakelite surfaces. This is done in order to reduce the surface imperfections that strongly affect the detector dark current and noise counting rate. The readout panels are segmented into strips and simply pressed on the external electrode surface. The readout strips are placed on both sides of the gap and arranged in perpendicular directions in one side with respect to the other, allowing to measure the x- and y-coordinate of the ionizing crossing particle. Strip panels are separated from the graphite coating by an insulating PET (Polyethylene-Teraphtalate) foil.

A ATLAS RPC unit consists of two independent gas volumes, which are read-out by two orthogonal sets of pick-up strips (see bottom picture of figure 3.1).

Two detector layers of one RPC units are interleaved with three support panels. The support panels are made of a light-weight paper honeycomb and are held in position by a solid frame of aluminium profiles. Two external support panels interconnected by the aluminium profiles give the required stiffness to the chamber.

The RPC units, with the exception of the BMS units (see next section for the nomenclature), have a length in the transverse (ϕ) direction exceeding the maximum length (3200 mm) of the available bakelite. For this reason the gas volumes are divided in two segments along the ϕ direction with a 9 + 9 mm inefficient region between the two edge frames. The readout-strip panels are also segmented in the (ϕ) direction, including the case of the BMS chambers, in order to get an homogeneous trigger scheme for all chamber types. This gas volume segmentation reduces the η-strips time jitter by a factor of two.

Most of the RPC trigger chambers are made of two units. The two units forming a chamber have an overlap region of 65 mm to avoid dead areas for curved tracks (see upper picture of figure 3.1). Several RPC trigger chambers are made

of one unit only.

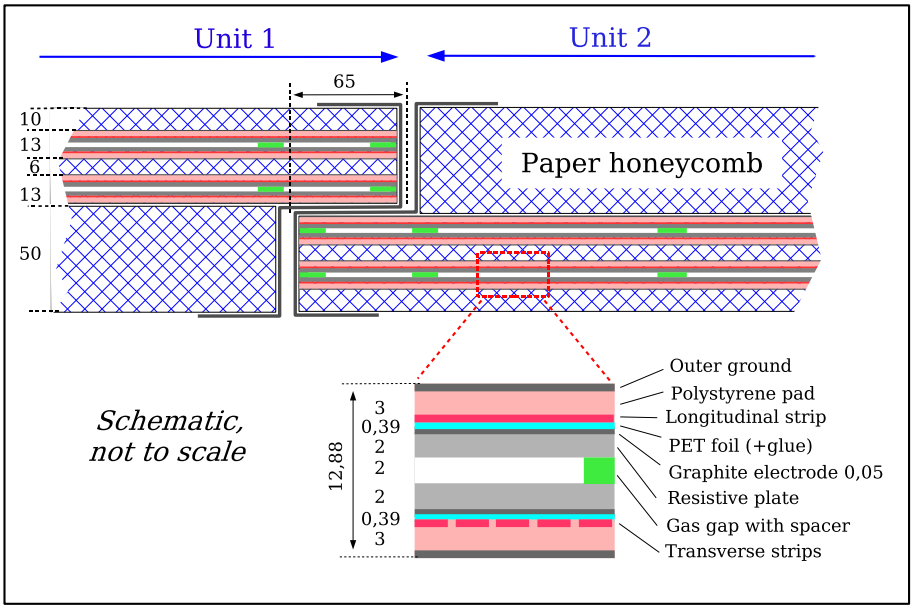

Figure 3.1: The cross-section of an ATLAS RPC chamber made of two units with two detection layers.

All standard RPC are assembled together with a MDT of equal dimensions in a common mechanical support structure: an example of the resulting layout is shown in figure 3.2. A number of small RPC chambers (special RPC‘s) are not paired with MDT‘s. These RPC’s are located around the magnet ribs and in the feet region, where MDT‘s cannot be installed because of lack of space. RPC‘s, requiring less space than MDT’s, are used in these regions to keep the trigger acceptance loss to a minimum.

3.2.1 Readout panels and front-end electronics

A RPC detector operating in avalanche mode produces signals of 5 ns full width at half-maximum with a time jitter of 1.5 ns while on the efficiency plateau. To preserve this high time precision, the pick-up strips must be high quality transmission lines with low attenuation and terminated at both ends with their characteristic impedance. The layout of a readout strip panel is shown in figure 3.3. The readout strips have a pitch of 25-35 mm and they are placed on a PET foil glued on a rigid polystyrene plate. The polystyrene plate is covered on the outside by an other foil PET and a copper sheet as ground reference. The strips are separated by a 2 mm gap with a 0.3 mm ground strip at the center to improve decoupling. This sandwich structure creates an impedance of about 25 Ω for the strips, slightly

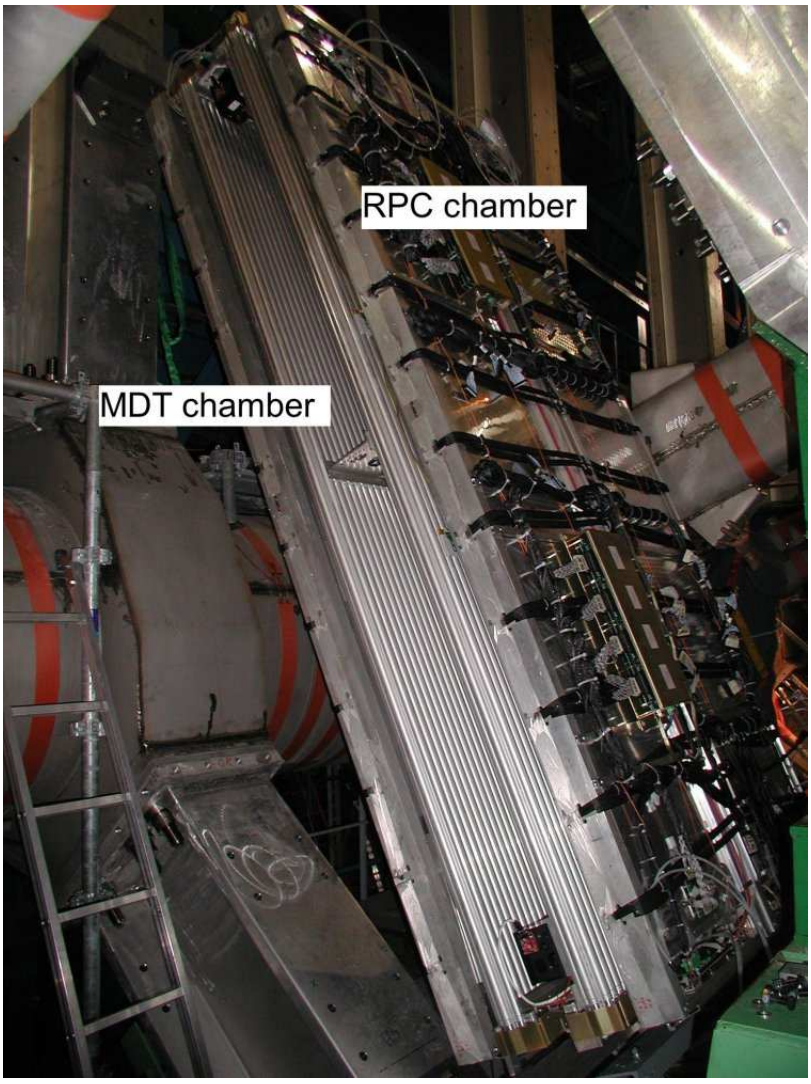

Figure 3.2: A RPC chamber coupled with a MDT drift tube chamber installed in the ATLAS detector.

depending on the width. The pick-up strips outside the PET layers are connected to the front-end electronics.

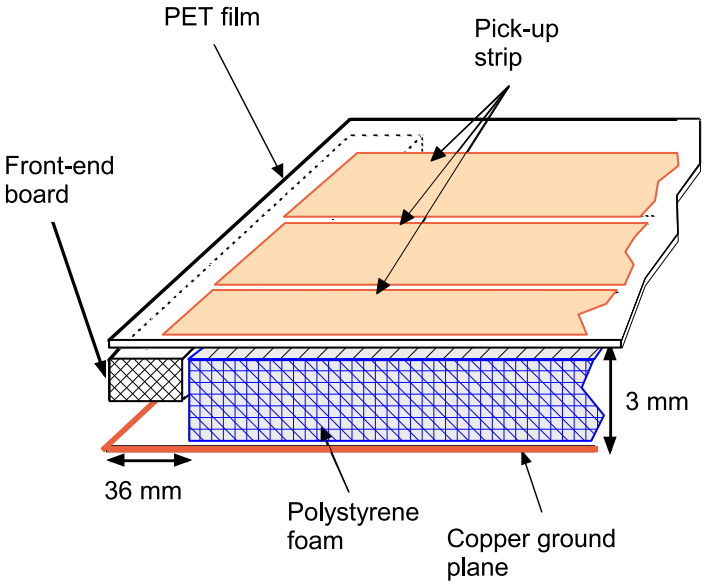

Figure 3.3: RPC read-out strip panel.

The front-end circuit is a three-stage shaping amplifier followed by a comparator. It is implemented by an eight-channel GaAs chip which is bonded on a printed circuit board and reading out eight strips. The frequency response of the GaAs-amplifiers has a maximum at 100 MHz with a 60 MHz bandwidth, well adapted to the rise time of the chamber signals. The front-end electronics input is coupled to the strips by a transformer integrated on the printed circuit and it matches the signal polarities of η-strips and ϕ-strips, which are opposite to each other [32] [33].

The ϕ-strips front-end output of two adjacent units are wired OR-ed. This is done to avoid unnecessary granularity and to adapt the RPC readout segmentation to the trigger sector segmentation as will be discussed in section 3.4. The ϕ-strip length and the relative time jitter is in average about half the η-strip relative time jitter, giving to the ϕ-strips a more precise timing.

In order to be used for the trigger, a signal from a RPC has to be compared with those in the two other RPC‘s along the path of the particle. This task is accomplished by an electronic system of fast coincidence units placed on top of the chambers. A detailed discussion of the RPC trigger system is given in section 3.4.

3.3 ATLAS RPC detector layout

The muon detector chambers are arranged such that particles from the interaction point traverse three stations of chambers. In the barrel the chambers are arranged in three concentric cylinders around the beam axis called BI (Barrel Inner), BM (Barrel Middle), and BO (Barrel Outer). RPC planes are installed in the Middle and Outer stations of the Muon Spectrometer always mechanically associated with MDT precision chambers (except for some "special" chambers). Two RPC planes are integrated with MDT in the Middle stations and one RPC plane only in the Outer stations.

The system is subdivided azimuthally into 16 sectors numbered from 1 to 16. The sector number increases in the direction of increasing ϕ with the number 1 corresponding to coordinate $\phi = 0$. The odd sector (called "large sectors") are located between barrel coils and the even sectors (called "small sectors") are covered by the coils (figure 3.4).

The naming convention for RPC chambers are than BMS (Barrel Middle Small), BOS(Barrel Outer Small), BML(Barrel Middle Large) and BOL (Barrel Outer Large), except for sector 12 and 14 where the ATLAS feet are located and the naming convention is BMF (Barrel Middle Feet) and BOF (Barrel Outer Feet).

In section 4.3, will be detailed how the hardware detector granularity is translated in the detector software description and thus in the histograms naming convention used in the following of this work.

3.4 ATLAS Barrel Muon Trigger

The trigger algorithm is based on temporal and spatial coincidences of strip belonging to different RPC planes (see figure 3.5). The number of planes is chosen in order to minimize accidental coincidences and optimize the trigger efficiency. To reduce the number of accidental counts, the trigger operates in the bending coordinates η and in the non-bending coordinate ϕ separately, but the trigger decision requires both to be satisfied. The trigger algorithm can be divided into two parts, respectively called low-p_T trigger and high-p_T trigger, depending on the value of the particle transverse momentum. This distinction was made in order to optimize the trigger according to the particles curvature and their loss of energy through the materials.

In case of low-p_T tracks, the algorithm uses information generated by the two RPC planes of the Middle stations (Pivot plane and low-p_T plane in figure 3.5). In the bending view η, if a RPC hit is detected in the doublet strips η of the Pivot plane, a fast RPC hit search is made in the doublet strips η of the low-p_T plane. The search is done with a spatial window (coincidence window or trigger

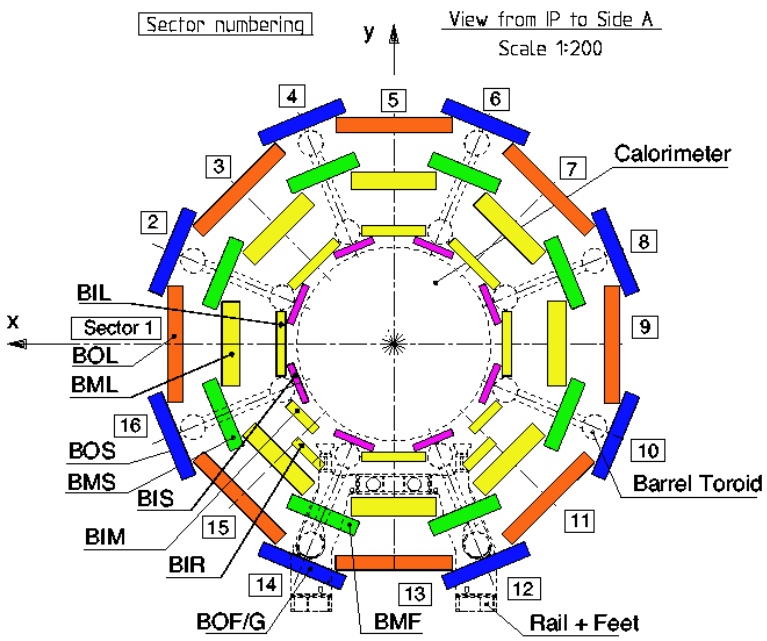

Figure 3.4: Cross-section of the barrel muon system perpendicular to beam line.

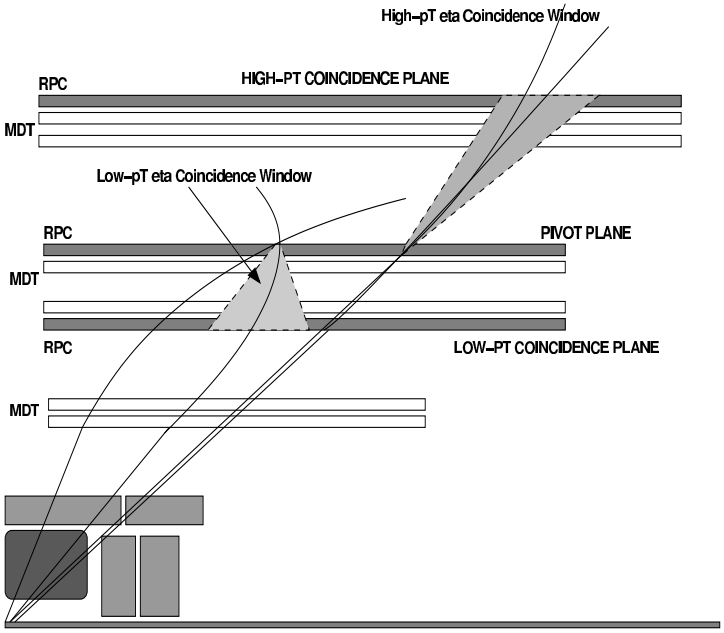

Figure 3.5: The muon barrel trigger algorithm

road) whose center is given by a hypothetical particle with infinite momentum

that travels from the point of interaction to the Pivot hit. The width of the window is programmable and the particles are selected depending on the p_T (a smaller window width gives a higher cut in p_T). The relationship between the window width and p_T cut is obtained through Monte Carlo simulations for each Pivot strip (see figure 3.6).

The trigger system can be programmed up to three windows simultaneously (corresponding to three different p_T threshold values). The transverse momentum for low p_T particles can varies between 5 and 10 GeV. To deal with the cavern background generating low-energy particles, the trigger signal is required to be revealed in at least 3 out of 4 layers.

The algorithm in the non-bending view ϕ is identical to that described above for η view, except that it links together ϕ strips belonging to adjacent chambers realizing a logical-or. There could be up to three chambers in logical-or, this corresponds to the maximum number of chambers along η that a muon deflected in the magnetic field can cross. The ϕ view logical-or is realized internally by the trigger and readout electronics and only for low-p_T and high-p_T planes (see figure 3.7). Instead, the ϕ view wire-or is realized by cabling on the chambers and for all three RPC planes (see figure 3.7).

In case of high-p_T tracks, the algorithm uses information generated by the high-p_T plane, requiring at least 1 out of 2 layer and the low-p_T trigger pattern. The algorithm used to search for the hit on high-p_T plane is quite similar to that used previously and is based on the coincidence window concept. Again, it is possible to program up to three coincidence windows at the same time, for various values of the momentum cut. The transverse momentum for high-p_T particles varies between 10 and 40 GeV.

The system is then able to resolve up 6 windows simultaneously for each view. The trigger algorithms are realized by implementing coincidence matrix between the signals coming from strip of the same view but belonging to different planes. Next paragraph will detail the trigger hardware layout.

3.4.1 Trigger hardware implementation

The differential signals coming from the front-end electronics are sent to an ASIC [1] named Coincidence Matrix (CMA). The CMA's are used to open a time coincidence window between strips, generate the trigger signal, locate the bunch-crossing and store the data waiting for the level-1 accept (L1A) decision.

Because of the coincidence windows overlapping, a RPC chamber must send its signals to more than one CMA. For this reason, the output signals from low-p_T and high-p_T RPC planes are readout by splitters. The splitters are designed to

[1] ASIC: Application Specific Integrated Circuit.

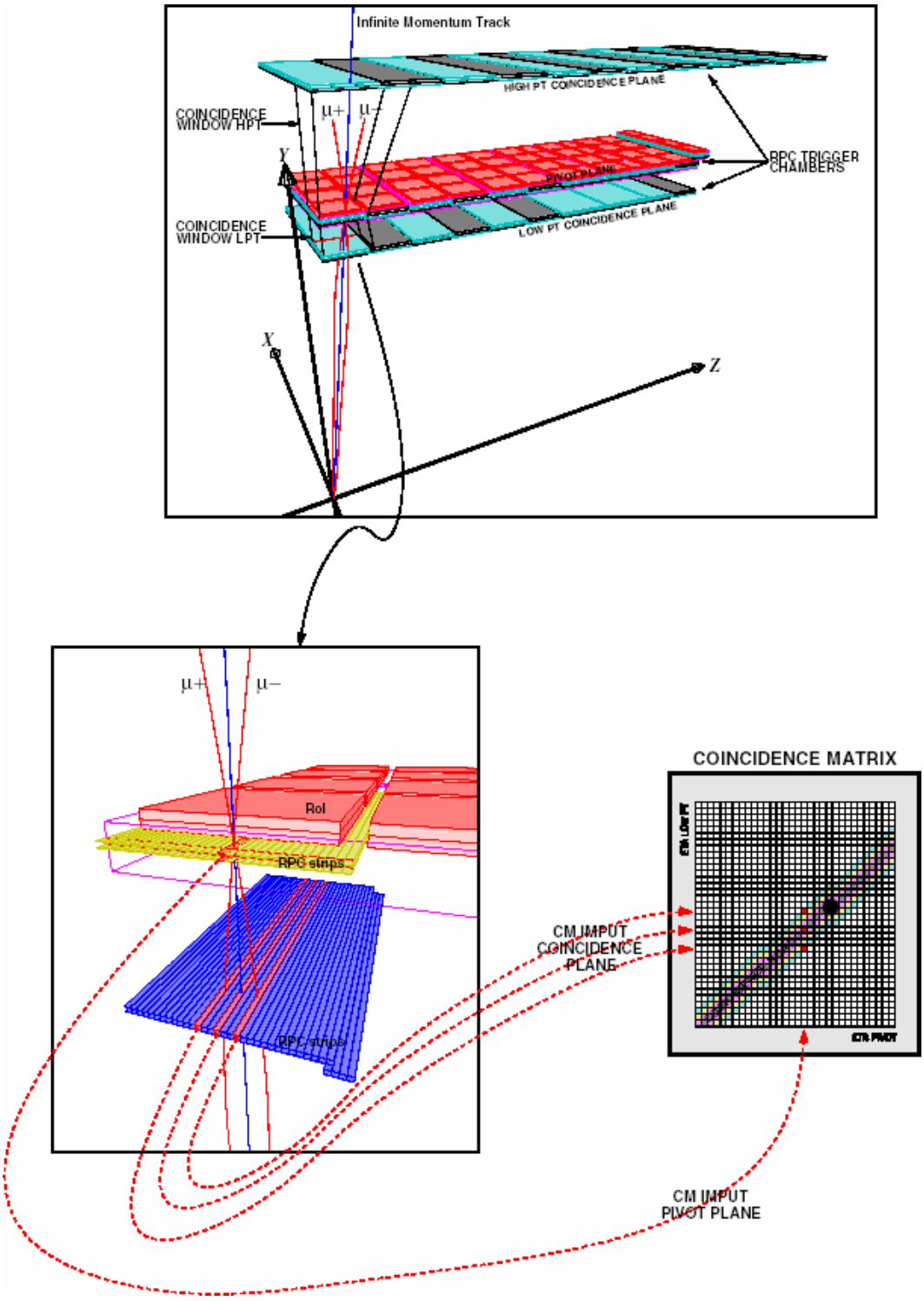

Figure 3.6: Simulated Low-p_T trigger event.

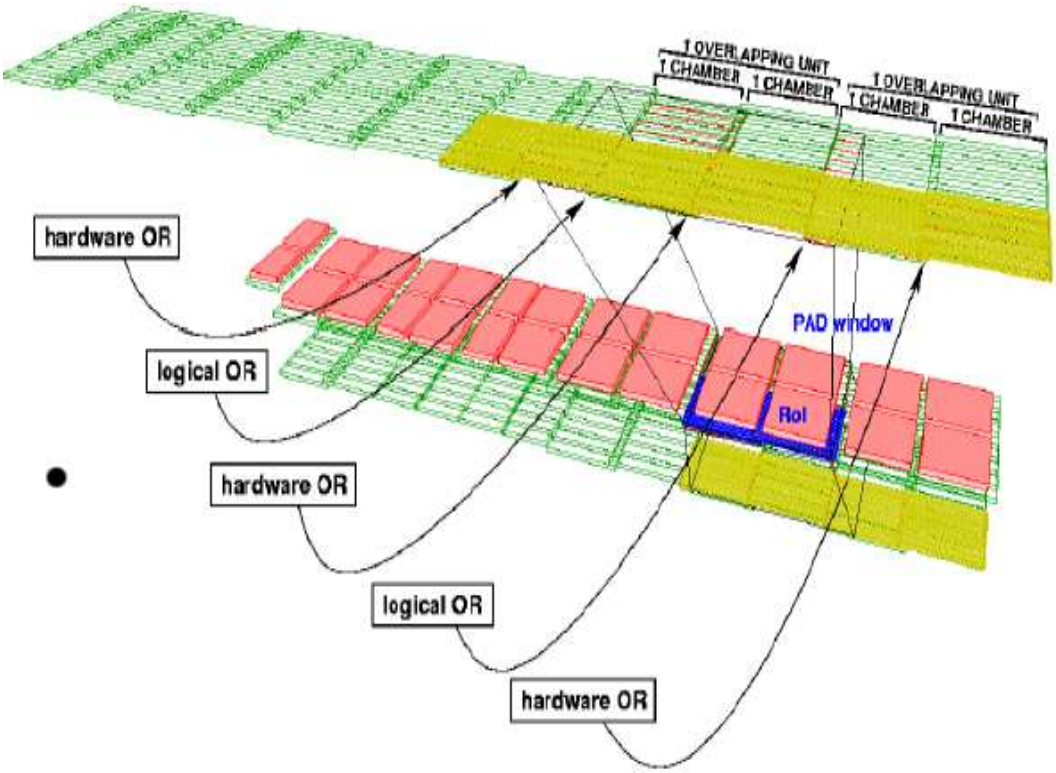

Figure 3.7: Logical-or and wired-or in ϕ views along the η direction.

duplicate the signal and drive more than one CMA. Another task of the splitter is to convert from ECL [2] logic to LVDS[3] logic the RPC front-end signals. The pivot RPC plane is directly connected to the CMA and a splitter is not required.

The pivot and low-p_T RPC planes are readout by 4 CMA's (2 for η view and 2 for ϕ view) and mounted on the same trigger box named low-p_T PAD. The task of the low-p_T PAD is to take data from the four coincidence matrix and send them to the high-p_T PAD.

The high-p_T RPC plane signals and the low-p_T CMA trigger signals are readout by 4 high-p_T CMA mounted on the high-p_T PAD. The high-p_T PAD, after processing, sends data and triggers serially via optic fiber to the off-detector electronic, in a room outside the detector. In this room the signals are received by the Sector Logic (SL) and the Read Out Driver (ROD) modules. The trigger signals are processed and shipped to MUCTPI (MUon Central Trigger Processor interface), and hence, ultimately, to the CTP (Central Trigger Processor) which has the task of taking the final trigger decision.

More specifically, the high-p_T PAD, through a FPGA [4], takes data from the 8 CMA, executes the trigger logic between the two views, selects the greater trigger threshold, solves overlaps and sends outgoing data and trigger signals. Figure 3.8 shows the structure of an ATLAS RPC trigger sector. In particular, a PAD, mounted on top of a RPC chamber, occupy half chamber along the ϕ direction and contains 4 CMA, which manages to cover an area $\Delta\eta \times \Delta\phi \approx 0.2 \times 0.2$, which includes 4 Regions of Interest (RoI). The RoI is the space region in wich the level-1 trigger identify possible interesting events and cover a sector of $\Delta\eta \times \Delta\phi \approx 0.1 \times 0.1$, while a CMA η covers a sector $\Delta\eta \times \Delta\phi \approx 0.1 \times 0.2$ and a CMA ϕ covers a sector $\Delta\eta \times \Delta\phi \approx 0.2 \times 0.1$. On ATLAS there are in total 832 PAD and 1664 RoI.

The Sector Logic module collects signals from all PAD's of the same trigger sector (7 PAD's for large sector, 6 PAD's for small sectors) and has the task of:

- Resolve trigger overlaps in η and indicate possible overlays with the adjacent sector.
- Select the muon with the greater p_T threshold and associate it to the triggered ROI.
- Select the muon with the second highest p_T threshold and associate it to the triggered ROI.

Once the data triggers were elaborated by the Sector Logic module, they are sent, via LVDS logic, to the MUCTPI, which receives information from all 64

[2] Emitter-Coupled Logic: is the logic family used for signals coming from RPC front-end.
[3] Low-Voltage Differential Signaling.
[4] Field Programmable Gate Array

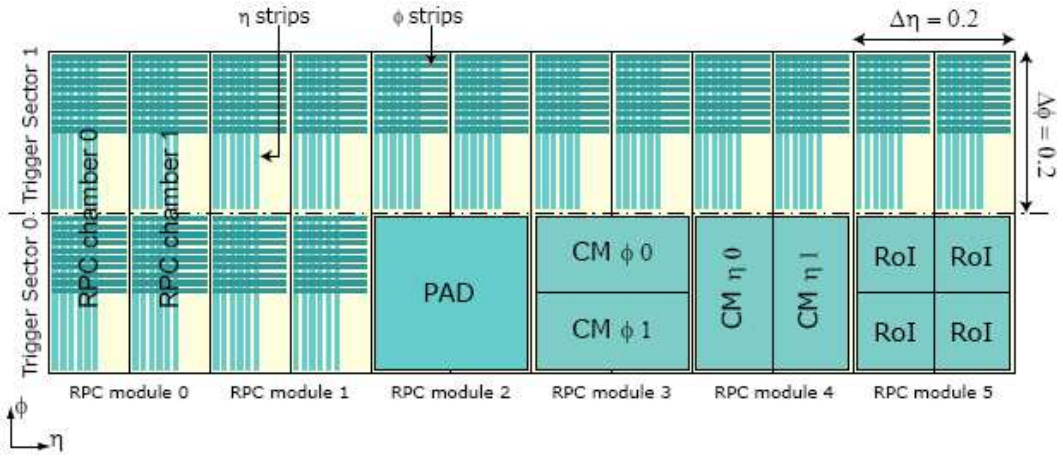

Figure 3.8: Segmentation of ATLAS RPC small sector.

barrel Sector Logics and all 144 end-cap Sector Logic. The MUCTPI has the task of:

- Resolve overlaps between adjacent Sector Logic.
- Select up to seven candidates for all six p_T threshold.
- Read during a time window programmable up to two bunch-crossing (this in order to set the timing of the system and monitor directly the activity of the trigger chambers).
- Align temporally data from different sectors and associate the right ROI.

The latency time of the trigger data in the MUCTPI should not exceed 8 bunch-crossing. The muon trigger data is then sent to the CTP, which together with the calorimetry trigger data built-up the final trigger decision.

4
RPC Offline Monitoring

The RPC off-line monitoring developed in this thesis covers basic aspects of the ATLAS RPC detector, such as electronics channels and readout strip response, and its standalone tracking capability [1]. The RPC off-line monitoring is part of the ATLAS official software and data processing which are briefly described in Section 4.1.1.

In Section 4.2 the main purpose and setting of the four software algorithms, which compose the RPC off-line monitoring, are presented. In Section 4.3 an overview of the RPC detector and readout electronics granularity is presented together with the detailed single readout strip and single channel histograms used for RPC commissioning with cosmics. In Section 4.4 the monitoring of the RPC and MDT signals correlation is presented and in section 4.5 is reported the RPC tracking algorithm and its use to evaluate the RPC efficiency.

In Section **??** simulated cosmic and commissioning data monitoring plots are compared, together with the validation of the techniques used to measure the efficiency.

4.1 ATLAS software infrastructure

4.1.1 The Athena framework

The ATLAS reconstruction software framework is called Athena [34]. It is used for a variety of purposes, including high-level triggering, simulation, reconstruction, monitoring and analysis. Athena provide a skeleton framework in which users can embed his/her analysis code.

Athena is an enhanced concrete implementation of a general component-based architecture called Gaudi [35], developed for a wide range of experimental and computing applications. The development of Athena software was driven by some

[1] At the moment of writing the monitoring is not dealing with the RPC LVL1 trigger chain where signals from different coincidence matrix are arbitrated, combined in two views, and selected by the Pads, the Sector Logic and the MUCTPI (see section 3.4).

general principles such as: the use of abstract interfaces and dynamic libraries, a clear separation between data and algorithms (this allows, for example, the independence of complex algorithms of track reconstruction from most simpler client algorithms that use track objects), the need of manage data with different lifetimes and to assure separation between persistent and transient data. As usual in particle physics, the framework is oriented to run on input data in event per event steps and make use of python scripts (known as "job options") to initialize and configure run-time algorithms.

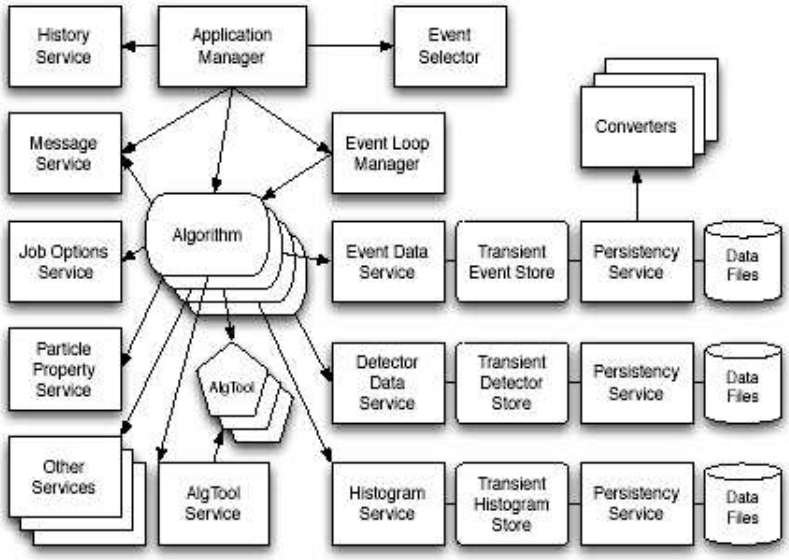

Figure 4.1: Major components and their relationships of the Athena framework.

Athena is a highly modular software and figure 4.1 shows a block diagram of its components. Major Athena components, as shown in figure 4.1, are:

Application Manager. The application manager is the component that manages and coordinates the activity of all other components. Through the *Event Loop Manager* performs the analysis on input data event by event.

Algorithms. Algorithms provide the basic per-event processing capability of the framework. Each Algorithm is designed to perform a specific well defined operation on some input data, even producing output data. In following sections of this thesis, algorithms written to perform the off-line RPC monitoring will be fully described.

Tools. As algorithms, tool can operate on input data and write output results, but they can be executed more than one time per event.

Services. Software components providing specific capabilities needed by algorithms.

Transient Data Stores. Data object used by algorithms are managed and organized by specific services depending on data type (event data, detector data, etc.)

Converters. Designed for the conversion of data from raw data to offline format and from transient to persistent (and vive versa) form. They allow algorithms code to be independent from the persistency mechanisms.

Selector. Selectors perform selection of events that will be processed.

ATLAS Software has a hierarchical structure: Athena is split in *Projects* and these ones are organized in *Packages*, a complete collections of projects is identified by an overall *release* number. Athena packages are managed in the CMT [2] configuration management environment and software code is developed by using SVN (Subversion) tool.

4.1.2 Data reconstruction process

As explained in section 2.2.6, the data read-out by the ATLAS detector (Front-End) are filtered by three levels of on-line triggers: level 1 (LVL1), level 2 (LVL2) and Event Filter (EF) [36]. The recorded events are stored into different streams depending on purpose (calibrations, physics or monitoring) and trigger hypotheses (muons, calorimetric clusters, minimum bias, and so on ...). The "express" stream is a special stream, contains a sample of each other trigger stream and it is analyzed first to provide a fast feedback of the detector status. A single run is split in *luminosity blocks* which have a fixed duration (five minuts) and are written in several files (of 2 GB size maximum).

Data recorded are in byte stream format (RAW data) and contain only hits of electronic read-out channels and information about trigger decisions. Those data are decoded and reconstructed by running Athena reconstruction process in various steps. First, data are translated from electronic channels to correspondent detector elements (i.e. read-out strips for RPC), then are reconstructed particles tracks, energy deposits in calorimeter cells, etc. Finally, are identified particles, secondary vertex, etc. Detailed output of the detector reconstruction from RAW data is written in ESD (Event Summary Data) files, AOD (Analysis Object Data) files, also produced in reconstruction process, contain a summary of the reconstructed event and sufficient information for common analyses. The data file size

[2] http://www.cmtsite.org/

per event changes from 1 MB per event for RAW files to 100 kB per event of AOD files (for ESD is 500 kB per event).

In parallel with each reconstruction process, off-line monitoring process are performed.

ATLAS uses a hierarchical analysis model. The reconstruction above described is run at the CERN computing farm (the Tier-0 centre) on the express stream (see pag. 44) as soon as data are available on disk and after on the different data streams.

Data quality is monitored online at the trigger level as well as offline during reconstruction. Monitoring histograms are checked by shifters and automatically via the Data Quality Monitoring Framework [37].

In the hierarchical ATLAS analysis model, the first step of reconstruction/monitoring process is done at the CERN computer farm called tier-0.

Detector calibrations, alignment, and basic detector operation have to be verified by rapidly reconstructing a smaller subset of the physics events (express stream). The first express reconstruction occurs as soon as data for a run are available and the necessary detector conditions information has been replicated to Tier-0, generally within few hours of the start of a run. Additional reconstruction iterations will occur as necessary until the calibrations are approved for full reconstruction. First pass of calibration and alignment should occurs within 24 hours after the data has been taken. The obtained constants are then used for the bulk processing of the data, once they have been validated by a second re-processing of the express stream.

Data are then distributed to the regional (called *Tier-1*) and local (called *Tier-2*) centres for data analysis. The Tier-1 centres are also responsible for data re-processing, i.e re-running reconstruction with improved calibration and alignment constants and with improved reconstruction algorithms.

Specialized calibration centers at Tier-2 facilities are also available in order to increase the statistics and the computer power available for calibration purposes. Specifically, Naples Tier-2 center is devoted to RPC calibrations. The RPC off-line monitor software here described is fully integrated with the Tier-2 calibration center infrastructure.

4.2 RPC off-line monitoring

Inside the general ATLAS off-line monitoring package, RPC monitoring tool has been developed. The RPC monitoring consists of four different algorithms specialized for different aspects of the RPC detector data object:

Electronic channels monitoring Monitoring the detector at the basic level of the read-out electronic channels (that means, for RPC, CMA channels, see sec.

3.4.1). It is run on RAW data in the first step of off-line reconstruction and it is focused to check possible problems in read-out hardware [3].

Detector element monitoring It is focused to monitor readout strips (offline identifiers).

RPC-MDT correlation monitoring It verify the correct time and spatial correlation between RPC η view strips and MDT tubes.

Track monitoring To explore the tracking capability of RPCs, a track tool that reconstructs muon tracks by using only RPC signals has been developed, those tracks (that in the following will be called *RPC standalone tracks*) are used to evaluate the performance (efficiency and noise) of RPC detector.

The output of the monitoring application are ROOT histograms, that are grouped in folder, one for each of the four algorithms. Further, histograms resultant of each algorithm are classified and grouped in different sub-folders according the different granularity on detector representations and the different application purposes. This classification is described below:

- **Commissioning plots**. These histograms are related to a single muon station or to a single trigger tower. They are named according to the hardware layout and used for commissioning. Because there are about 400 RPC chambers installed and by counting an average number of 100 histograms per chamber,the resulting number of plots is huge and than organized in sub-folder according to the station name and Sector Logic number.

  In order to reduce the number of histograms during the commissioning phase, where the RPC coverage was limited to a part of the apparatus, and during normal runs, when single data file have no more than several thousands of events, the booking is done only when the very first hit belonging to that plots appear in the event (*automatic plot booking*). To understand at glance the RPC coverage and simplify the data quality automatic checks, most of these histograms are booked exactly with the correct range (*automatic axis range*). A hole in these histograms corresponds to a hole in the detector coverage.

- **Sector plots.** The monitored quantities are plotted for an entire sector to allow a fast and comprehensive understanding of the detector response. The

[3] RPC Level 1 trigger decision quantities are not monitored but only quantities related to it, such as: 'Pivot' strips and thresholds causing a local coincidence in a single Coincidence Matrix which are readout similarly to raw hits.

histograms are organized in sub-folders, each one corresponding to a geometrical sector. Similarly to the previous ones, these histograms are booked automatically and have automatic axis ranges.

- **Overview plots.** These histograms are related to the global RPC status going into details and monitoring high level quantities for the RPC expert.

- **Shifter plots.** These histograms are intended to be controlled run by run by non expert shifters. These plots give a global and complete view of the RPC status without too many details.

- **Side A and C plots.** These histograms are used to generate RPC Side A and C data quality flags, which are stored into the so called Condition Database as required by the ATLAS experiment. These plots are grouped in sub-folders named `'RPCBA'` and `'RPCBC'`, where BA (BC) stands for Barrel side A (C), and produced by the packages RpcRawDataValAlg and RPCStandaloneTracksMon.

- **Readout strip panel summary plots.** These histograms are meant to characterize exhaustively the detector response in terms of readout panel average quantities such as efficiency, noise, cluster size, timing, occupancy and spatial residuals. These plots are produced by the package RPCStandaloneTracksMon, where track informations are available, and located in the sub-folder named `'Summary'`. For each geometrical sector and average quantity there is a summary histogram, where each bin corresponds to a readout panel, and a distribution plot filled with the summary plot bin contents.

- **Single strip summary plots.** These histograms are meant to characterize exhaustively the detector response with single readout strip granularity in term of the same quantities like the readout panels. These plots are produced by the package RPCStandaloneTracksMon where track informations are available and located in the sub-folder named `'CoolDB'`. For each geometrical sector, detection layer, and average quantity, there is a single strip summary histogram. Each bin of the histograms corresponds to a readout strip.

- **Efficiency and noise maps.** These histograms are meant to monitor the RPC gas volume response during the lifetime of the experiment in order to perform aging studies. These plots are produced by the package RPCStandaloneTracksMon, where track informations are available, and located in the sub-folder named `'RPCRadiography'`.

The four algorithms are highly configurable and driven by “python” scripting language file named “joboptions”. In these joboptions, the algorithms are called with several parameters (properties) that can be easily changed, if it is necessary, without to change (and re-compile) the C++ algorithm code. However, in the C++ code there is always the default value of each parameter that is over-written by the value in the joboptions file, if exist. Furthermore, the algorithms are meant to be modular (some analysis can be switch on/off by setting appropriate flags) and scalable (we can reduce the granularity of histograms to reduce memory consuming).

An important application of this feature is related to the RPC calibration. In fact, the creation and filling commissioning plots, single strip summary plots and Efficiency maps are turned off at Tier-0, due to the large computing memory consumption. Nevertheless, they are produced at the Naples Tier-2 calibration center with all other histograms. This allows to save maintenance, development and debugging time.

4.3 Detector and readout electronics monitoring

The readout and trigger electronics is implemented by on-detector programmable Coincidence Matrix ASICs (CMA)[38, 39] which are organized into independent trigger towers. A CMA trigger selection consists of a fast geometrical 25 ns temporal coincidence of 3 out of 4 RPC layers for ‘LowPt’ triggers and 1 out of 2 RPC layers for ‘HighPt’ triggers, in addition to a ‘LowPt’ trigger.

Input channels of each CMA are organized in 4 readout layers. The first two layers (I0 and I1 or ‘Pivot’ layers) have 32 channels each and the last two layers (J0 and J1 or ‘Confirm’ layers) have 64 channels each. The ‘LowPt’ CMA readout the ‘Pivot’ and ‘LowPt’ planes with the I0-I1 layers and J0-J1 layers, respectively. Instead, the ‘HighPt’ CMA readout the trigger pattern send-out by the ‘LowPt’ CMA with the I0 layer and readout the ‘HighPt’ plane with the J0-J1 layers, than without using the I1 ‘Pivot’ layer. The layers I0 and I1 are identified in the data with ‘ijk’ 1 and 2, and the layers J0 and J1 with ‘ijk’ 2-3 and 4-5. In fact, one ‘ijk’ number span 32 consecutive channels. In addition, ‘ijk’ 6 is used to identify the ‘Pivot’ channel belonging to the trigger hit pattern (trigger hits), i.e., when occurs a strip coincidence generatin a trigger signal, ijk=6 reports the index of the pivot strips from which starts the coincidence. In short, going out radially there are 6 RPC detection layers (named: ‘LowPt0’, ‘LowPt1’, ‘Pivot0’, ‘Pivot1’, ‘HighPt0’, and ‘HighPt1’) and 3 RPC trigger hits (named: ‘LowPt-Trigger’, ‘FromLowPtToHighPt-Trigger’,and ‘HighPt-Trigger’) measuring the bending and non-bending views.

A trigger tower is made by 2 phi and 2 eta views ‘LowPt’ CMA and the cor-

responding 2 phi and 2 eta views ‘HighPt’ CMA. The trigger towers (named also ‘Pads’) split the geometrical sectors of each side in two independent parts named Logical Sectors, corresponding to the strip readout panels ‘doublet phi’ 1 and 2. There are in total 64 Logical Sectors composed of 6 trigger towers (‘Small’ sectors) or 7 trigger towers (‘Large’ sectors) [4].

The RPC cable mapping is a not trivial task because the same electronics implements the trigger logic and the data readout. In fact, to avoid trigger inefficiency a large fraction of RPC strips are readout by two adjacent coincidence matrix in the ‘LowPt’ and ‘HighPt’ planes (named ‘cabling overlaps’). The pointing geometry requires cabling overlaps which are position dependent along the beam and when chamber boundaries are crossed in the bending view, a full non-bending view overlap is required between chambers (named ‘Logical-or’). More details on a trigger tower mapping are given in section 3.4.1 and in Figure 4.2 where three half station along z are shown, which are part of a Sector Logic and corresponding to one ‘doublet phi’.

[4]There are two exceptions: the ‘Small’ sectors 12 and 14 crossed by the ATLAS feet are readout by 3 trigger towers per Sector Logic and the ‘Large’ sector 13 is readout by 6 trigger towers per Sector Logic.

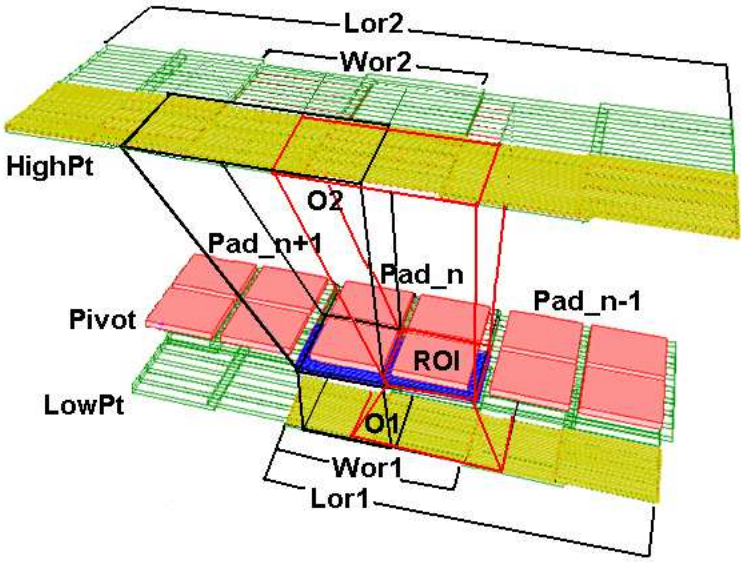

Figure 4.2: RPC trigger tower (Pad_n) implementing a projective muon trigger based on a geometrical coincidence between RPC raw hits from 'LowPt' plane, 'Pivot' plane and 'HighPt' plane. The trigger tower is segmented in four (ROI's) Region Of Interest's, there are exceptions where only one η CMA is used and the trigger tower have two ROI's. The trigger tower mapping overlap in 'LowPt' plane (O1) and 'HighPt' plane (O2) between adjacent ROI's inside a trigger tower and between trigger tower (only η overlap inside a trigger tower is shown). The trigger tower makes a 'Logical-or' in ϕ view with the station nearest to the IP on 'LowPt' plane (Lor1) and with the farthest one or both ones on 'HighPt' plane (Lor2). The picture shows the "wired-or" (Wor) in ϕ view of the central station.

The RPC readout electronics granularity is translated into the following five integer parameters:

- sector logic: from 0 to 63.
- pad: from 0 to 6.
- coincidence matrix: from 0 to 7.
- ijk layer: from 0 to 6.
- electronic channel: from 0 to 31.

An electronic channel is translated into one or more readout strips by the RPC cabling service.

As already explained in section 3, the RPC detector is build from single RPC units. The RPC planes are made of one or two mechanically independent RPC

units along the longitudinal direction (z or η) and identified as 'doublet z' 1, 2 and 3, [5], counting from the IP. The station number is positive in side A and negative in side C, increasing along the z direction.

A 'Middle' RPC station is built by two RPC planes ('LowPt' and 'Pivot' planes) and an 'Outer' RPC station by one RPC plane ('HighPt' plane). The RPC planes inside a station are identified as 'doublet r' 1 and 2, counting from the IP. Most RPC stations are integrated with MDT stations.

The RPC strip panel granularity is translated into the following nine integer parameters:

- station phi: from 1 to 8 (numbers increase in the direction of increasing ϕ).
- station name: 2 (BMS), 3 (BOS), 4 (BML), 5 (BOL), 8 (BMF), 9 (BOF) and 10 (BOG).
- eta: from -7 to 7 (increases in the direction of increasing z).
- doublet r: from 1 to 2 (increases from IP).
- doublet z: from 1 to 3 (increases from IP).
- doublet phi: from 1 to 2 (increases as phi).
- gasgap: from 1 to 2 (increases from IP).
- measure view: 0 for Eta measuring view and 1 for Phi measuring view.
- strip: from 1 to a maximum value of 80.

4.3.1 Readout electronics plots

The readout electronic channels monitoring algorithm analyses not decoded RAW data in the same format in which are written on disk from DAQ system. Histrograms produced are segmented on coincidence matrix and channels.

Coincidence Matrix plots

The electronic channel profiles, timing and trigger road are organized in 63 sector logic groups. The plots of Figure 4.3 and 4.4 represent few example. In Figure 4.3(a) the profile histograms show the channel count of a RPC layer of two adjacent coincidence matrix for all the pads of the corresponding sector logic. As a

[5] There are 48 special RPC doublets positioned on 24 coil ribs which are readout by the adjacent station nearest to the IP and three quarter of them are identified as 'doublet z' 3 and one quarter as 'doublet z' 2.

general rule the pivot channel ijk=0 or 1 are plotted separately (32 channels) but the confirm channel ijk=2-3 or 4-5 are plotted together (64 channels) because this correspond how they are connected along the readout strip panels.

Channel correlation plot between the trigger channel (ijk=6) and any confirm channel are also produced (see Figure 4.3(b)) separately for each coincidence matrix. Timing plot and correlation plots are put together in the same folder, because it is when both spatial and time coincidence between different layers are verified that the trigger fires.

The electronic channel time is displayed by histograms like in Figure 4.4(a) and 4.4(b), where the electronic channel absolute time and the time relative to the average trigger time in LowPt phi view.

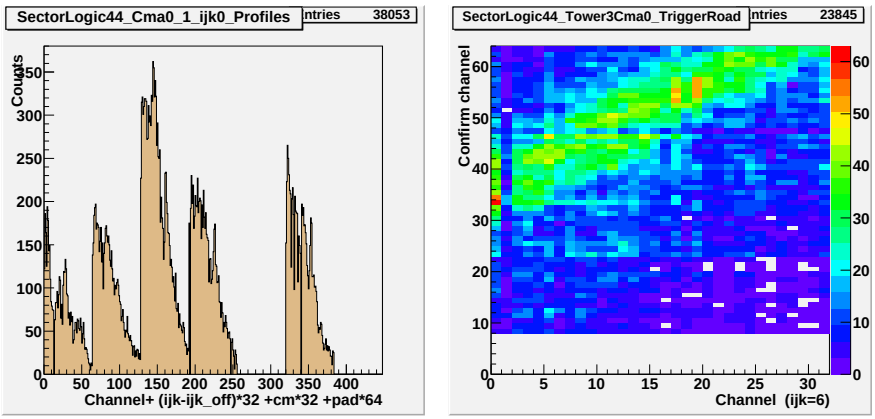

(a) One layer readout channel profiles of two adjacent phi view CM's.

(b) Scatter plot between confirm channel number and trigger channel number of the same CM.

Figure 4.3: Examples of RPC readout channels commissioning plots. Data are from calibration stream.

Readout overview plots

Overview plots relates to the ATLAS RPC trigger-readout quantities (see plots of Figure 4.5).
The plot of Figure 4.5(a) shows the distribution of the number of fired electronic readout channel per event. The mean value of the distribution is large because a cosmic muon cross generally more than RPC sector and the number of RPC channels fired is multiplied by overlaps between coincidence matrix and by "logical-OR" connection of ϕ strips.

In order to evaluate how the fired readout channel are distributed into readout hardware objects the 1D plot of Figure 4.5(b) and the 2D plots of Figure 4.5(c)

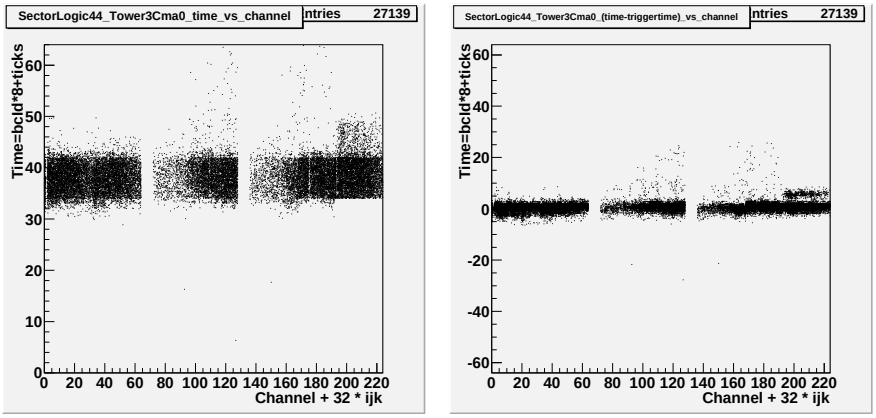

(a) Time vs readout channel of a CM.

(b) Relative time w.r.t average RPC trigger time vs readout channel of a CM.

Figure 4.4: Examples of RPC readout channels commissioning plots in 'RPCLV1/Profiles/SectorLogic44' folder: and 'RPCLV1/TriggerRoad/SectorLogic44' folders. Data are from calibration stream.

and 4.5(d) count the total number of fired channel per Sector Logic, Pad and Coincidence Matrix. The two bi-dimensional histograms have on the X axis the sector logic and on the Y axis, respectively, the Pad number (from 0 to 7) and the Coincidence Matrix number shifted by eight times the Pad number.

The plots of Figure 4.5(e) shows the distribution of the number of trigger hits per event separated for the two views. The are four of such a plots. Two plots, one shown in Figure 4.5(f), display the correlation between trigger hits in Eta and Phi view. Plots showing the correlation between Eta and Phi Coincidence Matrix trigger hits are also produced. These plots identify an area called Region of Interest (RoI).

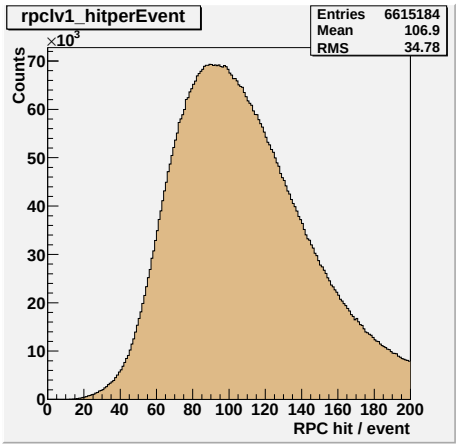

(a) Distribution of the number or fired readout channels per event.

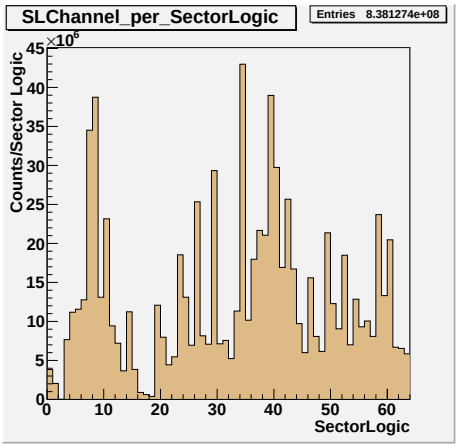

(b) Sector logic hit profile plots.

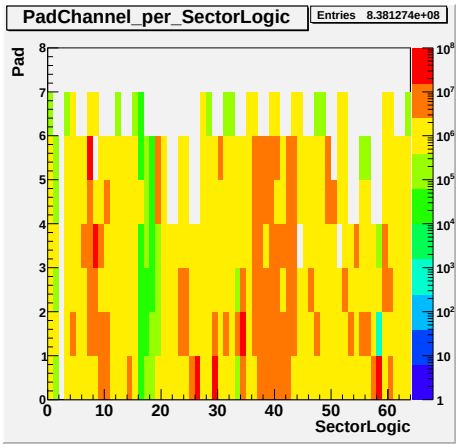

(c) Hit map of trigger tower vs sector logic.

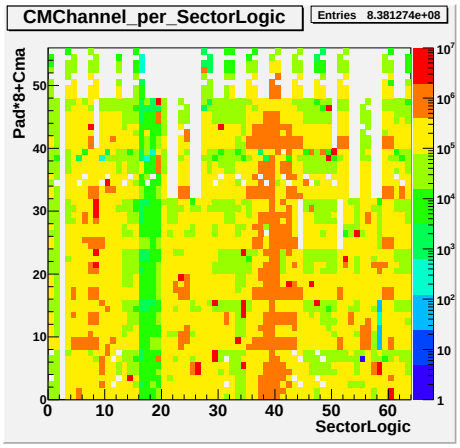

(d) Hit map of CM vs sector logic.

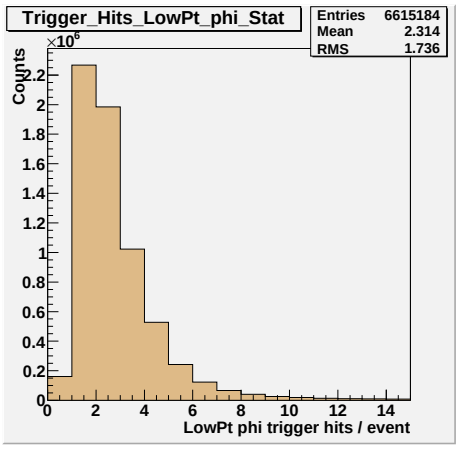

(e) Distribution of LowPt trigger hits in phi view.

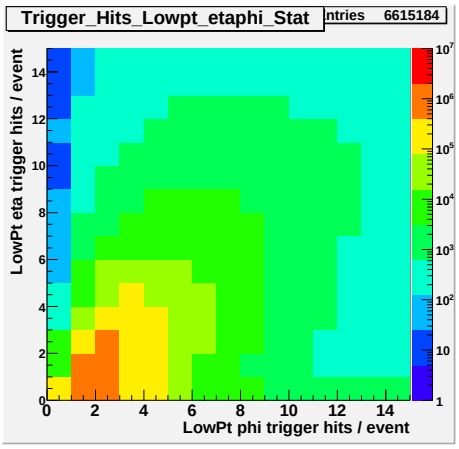

(f) Correlation between number of η and ϕ trigger hits in LowPt stations.

Figure 4.5: Examples of RPC readout channels overview plots in 'RPCLV1/Overview' folder. Data are from physics-RPCwBeam stream.

Four plots (figure 4.6(a)) shows the pattern of the coincidence matrix layers: J0, J1, I0 and I1 associated to a trigger hit for the same Coincidence matrix. The majority logic is programmed into the CMA, therefore not all combinations are allowed.

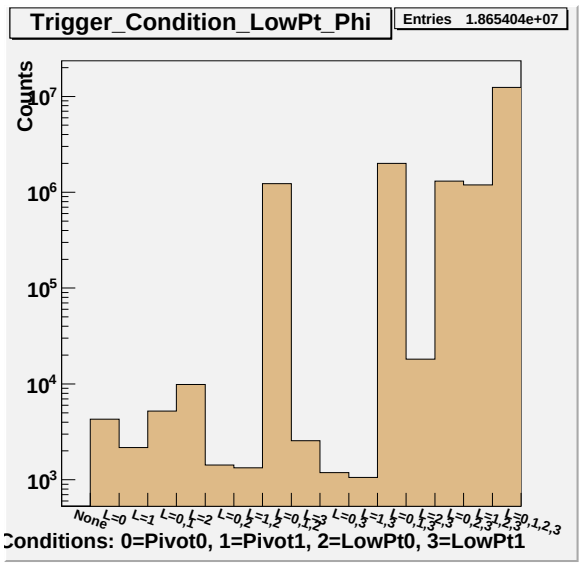

(a) Distribution of LowPt trigger pattern in ϕ view.

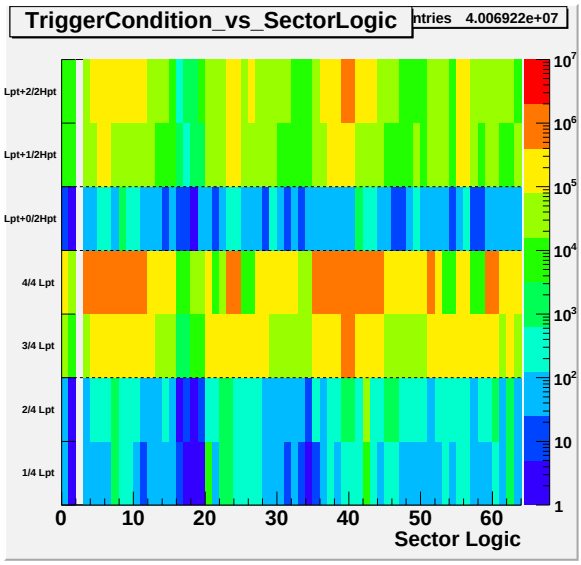

(b) Counts of trigger layers pattern vs sector logic.

Figure 4.6: Distributions of detector layers patterns generating LowPt ϕ trigger signals in coincidence matrix.

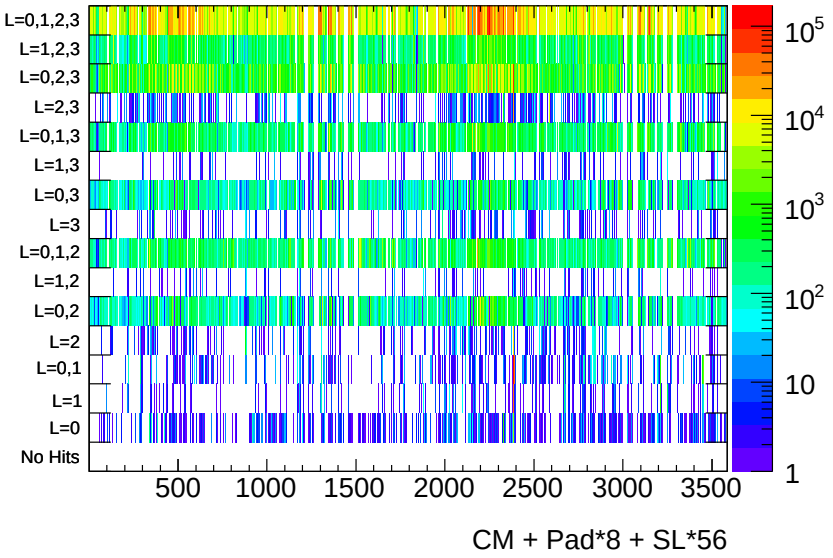

Figure 4.7: Distribution of trigger conditions for each single ATLAS RPC Coincidence Matrix (CM).

The 2D plot of Figure 4.6(b) is similar to the previous ones. It shows for each Sector Logic which detector layer patterns generate the trigger in phi view. The plot is divided in two parts along the Y axis, the lower part is related to the LowPt trigger coincidence and the upper part to the HighPt trigger coincidence. LowPt and HighPt triggers are realized with four and two independent RPC active layers respectively. In standard configuration LowPt trigger logic consists of 3 out of 4 layers in the same trigger time window (25 nsec maximum) and HighPt trigger logic of 1 out of 2 layers, in addition to a LowPt trigger. Consequently, not allowed layers pattern giving trigger (such as 2 out of 4 layers in LowPt trigger) is evidence of some inefficiency in the readout or fake triggers. The are also 2D plot similar to the previous one but the trigger condition is monitored for each single Coincidence Matrix (figure 4.7). On the X axis is listed the coincidence matrix number shifted by eight times the pad number and 56 times the sector logic number and on the Y axis is listed all possible layer combinations that could or could not provide a trigger hits.

4.3.2 Detector plots

A further step in the RPC monitoring is the check of the quantities related to physical detector elements (strips, panels, gas volume, etc.) instead of the electronic readout channels. Clearly, this monitoring algorithm is run on data decoded

by using map relating the electronic channels with the detector elements. In the following, the histograms produced are classified by categories shown in sec. 4.2.

Chamber plots

Figures 4.8 and 4.9 show the most relevant histograms with 1 strip granularity (with the exception of the plot d)) and related to a single station, layer and view (with the exception of the η-ϕ correlation plot). To reduce the total number of histograms, the eta view panels of different doubletz and phi view panel of different doublet phi are plotted on the same histograms with increasing number of strips. Due to the large number of RPC chamber types the total number of strips in both views are in general different.

Together with RPC hits it is important to monitor the RPC clusters, which are defined as a group of adjacent strips inside a window time coincidence and directly related to a charged track crossing the active volume. The plot of Figure 4.8(a) shows the strip profile but a similar plot exist for the baricenter of RPC clusters. An example of scatter plots between the hit arrival time and strip is given in Figure 4.8(b). From these plots is possible to extract time distribution to monitor the

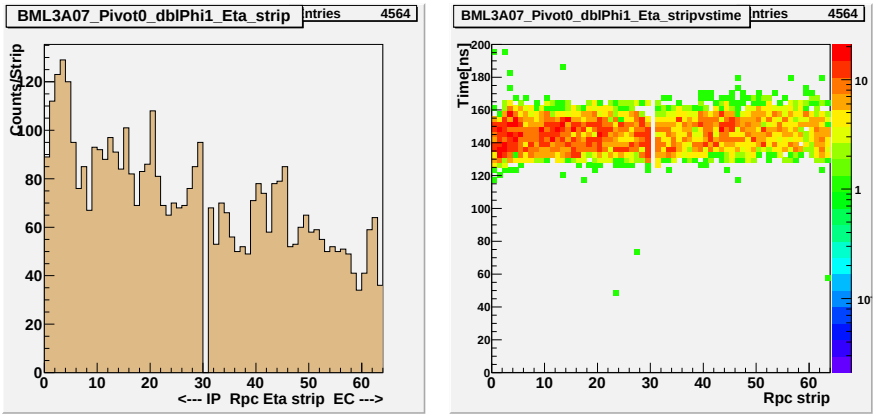

(a) RPC strip profile. (b) RPC time vs strip.

Figure 4.8: Example of RPC single station commissioning plots in 'RPC/Chambers/BML3A07' folder.

RPC time alignment and spread. In Figure 4.9(a) is reported a two dimensional plot displaying the hit multiplicity of the cluster to which the strip belong to and in Figure 4.9(b) the distribution of the cluster multiplicity for one readout panel.

Correlation plots between the two view of the same gas volume are important because they give localized information and can remove phi 'wired-or' and 'logical-or' ambiguities in phi view by using the orthogonal eta view. An example

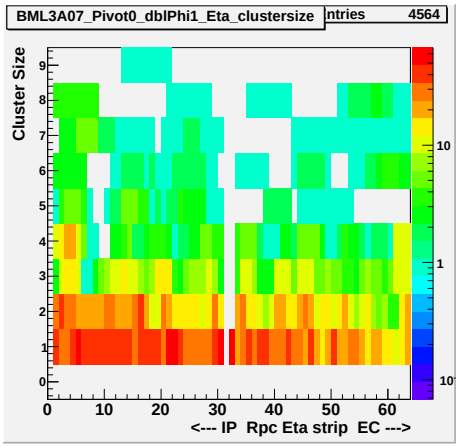

(a) RPC cluster size vs strip.

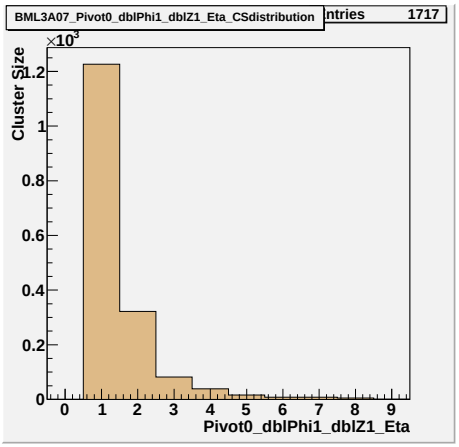

(b) RPC cluster size distribution for one readout panel.

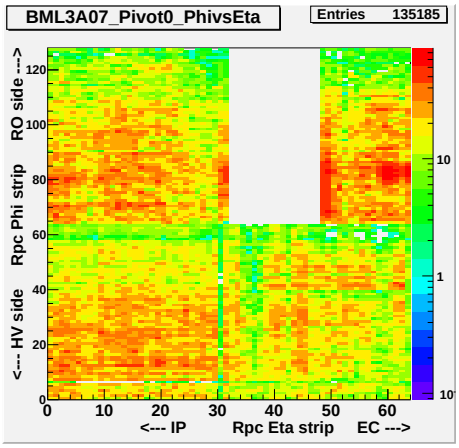

(c) RPC phi view strip vs eta view strip for the same gas volume.

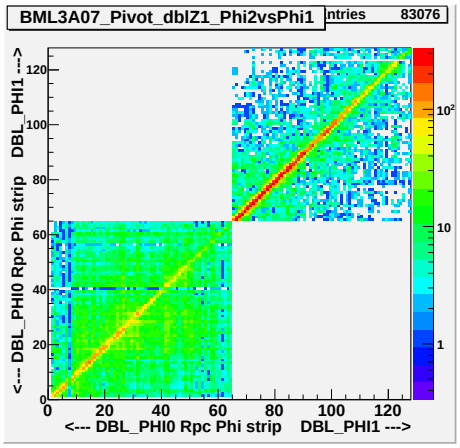

(d) Same view RPC strip correlation between adjacent layers.

Figure 4.9: Example of RPC single station commissioning plots in 'RPC/Chambers/BML3A07' folder.

is given in the plot of Figure 4.9(c) where at a glance is possible to see the RPC coverage. Phi-Phi or Eta-Eta strip spatial correlation between gas volumes doublets belonging to adjacent layer (same plane). For trigger hits the correlation is done with respect to the innermost pivot layer. An example is given in the plot of Figure 4.9(d). These plots are meant to debug the RPC hardware mapping during the commissioning phase or after hardware intervention on the RPC chambers.

Sector and ATLAS plots

A similar set of plots is also produced grouping together chambers of the same sectors to still have a detailed view but more focused on global behaviour. Example of sector plots are given in The `'RPC/Sectors'` folder contains plots showing the η and ϕ view spatial correlation of RPC hits and clusters belonging to the same gas volume (see Figure 4.10a).
One histogram shows one RPC layer of a geometrical sector with all stations along Z and both doubletPhi. For trigger layers the plots correspond to trigger coincidence in Eta and Phi views in the readout strips.

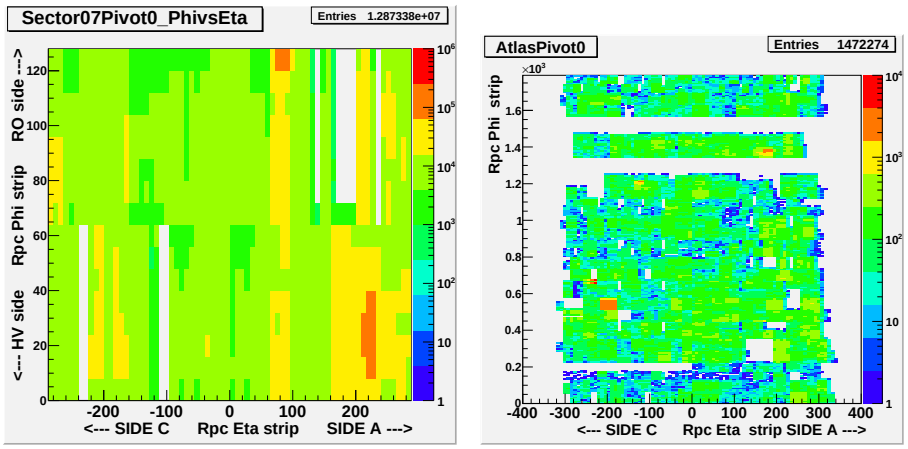

(a) One sector RPC hits map in phi view-eta view plane for one layer.

(b) RPC hits map in phi view-eta view plane for one layer.

Figure 4.10: Examples of RPC sector (a) and RPC atlas (b) plots.

RPC overview plots

Overview plots monitor integrated quantities for the entire ATLAS detector (see Figure 4.11).
The plots Figure 4.11(a) and 4.11(b) shows the distribution of the number of RPC hits and the number of RPC η and ϕ clusters per event, and the plot of Figure 4.11(c) shows the time distribution of all RPC hits for one view. No clean-up cuts are used to fill the timing plots which have a range of 200 nsec (equal to readout window of RPC level-1 trigger system) with a total number of 64 bins (bin size equal to 3.125 nsec to the RPC internal clock). The plots of Figure 4.11(d) shows the cluster size distribution of readout strips for one view.

Several two dimensional histograms map the RPC detector status in a convenient way. Two example of these histograms are given in Figure 4.12(a) and

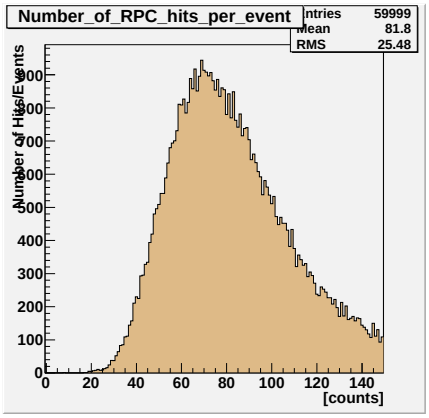

(a) Distribution of RPC hits per event.

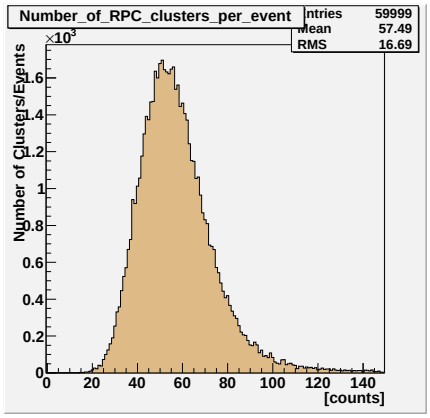

(b) Distribution of RPC clusters per event.

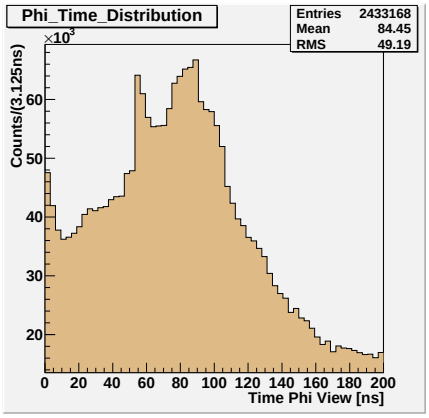

(c) Time distribution of RPC hits in phi view.

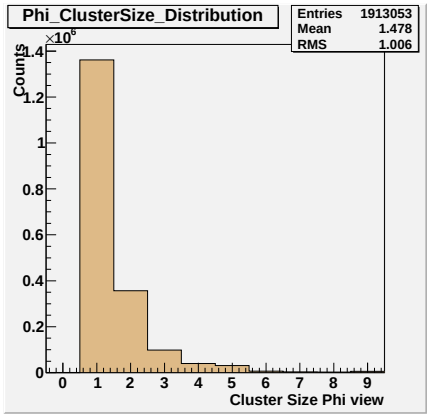

(d) Cluster size distribution of RPC hit clusters in phi view.

Figure 4.11: Examples of RPC overview plots in 'RPC/Overview' folder. Data are from physics-RPCwBeam stream.

4.12(b). The first one shows the RPC trigger hits map. The same kind of map exists for RPC hits for each detector layer. The RPC map have Eta station number along the X axis and the sector number un-folded in three planes along Y (see dashed lines).
The second one shows the map of correlated Phi and Eta hits of the entire ATLAS RPC detector for the corresponding layer.
Each bin in both axis corresponds to two crossing orthogonal strips of the same gas volume and is filled if both strips are found in the event. One histogram shows all 16 RPC geometrical sectors of one layer un-folded in Phi view. The range along the Y axis (Phi view) is equal to the number of phi strip for that layer. The

positive (negative) range and along the X axis (Eta view) is equal to the maximum number of eta strip for that layer and side A (C) Eta strips of side A (C) are plotted positive (negative). There are also histograms similar to the previous ones, but with spatial coordinates Phi and Z in mm are used instead of strip number.

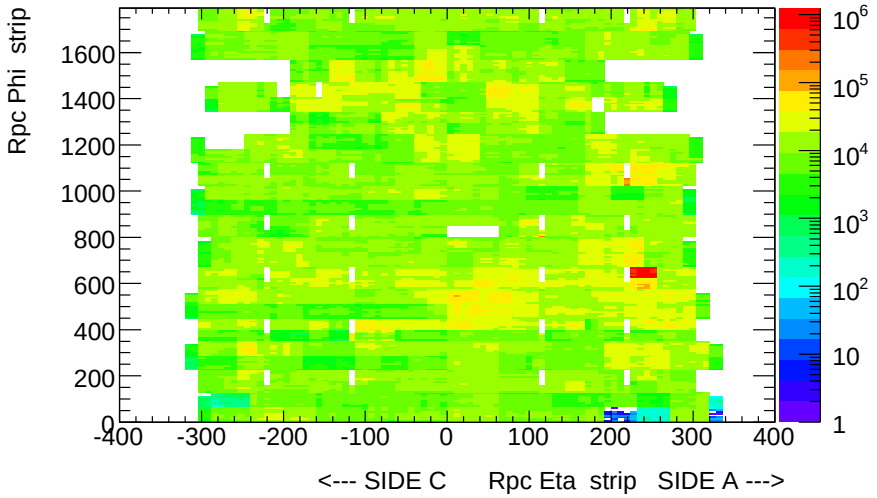

(a) Low Pt trigger hits map.

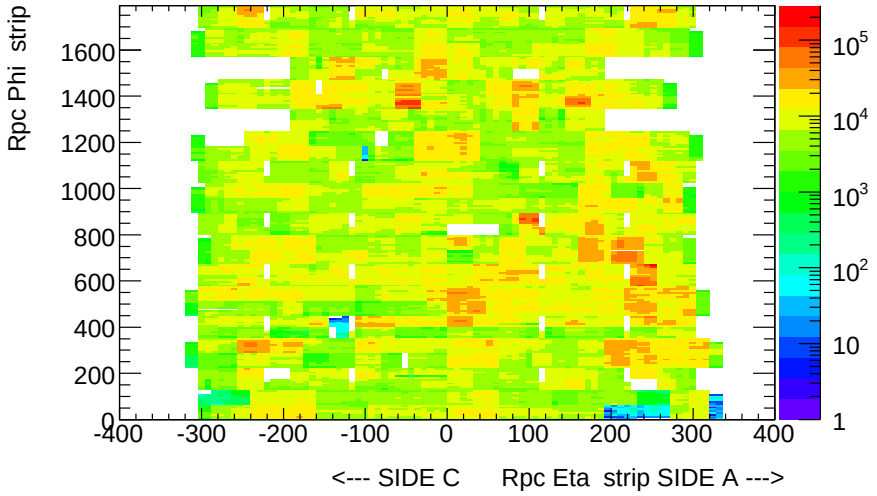

(b) Pivot 0 plane hits map.

Figure 4.12: .

Trigger data

Histograms intended to monitor the setting and the response of the trigger to the programmed spatial coincidence are also produced by RPC off-line monitoring. The width of the spatial geometrical coincidence (named 'trigger road') can be programmed to correspond up to 3+3 high transverse momentum track values.

Figure 4.13(a) shows the distribution of the conventional number named 'Threshold' which labels the trigger configuration for one view. Other six histograms shows the scatter plot between the 'Threshold' and the 2D impact parameter of the trigger segment defined by trigger hits and the confirm hits. Figure 4.13(b) clearly shows a projective trigger road in non-bending view as extracted from cosmics data. At the time of this writing the trigger road histogram granularity is only limited to small and large sectors, in addition to Low-HighPt and Phi-Eta view.

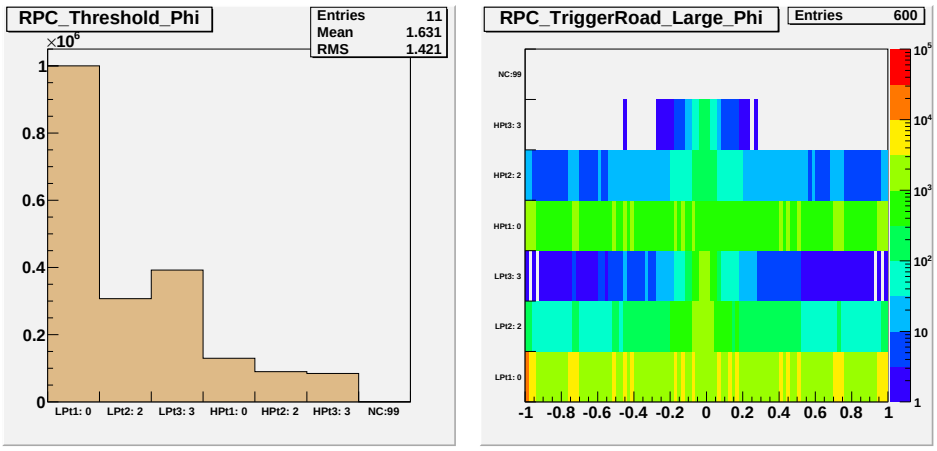

(a) Distribution of RPC trigger hit threshold in phi view.

(b) RPC trigger segment impact parameter in the corresponding view.

Figure 4.13: Examples of RPC trigger road plots in 'RPC/TriggerRoad'. Data are from physics-MuonswBeam stream and run 148209 (1,850,000 events analysed).

Luminosity blocks

The ATLAS data is divided in luminosity blocks ('LumiBlocks'), which should correspond to the minimum time interval where the instantaneous luminosity should be evaluated. In order to monitor the instantaneous luminosity by the RPC detector a chain of histograms storing information for each group of contiguous events were implemented.

For every luminosity block XXX these specific histograms are booked and filled by the monitoring algorithm and tagged as ‘luminosity block histograms’. Because the off-line monitoring at Tier-0 is split in data-files and sub-jobs, usually a data-file don’t correspond to a luminosity block. The luminosity block histogram merging is done at Tier-0 with an appropriate tool called (`‘mergeLBintervals’`).

The RPC luminosity block histograms are filled with the corresponding trigger hits. These plots are intended to monitor the RPC trigger rate from the readout hits with time granularity equal to the run luminosity block.

4.4 RPC and MDT correlation monitoring

The `‘MdtVsRpcRawDataValAlg’` package was developed to check spatial correlation and time synchronization between raw hits provided by MDT and RPC detectors. This was done by comparing the longitudinal position of MDT tube hits and RPC Eta strip hits belonging to the same station and plane. In order to suppress a residual MDT noise a cut on the MDT ADC of about 50 counts is always implied

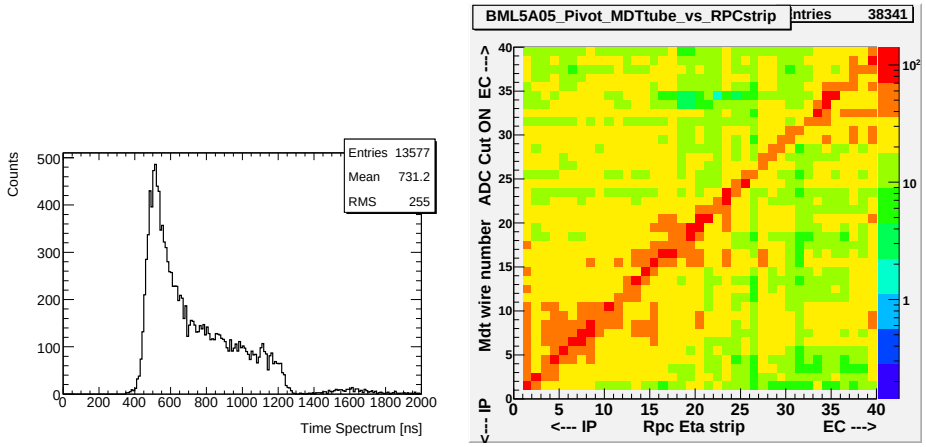

(a) MDT TDC spectra for tracks crossing HV or RO side.

(b) MDT tube vs RPC eta strip of one plane inside a station.

Figure 4.14: Examples of single station commissioning plots correlating RPC and MDT. from ‘MDTvsRPC/Chambers/BML5A05’ folder. The noise cut on MDT ADC of 50 counts is implied. The data are from physics-RPCwBeam stream.

The correlations is done between RPC strip number and MDT tube layer number. Because a MDT tube is long as the entire (in ϕ direction) chamber width and it is coupled to two RPC panels, the RPC doublet readout strip panel index allows to establish the side of the tube when the hit was generated by the crossing track.

This is important in order to monitor asymmetry in MDT detector response along the tube. Figure 4.14(a) shows a histograms displaying the MDT TDC spectra in nsec of MDT tube hits correlated to the corresponding RPC doublet.

Two dimensional plots showing the z hits correlation of one plane between RPC and MDT for the entire sector (see Figure 4.14(b) are important in order to verify the muon system synchronization with a limited number of histograms. On the X axis the RPC Eta strip Z coordinate in mm is plotted, whereas on the Y axis the MDT tube center Z coordinate in mm is plotted. The axis ranges are generated automatically according to the minimum and maximum Z coordinate of RPC and MDT tube for the plane and sector.

4.5 RPC track monitoring

Because RPCs can measure either η and ϕ coordinates of crossing muons, a tracking algorithm that use only RPC data has been implemented in off-line monitoring [40]. It is capable of producing a fast feedback on RPC detector data quality, without using informations from MDT precision chambers and without relying on the full ATLAS event reconstruction and combined quantities.

The RPC tracking is based on RPC space points, which are defined by orthogonal RPC baricenters of cluster of the same gas volume. The pattern recognition is seeded by a straight line, which is defined by two RPC space points belonging, respectively, to low-Pt and pivot planes of the same or nearby station. RPC space points not part of any previous tracks and inside a predefined distance (50 mm) from the straight line are associated to the pattern. Resulting patterns with points in at least 3 out of 4 layers in low-pt and pivot planes are retained and a least square linear fit is performed in two orthogonal views.

The patter recognition parameters can be selected by joboptions. The ‘MergePointDistance’, with a default value of 50 mm, establishes when a space point can be merged in a seeded RPC track. The ‘EtaStationSpan’, with a default value of 2, and the ‘DoublePhiSpan’, with a default value of 1, establish the range of stations along z and sectors along phi that a track can cross in order to avoid pathological tracks. With the default values a cosmic track crossing the detector top to bottom results in two RPC tracks.

From data triggered with cosmics about 95 % percent of events have at least one RPC track; this is due to the strong correlation between the pattern recognition and the trigger algorithm. Applying a quality cut of chi2/dof < 1 about 70 % of events have at least a good tracks and 10 % with more than one. This quality track cut can be set by joboption changing the parameter ‘Chi2dofCut’.

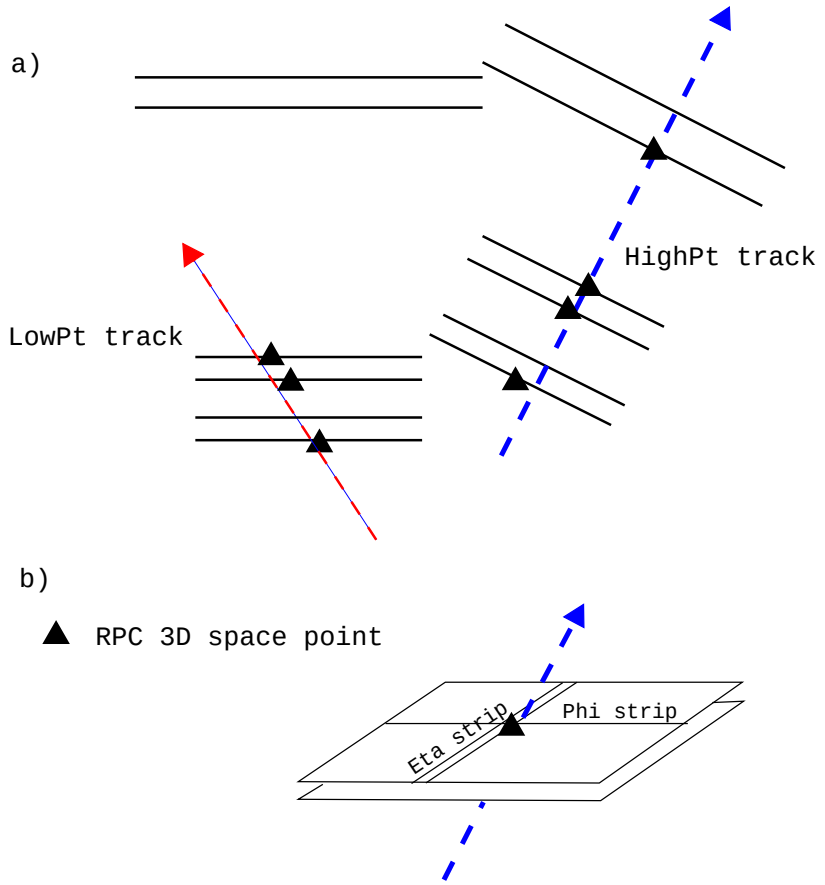

Figure 4.15: Schematic view of the RPC standalone tracking algorithm. Starting from eta and phi clusters (with size less than 4), RPC 3-D space points are build (b). From these points, a pattern recognition with linear fit is performed requiring at least 3 hits over 4 RPC layers in Low Pt stations and at least 1 hits over 2 layers in Highpt stations (a).

Detection efficiency

The detection efficiency is measured by repeating 6 times the RPC tracking. At each iteration the layer under test is removed from the pattern recognition and track fitting. The track reconstructed is then extrapolated to the active gas volume of the removed layer and the crossing point evaluated. No error analysis on the extrapolation accuracy is done at the moment of writing. The efficiency is evaluated only if the crossing point is inside a fiducial region expressed in term of strip distance from active volume boundaries. The fiducial border size can be set by the joboptions parameter ‘nstripfiducial’ which by default is zero. If the extrapolation point is inside the fiducial region then the gas volume is assumed to be efficient if at least one hit is found inside a search window expressed in terms of strips by the

joboption parameter ‘nstripfiduceff’, which have a default parameter of 3 strips.

An unbiased measurement of the RPC efficiency is also made if the detector is part of the trigger decision. In fact, the 3 out of 4 majority trigger logic makes the layer under test response irrelevant in the trigger decision when the other three layers have a good track.

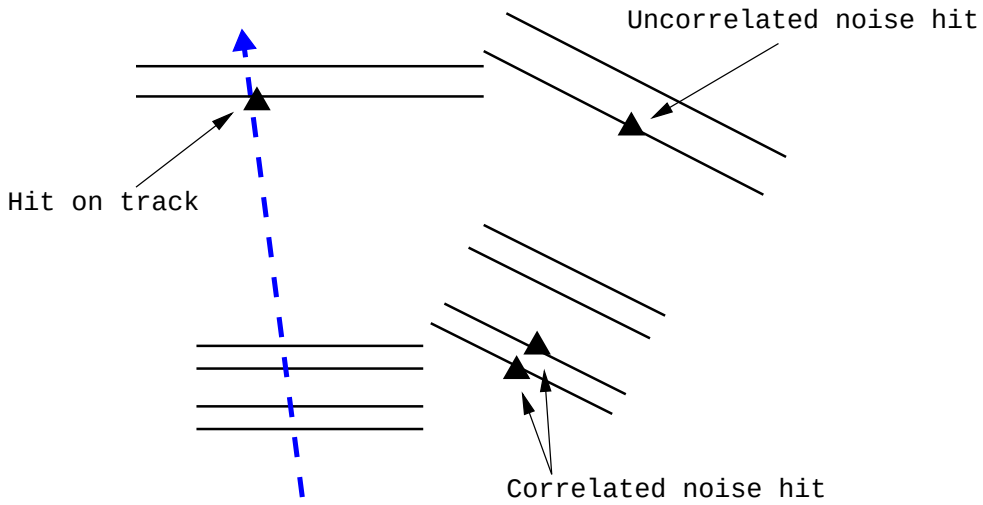

Figure 4.16: Definition of *on tracks* hits, *correlated* and *uncorrelated* noise hits. Hits not associated to any track are classified as “noise” of RPC chambers: hits belonging to two different gas gap of the same RPC doublets are defined “correlated noise”, whereas hits present in only one gas volume are define “uncorrelated noise”.

Noise Measurements

The detector total noise is measured taking into account RPC hits not belonging to any RPC track, that is, farther away than the parameter ‘MergePointDistance’. The correlated noise is defined by RPC noise hits belonging to the same chamber but different gas volume and inside a spatial window defined by the parameter “`mergePointDistance`”. The parameters occurring in the noise definition are kept equal to the track pattern recognition parameters to stay conservative. This could change if further needs emerge.

The noise is expressed in term of Hertz per centimeter square by the formula:

$$Noise = \frac{Counts}{Events \cdot w \cdot surface},$$

where w is the rpc readout time window and is equal to 0.2 μsec, the maximum value allowed by the hardware and used for cosmics.

Cosmics run versus collisions run

Cosmic rays arrive randomly in time and not uniformly on detector surface. This makes detector studies with cosmics less accurate then with beam collisions. Tracks produced by beam collisions are synchronous with beam clock, pointing to the interaction point, and uniform in azimuthal angle and pseudo-rapidity. The difficultly with beam is due to the presence of the magnetic field and operation at high luminosity. The above described pattern recognition and the track quality cut correspond, in magnetic field, to a cut in transverse momentum. At high luminosity a large uncorrelated and correlated background could increase the number of fake tracks significantly. Studies with a Monte Carlo sample with pile-up and cavern background are underway at the time of this writing.

Commissioning histograms are related to single chamber and have 1 strip granularity. The plot of figure 4.17(a) shows the profile of strip crossed by the tracks reconstructed with the other layers. Similar histograms are filled with the profile of strips crossed by the tracks, reconstructed with the other layers, with a nearby fired strip in the same view (figure 4.17(b)) and in both views (figure 4.17(c), respectively. The three previous histograms allow to compute the readout panel detection efficiency not conditionated or conditionated to the other measuring view. The histogram of Figure 4.17(d) show the distribution of the spatial residual defined as the difference between the projected track local coordinate and the RPC cluster local coordinate. The track extrapolation errors are not subtracted from the residual evaluation.

RPC tracks overview plots

The general plots show quantities related to RPC track standalone capability for the entire ATLAS detector. In this section only some of the overview plots are described (see Figure 4.18) and the other general plots are discussed in Section 5.2.1 where shifter plots are described.

The quality of the RPC tracks reconstructed with all layers are monitored by the distribution of the chi2 per degrees of freedom, the 3D RPC space points multiplicity and spatial and time residual. The histogram of Figure 4.18(a) display the distribution of the total chi2 per degree of freedom (both views) and the histogram of Figure 4.18(b) shows the scatter plot between the chi2 per degree of freedom of the two views separately. The distribution of the number of 3D RPC space points associated to the track and used by the straight line fit is plotted on the histogram of Figure 4.18(e). In addition, the RPC tracks are classified according to the 3D RPC points layer combination and the distribution is shown by the histogram titled of Figure 4.18(f). Spatial track residual distribution and the time spread of the 3D RPC space point are also reported in Figure 4.18(c) and 4.18(d).

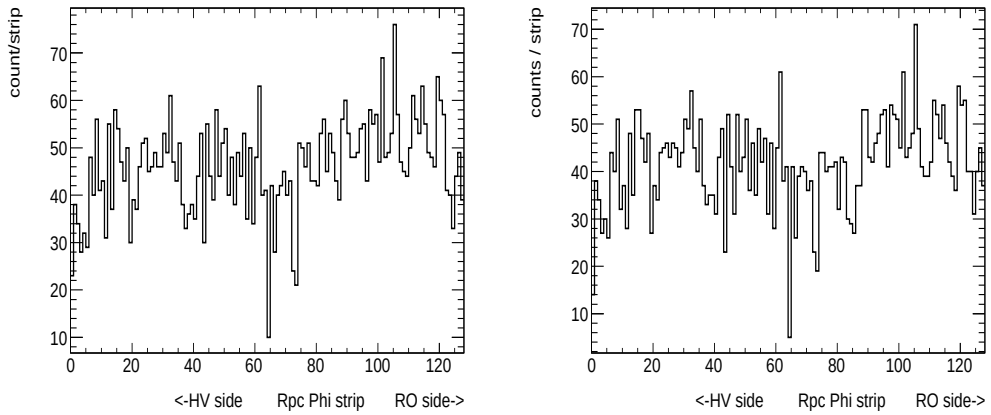

(a) Strip profile of RPC tracks projected on the removed readout panel.

(b) Strip profile of RPC tracks projected on the removed readout panel and matching RPC cluster hits.

(c) Strip profile of RPC tracks projected on the removed readout panel and matching RPC cluster hits in both views.

(d) Spatial residual distribution of a strip readout panel.

Figure 4.17: Examples of RPC single station commissioning plots.

In order to visualize directly the origin of the tracks (cosmic, random, single beam, beam collisions, ...) and the trigger stream (RPC, TGC, Lucid, MTBS, ...) the reconstructed tracks are extrapolated on different planes such as (x,z) plane at y = 81 m, corresponding to the ATLAS surface (see Figure 5.6(f)). In addition, two-dimensional track parameters distribution in term of track pseudo-rapidity variable $\eta = -ln(tan(\theta/2)$, with θ the track poloidal angle, track impact parameter b and the track azimuthal angle ϕ are also produced (Figures 4.19(a) and 4.19(b)). Finally, one dimensional track parameters distribution are shown for all above quantities (see Figures 4.19(c), 4.19(d) and 4.19(e)).

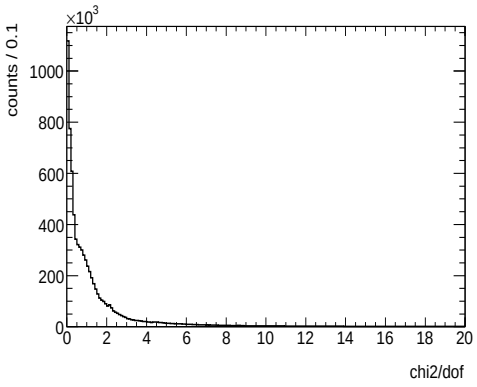

(a) χ^2 per dof distribution of RPC track fit.

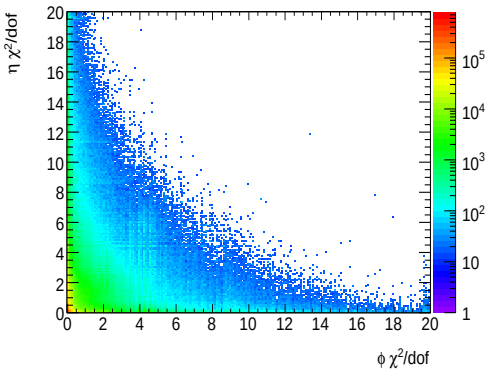

(b) Scatter plot of χ^2 per dof RPC track fit between the two views.

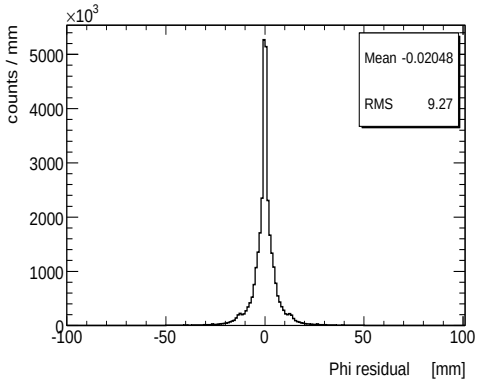

(c) RPC spatial residual in phi view.

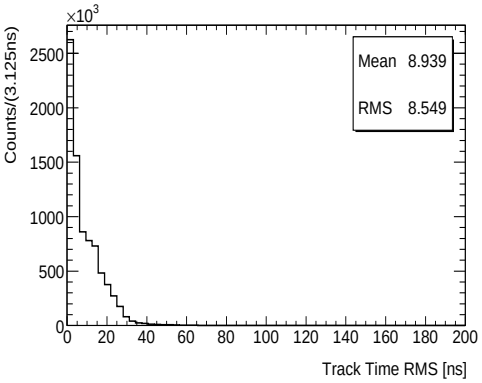

(d) Standard deviation of RPC hit time belonging to a RPC track.

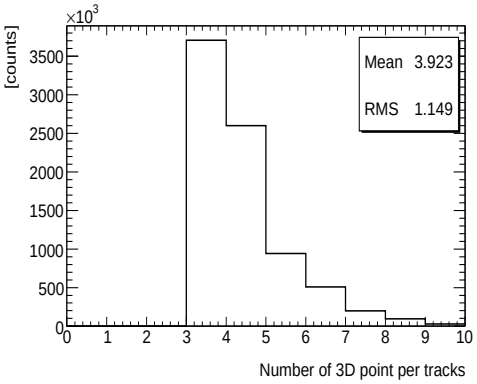

(e) Distribution of RPC 3D point number per RPC track.

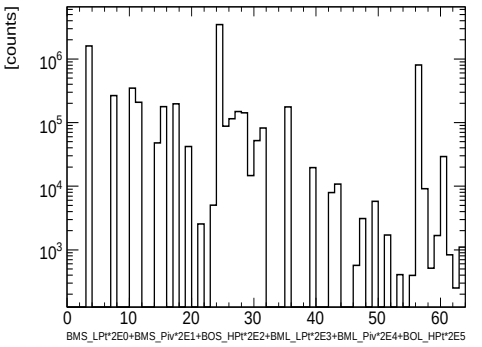

(f) RPC track 'type' plot.

Figure 4.18: Examples of RPC track overview plots in 'RPCStandAloneTrackMon/Overview' folder.

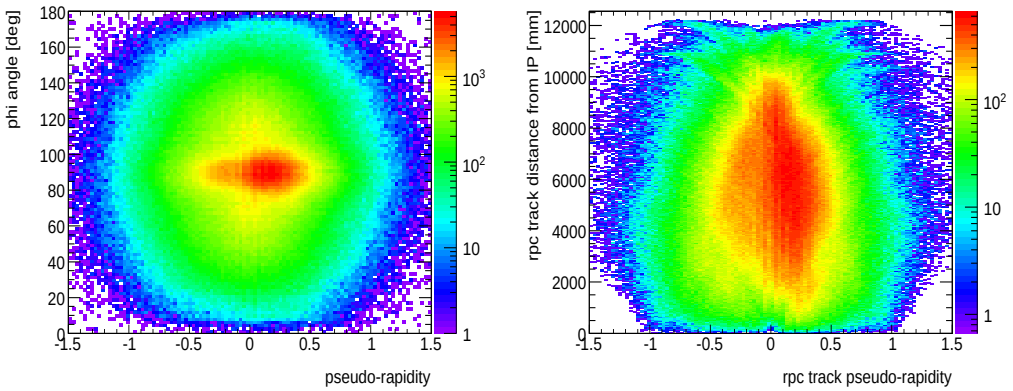

(a) Scatter plot of pseudo-rapidity η vs azimutal angle ϕ of reconstructed tracks.

(b) Scatter plot of impact parameter b vs azimutal angle ϕ of reconstructed tracks.

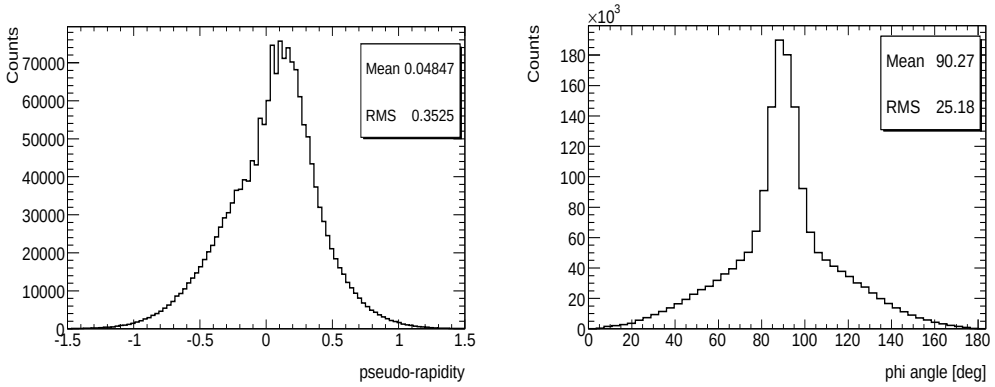

(c) Distribution of pseudo-rapidity η parameter of reconstructed tracks.

(d) Distribution of azimutal angle ϕ parameter of reconstructed tracks.

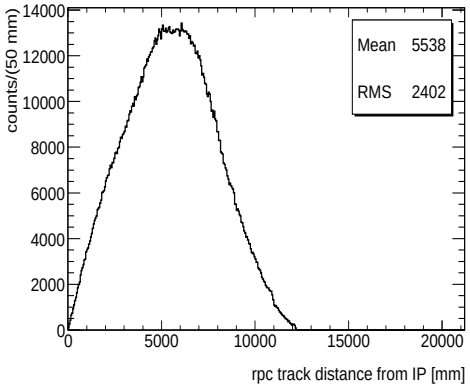

(e) Distribution of impact parameter b of reconstructed tracks.

Figure 4.19: Examples of track parameters scatter and distribution plots.

5
RPC Data Quality

The applications of RPC offline monitoring consist of:

- giving informations about the status and the behaviour of the detector almost in real-time, spotting possible problems which can occurs during detector operation;
- defining the quality of data recorded and therefore the possibility to be used for analysis;
- defining the effective detector working parameter (such as efficiency, cluster size, etc.), which must be used to obtain Monte Carlo simulation as realistic as possible.

In this chapter, the second and the third items will be detailed, whereas the results of the application of monitoring package to study detector performance are postponed to next chapter.

5.1 Muon Spectrometer Data Quality Chain

Data quality is a crucial issue for physics analysis. The data quality process has been introduced with the aim of marking reconstructed data of every run as usable or not for performance and physics analysis in ATLAS experiment. Because the size of the ATLAS collaboration and the complexity of the detector, it is necessary to use a tool that allows final users to extract good runs. This tool is designed to hide technical detector details to final users.

The quality information of detectors is summarized in “traffic lights”-like flags [41], that can assume five values described in table 5.1. Data quality flags are generated for each sub-detectors and for each data quality source (detector control system, on-line and off-line) and have the time granularity of one luminosity block. All informations are stored in a dedicated conditions database: in total, there are more than 100 data quality flags recorded. As a result, by analysing the data quality flags obtained above, official *good run lists* (distinct for individual

Status	Light	Description
Disabled	black	indicates that the system has been disabled.
Undefined	gray	indicates that a clear statement cannot be made (for example in case of short runs with a few statistics or in case or data quality problems).
Bad	red	indicates that the fraction of data is considered not suitable for physics analysis.
Good	green	indicates that the fraction of data is considered suitable for physics analysis.
Flawed	yellow	indicates that data are not good, but are possible recoverable. The flag is *yellow* if a calibration work or the precise status determination is still underway, and the use of the data should be postponed until the work has been finalized (in the chosen model, after the final reprocessing the detector status should be only *good* or *bad*).

Table 5.1: Data quality status flag codification.

physics objects) are defined and delivered to physics group for physics analysis and publication of physics results.

Data monitoring is first done online, on a sampled subset of the events being recorded, to quickly spot problems and instabilities. We focus here on offline monitoring, which is performed after the data has been taken, ideally in parallel to the event reconstruction chain (see Figure 5.1), at the CERN computer farm *Tier-0* (see section 4.1.2). Muon offline monitoring ensures that the initial data is satisfactory (first pass) or that the calibrations are valid (second and higher passes). The off-line data quality process of ATLAS is based primarily on analysing histograms produced by monitoring tool that runs in Athena (see chapter 4). These tools are active during prompt reconstruction but can also be used independently. Tools are already implemented to monitor information ranging from hardware readout errors to dimuon masses for J/ ψ and Z reconstruction.

There are two ways by which the histograms are analysed:

manual checks: histograms are viewed by shifters, both in ATLAS control room during data taking and off-line after run end;

automatic checks: the automatic tool DQMF (*Data Quality Monitoring Framework*) [42] performs checks of histograms by applying specific methods (detailed below) and publish the resulting flags on web pages.

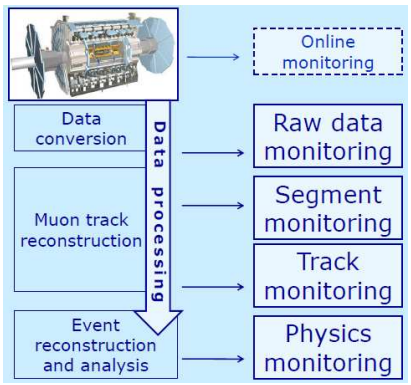

Figure 5.1: Schematic diagram of the flow of the offline muon Data Quality Monitoring with respect to the data processing.

The monitoring algorithms can only use a limited amount of memory (typically no more than 100 MB per algorithm) and time (less than a second per event); this is particularly important for central processing of raw data at CERN, so that monitoring histograms are created as soon as the data itself is available.

5.2 RPC Data Quality

Data quality plots are automatically presented in a dedicated web page [1], figure 5.2 shows links to different technologies plots, in particular links to folders in which RPC histograms are grouped are expanded; plots which are mainly meant to be checked by human shifters are detailed in paragraph 5.2.1, whereas automatic checks of histograms are shown in paragraph 5.2.3.

5.2.1 RPC Shifter plots

In this section the subset of histograms produced by monitoring package and checked by data quality shifter is presented. Shifter plots give the general status of the detector at one glance, without knowing RPC detector details.

RPC plots

The two-dimensional plot Figure 5.3(a) shows the geometrical map of η vs ϕ view trigger hits of RPC in the spectrometer. The chosen coordinates are the

[1] https://atlasdqm.cern.ch/webdisplay/tier0/

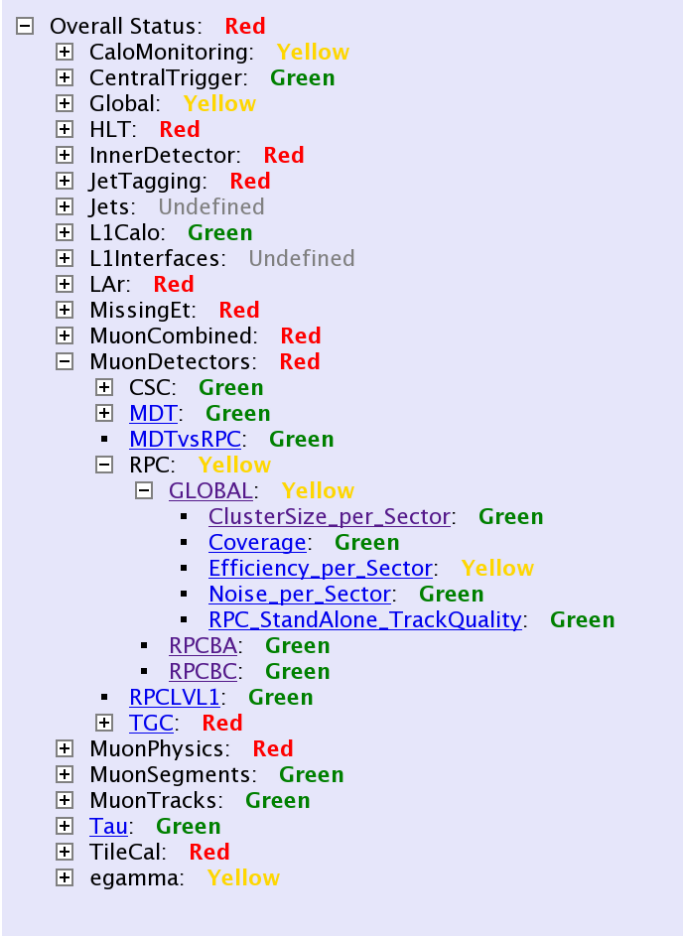

Figure 5.2: Links on the ATLAS off-line data quality web display (RPC folders are expanded).

pseudo-rapidity and the azimuthal angle. It is intended to show the RPC trigger geometrical coverage.

There are other two-dimensional plots showing the total counts of RPC in LowPt and HighPt stations, without distinguish between η and ϕ view hits. It is intended to show the RPC trigger layout coverage. The two-dimensional plot of Figure 5.3(b) shows the total counts of RPC without distinguish between η and ϕ view hits. On the x axis there is the η station number within a geometrical sector. On the y axis there are shown the total counts of LowPt, Pivot, and HighPt planes for all geometrical sectors.

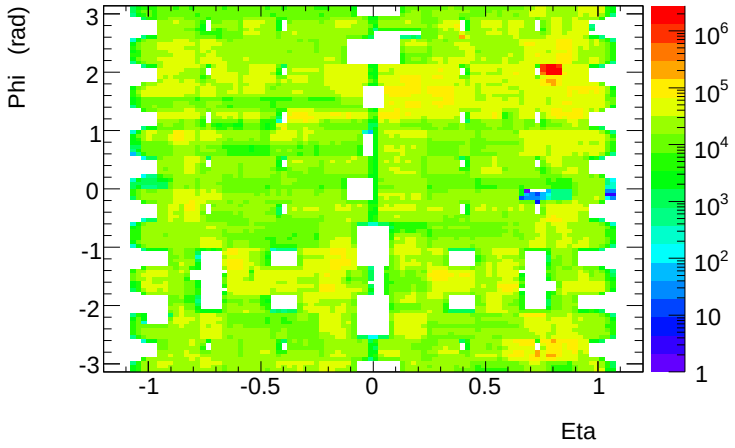

(a) RPC LowPt trigger hit map in (phi,eta) plane.

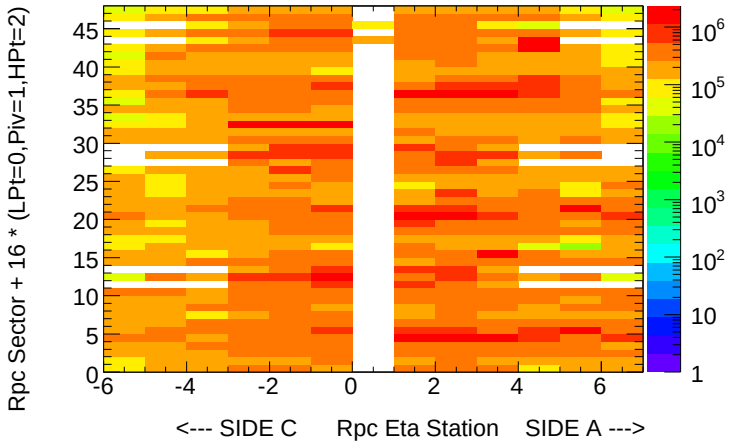

(b) RPC hit chamber map.

Figure 5.3: Examples of RPC general status plots in 'RPC/GLOBAL' folder (data are cosmics muons taken during November 2009).

RPC level 1 plots

Regarding to monitoring of RPC triggers (see section 4.3.1), the plot of Figure 5.4(a) shows the combination of LowPt RPC layers inside a coincidence matrix in correspondence to a trigger hit in the readout for each RPC Sector Logic. On the y axis, the LowPt and HighPt trigger combinations are shown separately, the first one at the bottom part of the plot and the second one in the upper part.

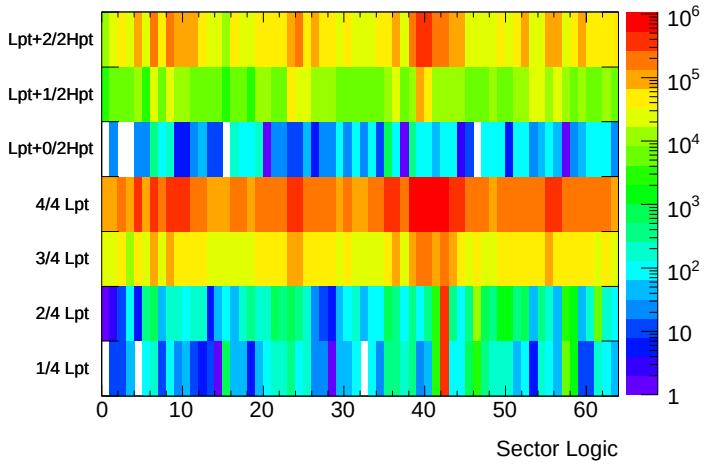

(a) Counts of trigger layers pattern vs sector logic.

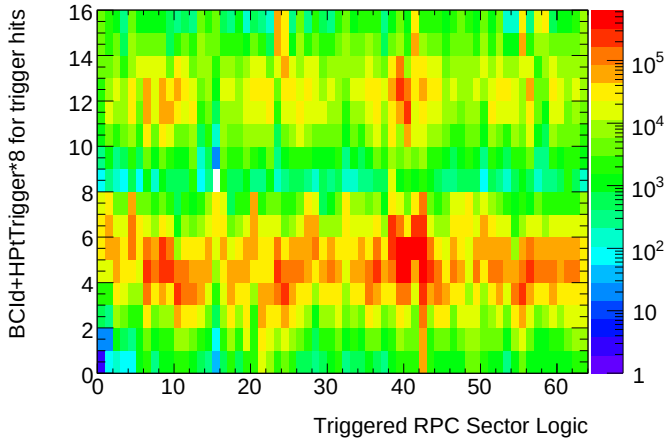

(b) RPC hits bunch crossing time for LowPt and HighPt trigger in phi view vs sector logic.

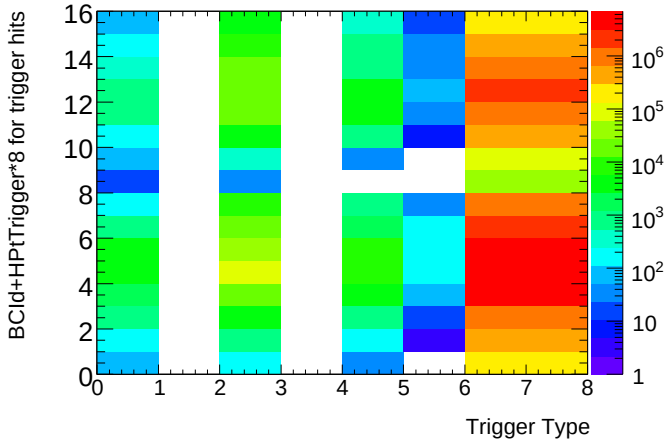

(c) RPC hits bunch crossing time for LowPt and HighPt trigger in phi view vs trigger bit position.

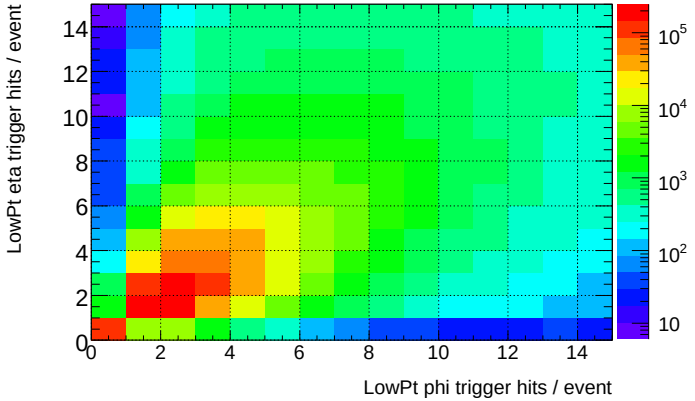

(d) Scatter plot between LowPt trigger hits in phi view and eta view.

Figure 5.4: Examples of RPC general status plots in 'RPCLV1/GLOBAL' folder.

The fact that bins corresponding to combinations forbidden by trigger requirements are not empty indicates possible problems in RPC electronics. The plot of Figure 5.4(b) shows the time distribution for each Sector Logic of the Phi view RPC channel hits. LowPt hits time and HighPt hits time are shown separately in the plots along the y axis, the first one at the bottom part of the plot and the second one in the upper part. This plot of Figure 5.4(c) shows the RPC trigger time distribution (ranging from 0 to 7 BCID) vs the event trigger type bit (ranging from 0 to 7). The plot of Figure 5.4(d) shows the correlation between η and ϕ trigger hits (in the case of low p_T trigger): the two views trigger are strongly correlated and the first bins along the diagonal should be the most populated.

MDT and RPC correlation plots

The spatial and time correlation between MDT and RPC must be taken under control. To easy spot possible problems the plot shown in Figure 5.5 is used. This plot shows the distribution of the spatial residual along z (bending view) between RPC hits (strip position) in eta view and a MDT Hit (wire position) belonging to the same muon station and having RPC plane and MDT multilayer near-by. The residual distribution is about centred around zero with a spread of about 50 cm. Any significant deviation from these values spot a synchronisation problem for one or both detectors.

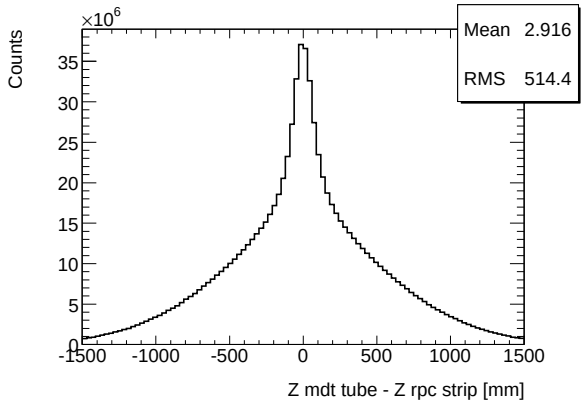

Figure 5.5: Distribution of the difference between MDT tube z coordinate and RPC eta strip z coordinate

RPC standalone tracks

The aim of these plots is to provide a quick overview of the quality of the muon tracks selected by the RPC.

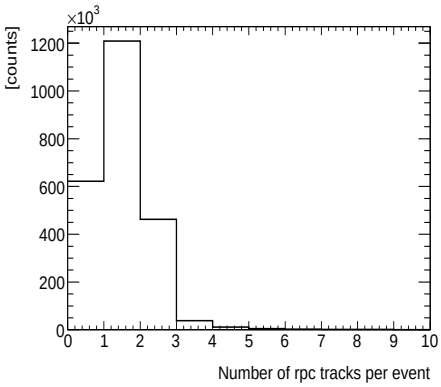

(a) RPC tracks multiplicity per event.

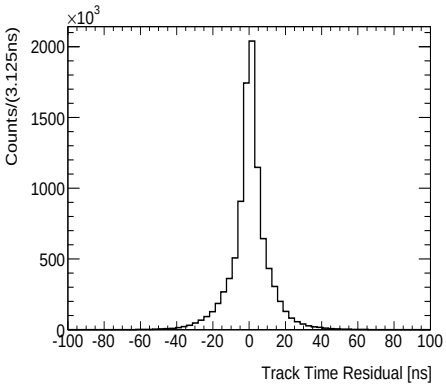

(b) RPC track hit time deviation from the average.

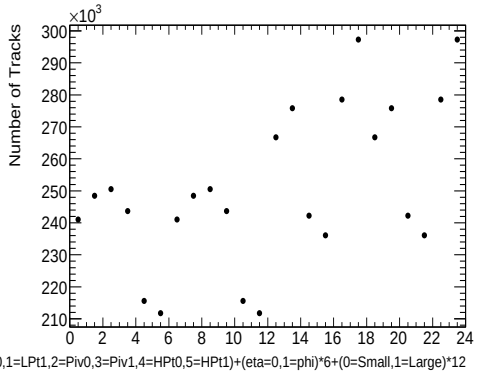

(c) Number of RPC tracks projected on the removed layer.

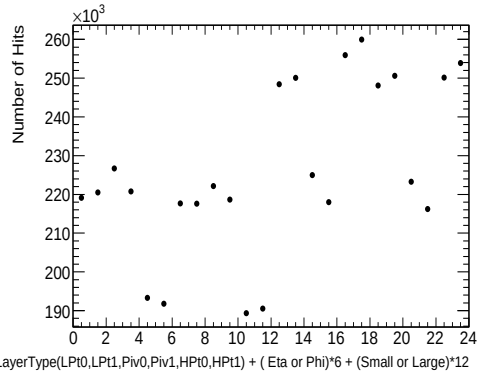

(d) Number of RPC tracks projected on the removed layer and matching RPC cluster hits.

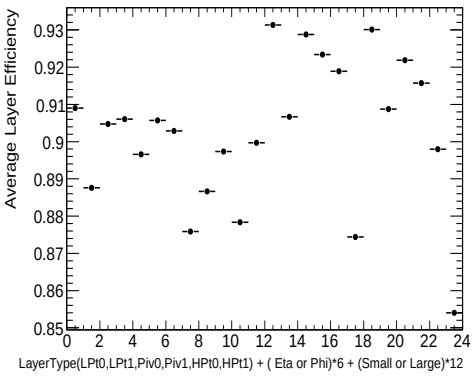

(e) Average layer efficiency with respect to RPC track coverage.

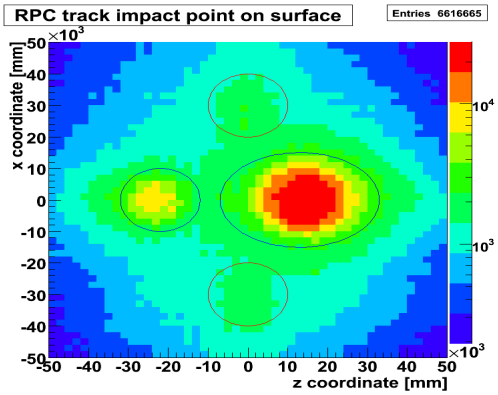

(f) Cosmic muon map reconstructed on surface (z = 81m).

Figure 5.6: Examples of RPC track general status plots in 'RPCStandAloneTrackMon/GLOBAL' folder. Data are from physics-RPCwBeam stream and run 113860 (6,600,000 events analysed).

The plot of figure 5.6(a) shows the distribution of the number of tracks reconstructed in each event, provided by the RPC standalone reconstruction algorithm.

The plot of figure 5.6(b) shows the distribution of the Root Mean Square values of RPC hit times belonging to a single RPC standalone track. After RPC timing calibration, a spread much less than one bunch crossing is expected.

The plot of figure 5.6(c) and 5.6(d) shows the total number of tracks extrapolated on each RPC layer and the number of extrapolated tracks with a near-by hit. The RPC layers are divided in Large and Small sectors, in Eta and Phi views for a total of 24 bins.

The plot of Figure 5.6(e) is the ratio of the two previous plots and shows the efficiency.

The plot of Figure 5.6(f) shows the two-dimensional distribution of impact parameters of tracks reconstructed by the code RPCStandAlone, extrapolated to the surface. Are clearly visible the areas from which comes the greatest number of muons reconstructed by the RPC, which correspond to the two holes of the ATLAS experimental cavern, through which the ATLAS component were descending for installation. Besides these areas, there are two secondary areas across which a not negligible [1] number of muons reaches the detector. These areas are related to the shaft of the experimental cavern lifts.

The shifter plots above described are summarized in the table 5.2 according to corresponding monitoring algorithm.

5.2.2 Data Quality Monitoring Framework

The *Data Quality Monitoring Framework* (DQMF) [42] is a software tool developed to perform automated analysis on monitoring data and to encode results in flags as defined in table 5.1.

The DQMF is based on applying some operations on histograms produced by monitoring package: for example, the operation can be the evaluation of the mean or the RMS of a histogram, the Kolmogorov test, the counting of the number of bins with content above or below a predefined threshold, a comparison with a predefined histogram used as reference, etc. The numerical result of these operations is compared with the thresholds which define the *good* and *bad* interval. The operation are defined in the *DQMF algorithm*, that are managed by a general *configuration script*.

Figure 5.7 shows an example of application of DQMF to the two-dimensional plot showing the trigger coverage of RPC in side-A of "low p_T " stations. Each bin in

[1] The not negligible amount of cosmics from elevator shafts, smaller than cavern holes, was unexpected. This "discovery" of ATLAS elevators was an unintentional application of physics Nobel prize L. W. Alvarez proposal [43] to search hidden rooms in Egyptian pyramids by looking at cosmics flux anysotropy.

RpcLv1RawDataValAlg

Type	Title	Description
TH2I	TriggerCondition_vs_SectorLogic	Majority trigger logic vs Sector Logic
TH2I	rpclv1_BCid_vs_SectorLogic	Trigger Bunch Crossing vs Sector Logic
TH2I	rpclv1_BCid_per_TriggerType	Trigger Bunch Crossing vs type of trigger

RpcRawDataValAlg

Type	Title	Description
TH2I	EtavsPhi_TriggeredMuons	LowPt trigger map in (ϕ,η) plane
TH2I	GlobalHitsPerRPCMiddle	RPC Middle Station hit map
TH2I	GlobalHitsPerRPCOuter	RPC Outer Station hit map
TH2I	rpc2DEtaStation	RPC Station hit map

MdtVsRpcRawDataValAlg

Type	Title	Description
TH1I	MdtRpcZdifference	RPC and MDT residual along z

RPCStandaloneTracksMon

Type	Title	Description
TH2I	rpczxSurfaceView	RPC track map on surface
TH2I	rpctrack_bvseta	RPC track pseudo-rapidity vs impact parameter
TH1I	rpcNtracks	RPC number of tracks per event
TH1I	TimeTrackResidual	RPC track cluster time residual
TH1I	Track_Projected_on_Layer	RPC projected tracks on RPC layer
TH1I	Hit_on_Track_Layer	RPC projected tracks with corresponding hits
TH1I	Layer_Efficiency	RPC layer average efficiency

Table 5.2: RPC Shifter plots with a short description.

the histogram corresponds to one RPC chamber (in the x axis there is the chamber index and all 16 RPC sectors are unfolded in y axis) and contains the number of RPC Low p_T trigger signals. The DQMF algorithm (all operational parameters are reported in figure) used here checks (for every bin) if the bin content is above the threshold (the parameter `BinThreshold` set to 5 in this case). The total number of bins satisfying the above condition, called `NBins`, is the central parameter of the algorithm: it is compared with the auto-explicative thresholds of red and green

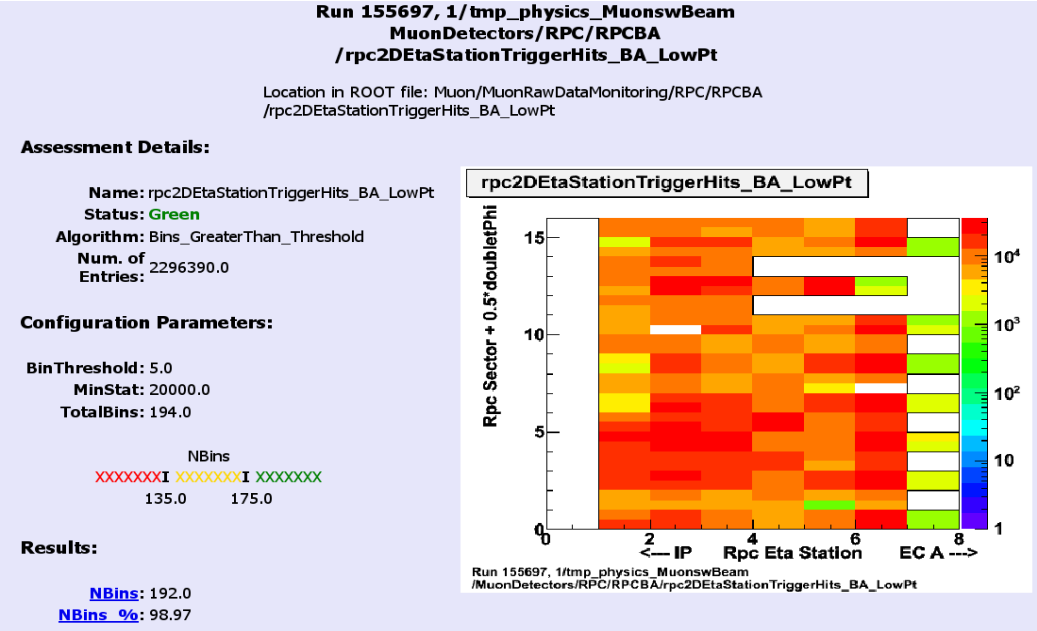

Figure 5.7: Example on automatic algorithm application on plot showing the trigger coverage of barrel A side of "low p_T " planes.

intervals reported in the figure. In this case, the RPC chambers with trigger coincidence are 192 over 194[2], the coverage is nearly to 99% and the resulting status (regarding the geometrical coverage) is *good*. The check is performed only if the statistics is over the value `MinStat` (otherwise the flag is set to *undefined*).

The DQMF infrastructure stores all results in database and provide also an *history* tool to monitor the detector performance over the time. As an example, the figure 5.8 reports the trend of the RPC trigger coverage percentage (of side A Low p_T) for 2010 runs (with more than one million of events).

5.2.3 RPC Data Quality plots

The offline monitoring provides histograms to the Data Quality procedure which for each run flag the sub-detectors and triggers performance as good or not for data analysis. The plots used as input to the Data Quality procedure are stored in the two folders: `'RPCBA'` and `'RPCBC'` (see figure 5.2), according to Side A and Side C. In fact, the data acquisition system is completely separated in the two sides (DAQ partitions).

The figure 5.9 reports off-line histograms of the subdirectory "RPCBA" as are

[2]The bins outside the black contour in the plot not correspond to real RPC chamber and are not counted in the number of total bin equal to 194.

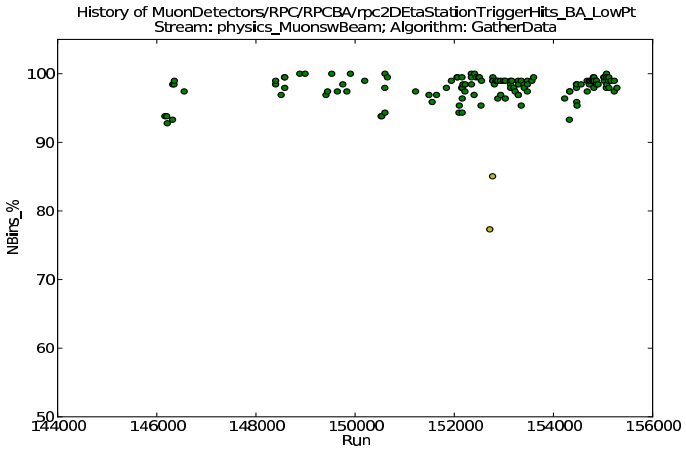

Figure 5.8: Trend of the RPC coverage (in percentage) of side A low Pt RPC chambers during 2010 operations (only data related to run with more than 100000 events are reported).

displayed in the data quality web page. The coloured histograms border correspond to flags obtained by DQMF (section 5.2.2) tool.

The plot of Figure 5.9(a) contains the distribution of the average readout panel cluster size. This correspond to one of the summary plots of the quantities analysed in the monitoring code (see Section 5.3), but separated in side A and C. The data quality flag is set *green* if the average cluster size is below 2.1 and set *red* if above 2.4.

The plot of Figure 5.9(b) contains the average layer efficiency taking into account only side A. This correspond to one of the shift plots but separated in side A and side C. The applied algorithm checks if the histogram is not empty.

The plot of Figure 5.9(c) show the distribution of the number of hits per event for Side A. The peak in these distributions are generated by the hits of events produced by muons, while the tail may be associated with noisy events or events containing multiple muons. The data quality flag is set *green* if the average value of this hits are below 50 and set RED if above 80. The flag is GREEN if the histogram is not empty.

The plot of Figure 5.9(d) show a two-dimensional map of trigger hits generated by "LowPt" coincidence. On the x axis there is the Eta station number along a geometrical sector, ranging from 0 to 7 for Side A, and from -1 to -7, for Side C. On the y axis there is the geometrical sector number ranging from 1 to 16, but with 32 total bins in order to have separate counts for different sector logic (doubletPhi) inside the a geometrical sector. Similar plots are realized with the hits generates by HighPt coincidence. LowPt and HighPt trigger hits maps, provide a

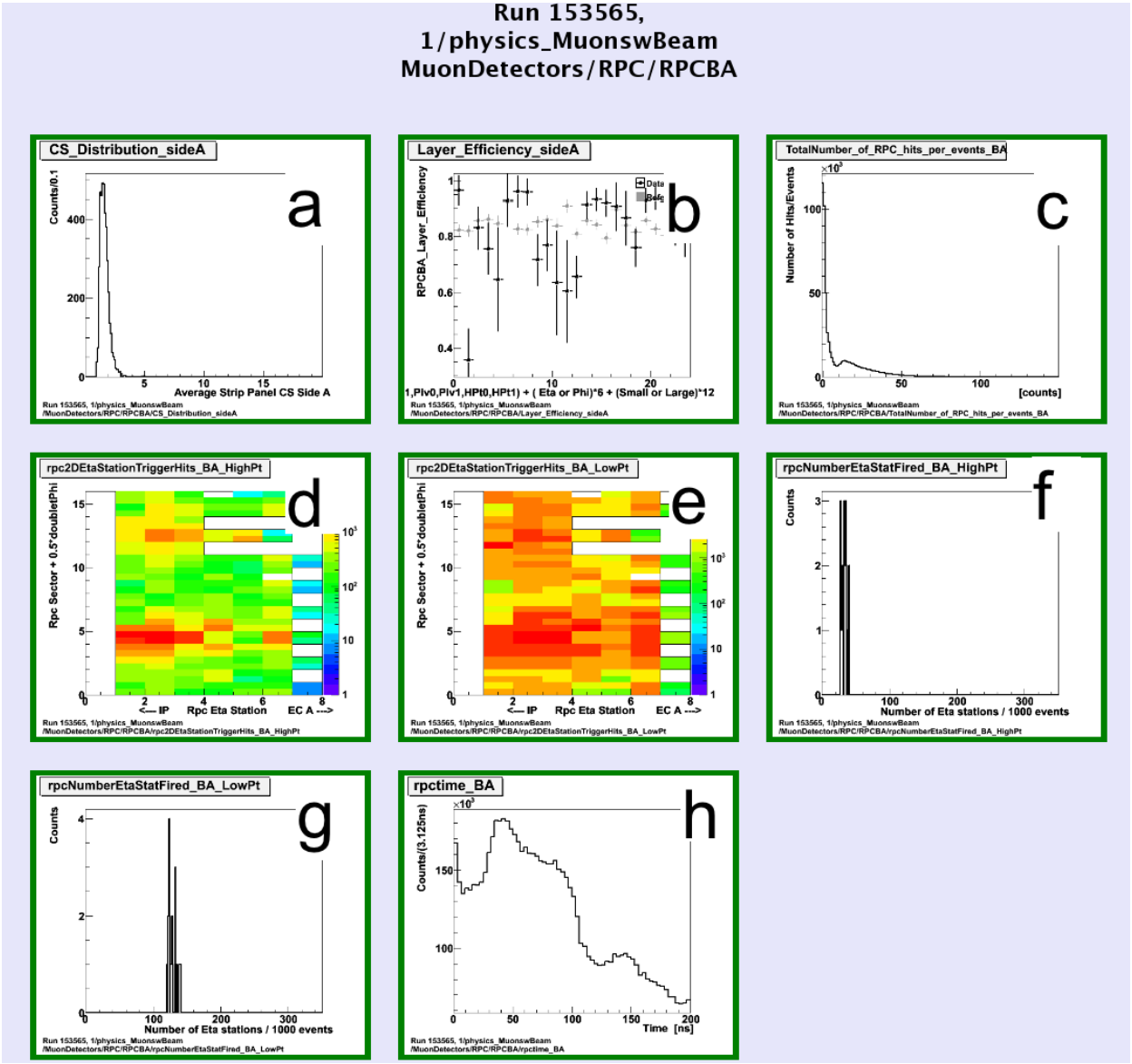

Figure 5.9: Screenshot of web page displaying histograms of RPCBA folder. Colour box surrounding graphs result from applying data quality algorithms.

measure of the trigger coverage in the spectrometer barrel region. The choice of binning equal to the segmentation of the trigger towers, allow an easy identification of noisy towers or those that do not provide triggers. The data quality flag is set *green* if the number of station with trigger hits are above 95% of the total and set *red* if below 90% of the total. There is a threshold set to 5 in order to count a station as having trigger hits. A similar map and algorithm exist for trigger hits

generated by HighPt coincidence (figure 5.9(e)).

The plot of Figure 5.9(f) and 5.9(g) are filled each time that a data block is closed with the number of the RPC η stations (of respectively pivot and high p_T plane) that have at least one trigger hit. For a run with stable and uniform trigger and readout system, this number is expected to be constant and the distribution should be very narrow. The data quality flag is set *green* if the spread in the number of responding station is below 15 and set *red* if above 30 .

The plot of Figure 5.9(h) shows the distribution of the raw hit times without any selection. During the commissioning with cosmics the RPC readout window size is set to the largest size of 200 ns (eight bunch-crossing). Cosmic muons arrive randomly with respect to the bunch-crossing clock and the time distribution is flat inside the time window (25 nsec) of the bunch crossing window selected by the trigger. After RPC time adjustment a single uniformly populated bunch crossing is expected. During beam collisions, the muons produced by the interaction arrive synchronous with the bunch-crossing clock and a very tight distribution inside a single bunch crossing expected. The data quality flag is set GREEN if the time spread is less than 45 ns and set RED if above 60 ns.

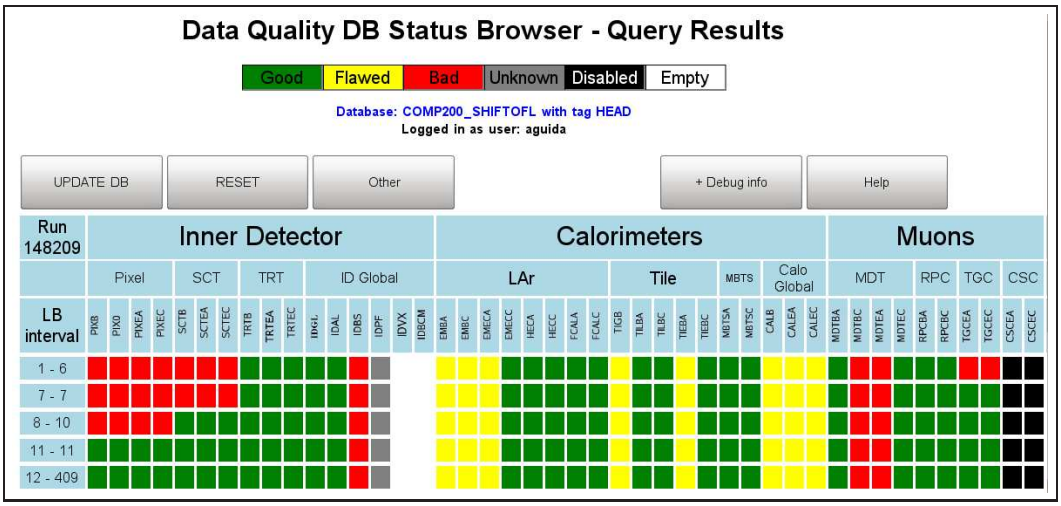

Figure 5.10: Screenshot of the web interface to the data quality flags database. The off-line flags for the all technologies of four ATLAS subdetectors are shown, each one segmented in side A/C. On the left is shown the luminosity block validity range of the flags.

Detector off-line flags obtained from a ATLAS physics run are shown in figure 5.10.

5.3 Summary plots

The monitoring package produces several histograms which summarize for each sector the average and the spread of the main readout panel quantities. These "summary" histograms are one dimensional histograms and, on the x-axis, one bin corresponds to one RPC read-out panel and the correlation between panel index (in the histogram) and physical coordinates (defined at pag. 66) is done by the formula:

$$\begin{aligned} \texttt{index} = \big[& \texttt{view} + (\texttt{gasgap} - 1) * 2 + (\texttt{doubletPhi} - 1) * 4 \\ & + (\texttt{doubletZ} - 1) * 8 + \texttt{Plane} * 24 \\ & + \texttt{abs}(\texttt{StationEta}) * 72 \big] * \texttt{sign}(\texttt{StationEta}) \end{aligned} \tag{5.1}$$

`Plane` is 0 for Lowp_T panels, 1 for Pivot and 2 for High Pt. With this choice the readout panel of Side A (positive bins) and C (negative bins) are clearly separated and the eta readout panel is followed by the corresponding phi readout panel.

The monitored basic quantities characterizing the RPC detector response and shown by summary plots are the following:

- readout panel efficiency
- gas volume efficiency
- average readout panel cluster size
- average readout panel spatial residual for cluster size 1
- average readout panel spatial residual for cluster size 2
- average readout panel spatial residual for cluster size larger than 2
- average readout panel spatial resolution for cluster size 1
- average readout panel spatial resolution for cluster size 2
- average readout panel spatial resolution for cluster size larger than 2
- average readout panel time
- average readout panel occupancy
- average readout panel correlated noise
- average readout panel total noise

With the summary histograms, it is possible not only to spot the presence of a problem, but also to investigate which panel has a problematic behaviour regarding to quantities listed above.

Another crucial task of summary histograms is the storing panel informations that has to be written in the *detector conditions database*.

The effective RPC working parameters (efficiency, noise and cluster size) are measured by using the summary histograms with the read-out panel granularity and then are stored, run by run, in a database. This allows to know the real operational conditions, which must be used to simulate, in Monte Carlo production, the detector response more realistic than possible. In fact, all physical measures will be weighted by detector parameters to spot the systematic uncertainties on measures.

One example of summary plot is shown in figure 5.11(a) where the measured quantity is the average readout panel efficiency with its error.

In addition to the summary plots, for each sector and for physical quantities of interest, distribution plots are made. One example is shown in the figure 5.11(b) for the efficiency. More precisely, the summary plot distribution per sector are evaluated for the previous quantities and for the spatial residuals spread for cluster size one, two and bigger than two, for a total of thirteen summary distribution plots.

Furthermore, histograms showing the distribution for side A and C separately of all the above quantities are also produced.

Summary histograms like the previous ones but relative to the single RPC strip instead to one readout panel are also available. This plots shows all the strips (both Eta and Phi views) along the X axis of a geometrical sector layer with a specific doublet Phi. These fully detailed histograms are not generally produced (except one) in standard reconstruction process at Tier-0, because the huge amount of memory required, but are only used by detector expert for very detailed RPC controls.
The only histogram with strip granularity produced at tier-0 contains the strip hit counts (*strip profile plot*) and it is used for the evaluation of noisy and dead strips by counting, at the end of run, the number of bin entries with respect to the total number of events.
An example of profile plot is shown in the Figure 5.12.

Results about the evaluation of the fraction of dead strips in RPC detector will be discussed in section 6.2.1.

Histograms merging procedure

Data belonging to one run are stored in thousands of data files (because ATLAS DAQ collect and store data in files which for safety reason can not be more large than 2 GB) which are analysed separately by the monitor code. In order to use the full run statistics a merging procedure starts automatically at tier-0 computing farm when the data run processing is finished. The merging procedure by default add bin by bin the content of the same sub-histograms.

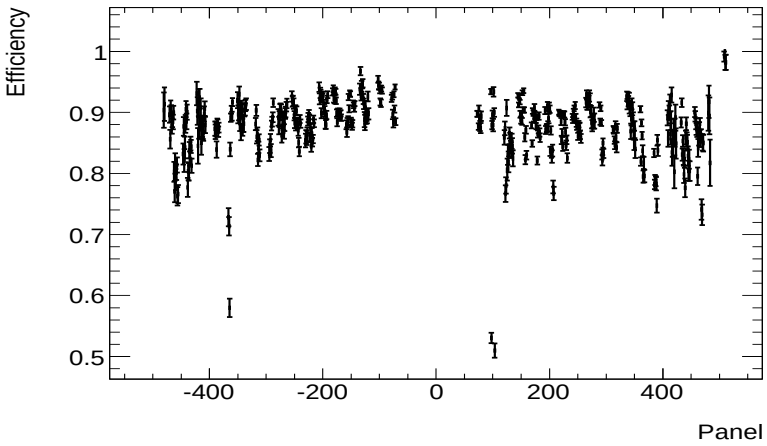

(a) Average readout panel detection efficiencies. The panel index on x axis is obtained from 5.1.

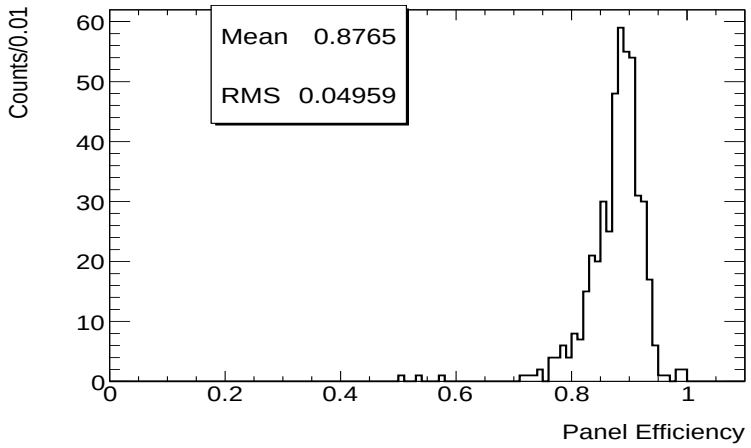

(b) Distribution of average readout panel detection efficiency

Figure 5.11: Examples of RPC efficiency summary plots related to sector 7. Data are cosmics taken during November 2009.

For quantities such as efficiencies, averages and normalized counts, the merging operations are more complicated and a specialized RPC code was written (*RPC post process algorithm*).

In general, an efficiency is evaluated as the ratio between the number of projected tracks with the associated hits N_h and the total number of extrapolated tracks N_p:

$$\epsilon = N_h/N_p. \tag{5.2}$$

and assuming binomial errors with an uncertainty given by:

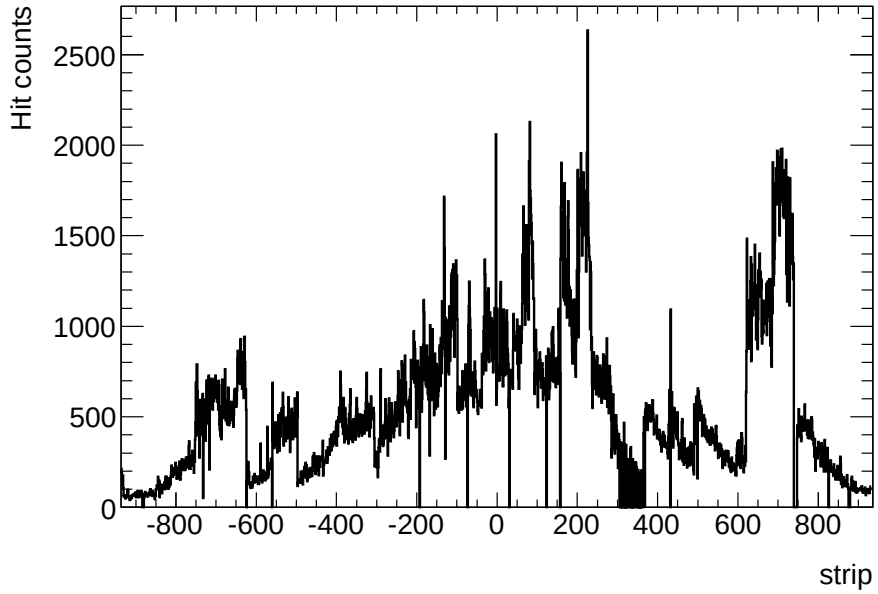

Figure 5.12: Examples of RPC single strip profile plot (obtained from November 2009 cosmics data) .

$$\sigma_\epsilon = \sqrt{\frac{N_h}{N_p}}\sqrt{1-\frac{N_h}{N_p}}\sqrt{\frac{1}{N_p}} = \sqrt{\frac{\epsilon(1-\epsilon)}{N_p}}. \tag{5.3}$$

The quantities N_h and N_p are merged by the regular add operation and from them the *RPC post process algorithm* evaluated the efficiencies with the errors.

For the average quantities $\overline{value}$ and their spread we have available the relative extensive quantities needed to evaluate the average and the spread: the sum of the entries $N_{entries}$, the sum of the values N_{value} and the sum of the squared values N_{square}. These quantities could be merged by the regular add operation and the *RPC post process algorithm* from them evaluates the average, the average of the square and the spread by the following formula:

$$N_{entries} = \sum_{i=1}(entries)_i \tag{5.4}$$

$$\overline{value} = \frac{N_{value}}{N_{entries}} = \frac{\sum_{i=1}^{N_{entries}}(value)_i}{N_{entries}} \tag{5.5}$$

$$\overline{value^2} = \frac{N_{square}}{N_{entries}} = \frac{\sum_{i=1}^{N_{entries}}(value_i)^2}{N_{entries}} \tag{5.6}$$

$$spread = \sqrt{\overline{value^2} - \overline{value}^2} \tag{5.7}$$

The bin content and its error are set equal to the average and the spread of the quantity respectively. Similarly, the occupancy and the noise quantities are evaluated by the corresponding unnormalised plots divided by the total event number. The readout panel summary, the sector distribution, the data quality distributions and the single strip summary are then re-computed to account for the final estimate of those values by the *RPC post process algorithm*. The summary plots and the distribution plots are filled with significant quantities only at the end of the process.

These kind of merging technique required to add several additional auxiliary histograms which are memory consuming and then a careful optimisation had to be taken into account.

Finally, after the end of merging procedure, a dedicaded module of *RPC post process* algorithm write out the summary results (average efficiency, clusters size, timing, etc.) for each panel in a database.

6

Performance of ATLAS RPC detector

6.1 Introduction

In this chapter will be presented a detailed discussion about the results on the analysis of the RPC performance. This analysis was performed both using cosmic ray data taken during the commissioning period (from the end of the installation in the cavern until the starting of the beam operation in autumn of 2009) and beam data, particularly data registered in special runs with the so-called "beam splash events". In addition, in November 2009, to characterize the detector response at the starting of the physics program of ATLAS experiment and to know the trend of fundamental parameters (like efficiency and cluster size) as function of electric field applied to RPC, several runs with high voltage set to different values were taken (RPC high voltage "scan"). This is important also to check if RPC were operated at the proper working point.

All the results were obtained by running the RPC monitoring package, described in previous chapter 4. In some cases, to perform a more detailed analysis than that allowed at CERN-Tier0 facility, the package was run in private preprocessing sessions, using the CERN computing farm dedicated to users analysis and using the worldwide distributed computing resources system called GRID. For this purpose, dedicated scripts were developed. The distribution plots showed below were obtained from ntuples dumped out by database file produced by the RPC post-process tool (section 5.3). This method allows to store the relevant RPC operation parameter (efficiency, cluster size, etc.) for each read-out panel in a file with database structure. Therefore, it was easy to manage a large amount of data, to make statistical analysis over detector properties, to apply cuts on data and make comparisons.

6.2 Studies with cosmics data

A commissioning effort has been on-going by taking data with cosmics rays when the first sub-detectors were partially installed in the ATLAS pit [44, 45]. This final

chapter presents the results of analysis carried out on cosmic data taken during November 2009, with the full operational detector and with both the solenoid and toroid magnetic fields at full values. Several hundred million cosmic ray events during 2008 and 2009 were triggered by the RPC detector and collected by the Muon Spectrometer in standalone mode or by all ATLAS detectors in combined mode. With these data were possible to show that the ATLAS detector is close to the design performance and that the Muon Spectrometer is ready to identify, to measure and to trigger muons produced in high energy proton-proton collisions.

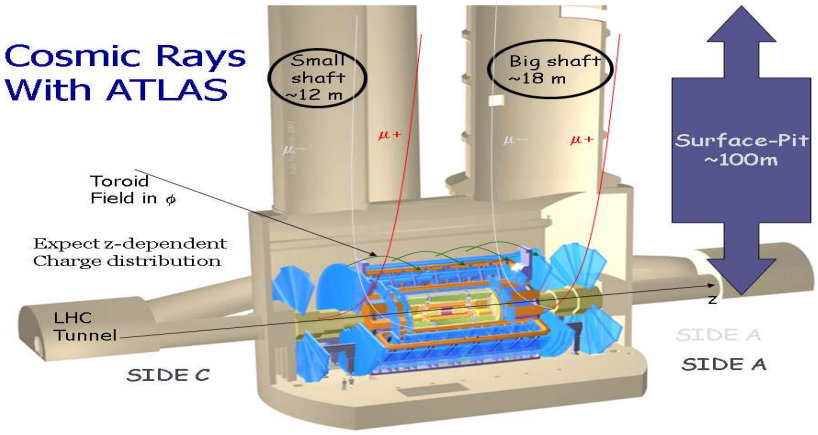

Figure 6.1: Pictorial view of ATLAS detector in underground experimental area.

Cosmic rays are coming predominantly from the vertical direction. They were therefore particularly useful for studying the barrel region of the detector, where they resemble particles from collisions, specially for the bottom sectors where the timing is also similar.

During combined and standalone cosmic ray data-taking periods, a complete tuning and calibration of the detectors was performed as detailed in this Section.

Most of the detector was operational during the cosmic-ray data-taking periods. The cosmic-ray time alignment significantly improved the RPC trigger synchronization with the rest of ATLAS detector up to few bunch crossing.

Given the angular distribution of cosmics, local calibrations are statistically limited by the small acceptance of individual detector modules, especially in the vertical sectors. Therefore it was not possible to perform full calibration of the whole detector with the same statistical accuracy.

The intrinsic detector efficiency measures the probability of a hit being registered in an operational detector element when a charged particle traverses the sensitive part of the element. Both, a high intrinsic efficiency and a low non-operational fraction are essential to ensure good-quality tracking.

The intrinsic efficiencies of the RPC detectors are measured by extrapolating well-reconstructed tracks through the detector and counting the numbers of hits (clusters) on the track and holes where a hit would be expected but is not found.

The measured inefficiency contains instead a contribution from isolated dead strips due to electronics inefficiency for which no correction is applied.

6.2.1 RPC coverage

In order to have a complete picture of the response of the detector, two-dimensional maps of the readout hits were made for all six layers of active detector (figures 6.2, 6.3 and 6.4). Moreover, two-dimensional distributions of the response of the trigger detectors are also produced (figure 6.5).

As explained in chapter 3, the muon trigger selects muons in barrel region identifying them as low-p_T (p_T range approximately between 4 and 10 GeV/c) or as high-p_T (p_T range approximately from 10 to 40 GeV/c) muons. The low-p_T trigger (AtlasLowPt_TriggerOut) is made in BM chambers, the signal is sent to the BO chambers (AtlasHighPt_TriggerFromLowPt) for the final generation of the trigger signal (AtlasHighPt_TriggerOut). In this context, three types of two-dimensional plots are made to monitor the trigger response of the RPC.

These two-dimensional maps are made differently, depending on the use to which they are intended. In the plots meant for the debug of the detector, each bin corresponds to one read-out strip. In this way is easily to identify the fractions of detector that does not work, but non-instrumented zones do not appear in plots. The same plots are reproduced by plotting the geometrical position of the strips. This representation allows the identification of areas that are not instrumented and faithfully reproduces the geometry of the apparatus. Finally, but only for two-dimensional distribution of the triggers information, the plots are also produced according to the coordinates η and ϕ, this to allow consistent comparisons with other systems of the ATLAS detector.

In order to measure quantitatively and define in detail the coverage of the detector, all the not operated strips are identified and monitored. A strip is defined as “dead” if produces less than 5 hits on the front end for a million triggers. In fig 6.7 is shown the number of not operated strips per panel (the fraction of dead strips is about 2% of the total strips).

6.2.2 RPC efficiency

The efficiency of the RPC detector has been calculated by using the standalone algorithm shown in paragraph 4.5. Efficiency was estimated starting from tracks reconstructed with only RPC hits and without hits belonging to RPC plane under measure. When a reconstructed track is extrapolated on RPC plane, a read-out

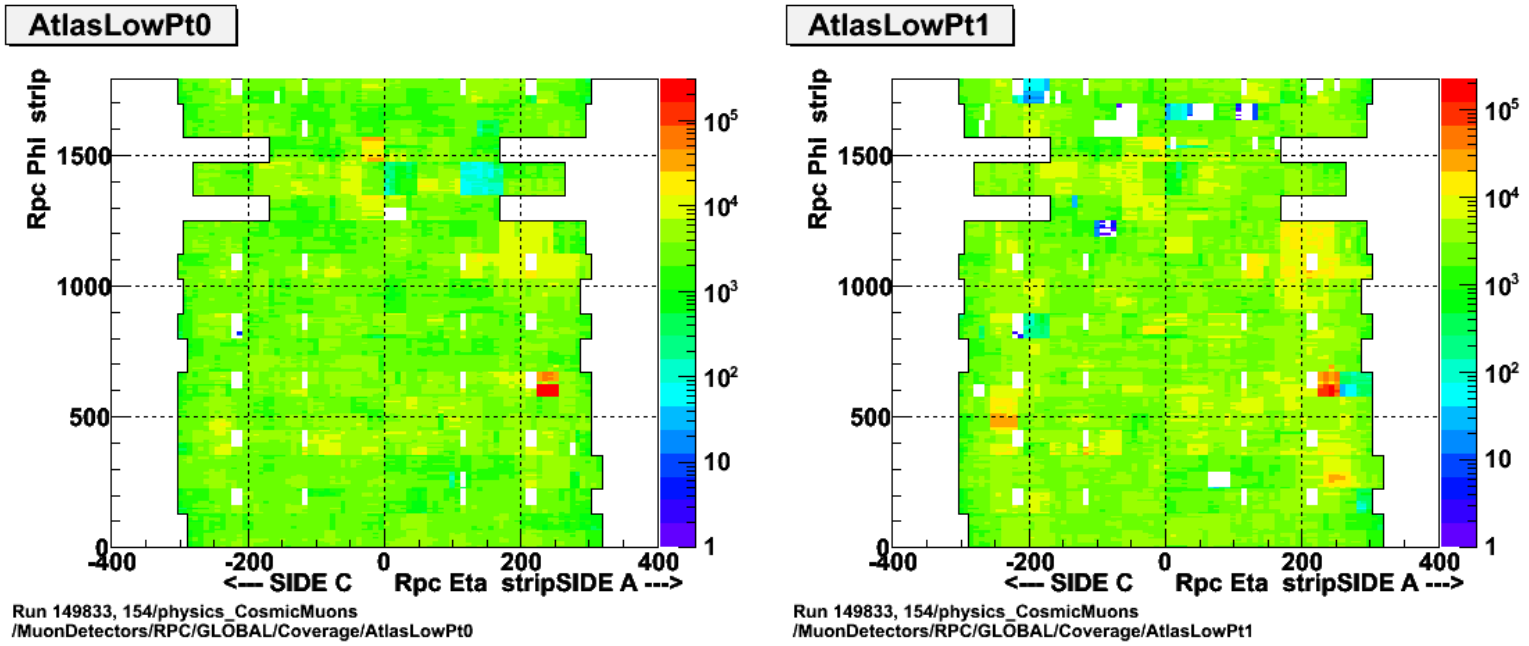

(a) AtlasLowPt0

(b) AtlasLowPt1

Figure 6.2: Detector coverage of RPC LowPt layers in spring 2010 with cosmic muons data.

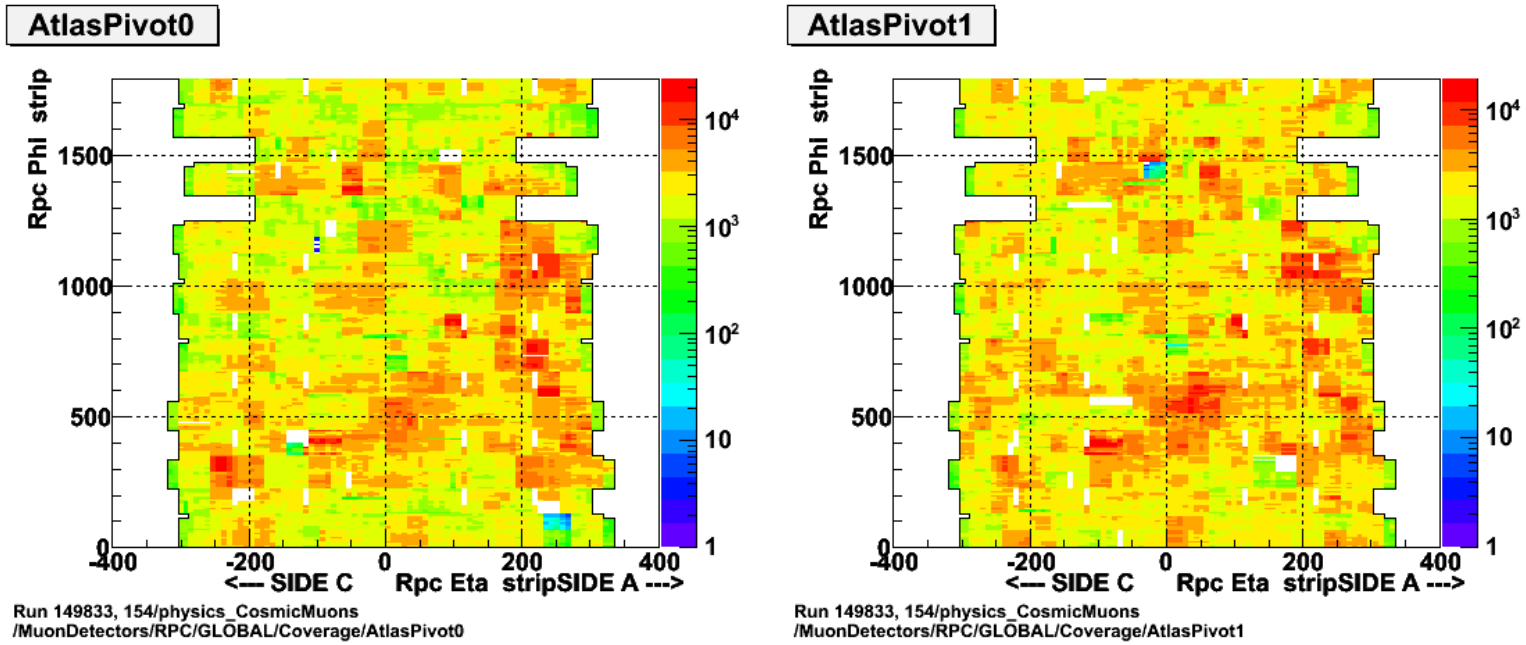

(a) AtlasPivot0

(b) AtlasPivot1

Figure 6.3: Detector coverage of RPC Pivot layers in spring 2010 with cosmic muons data.

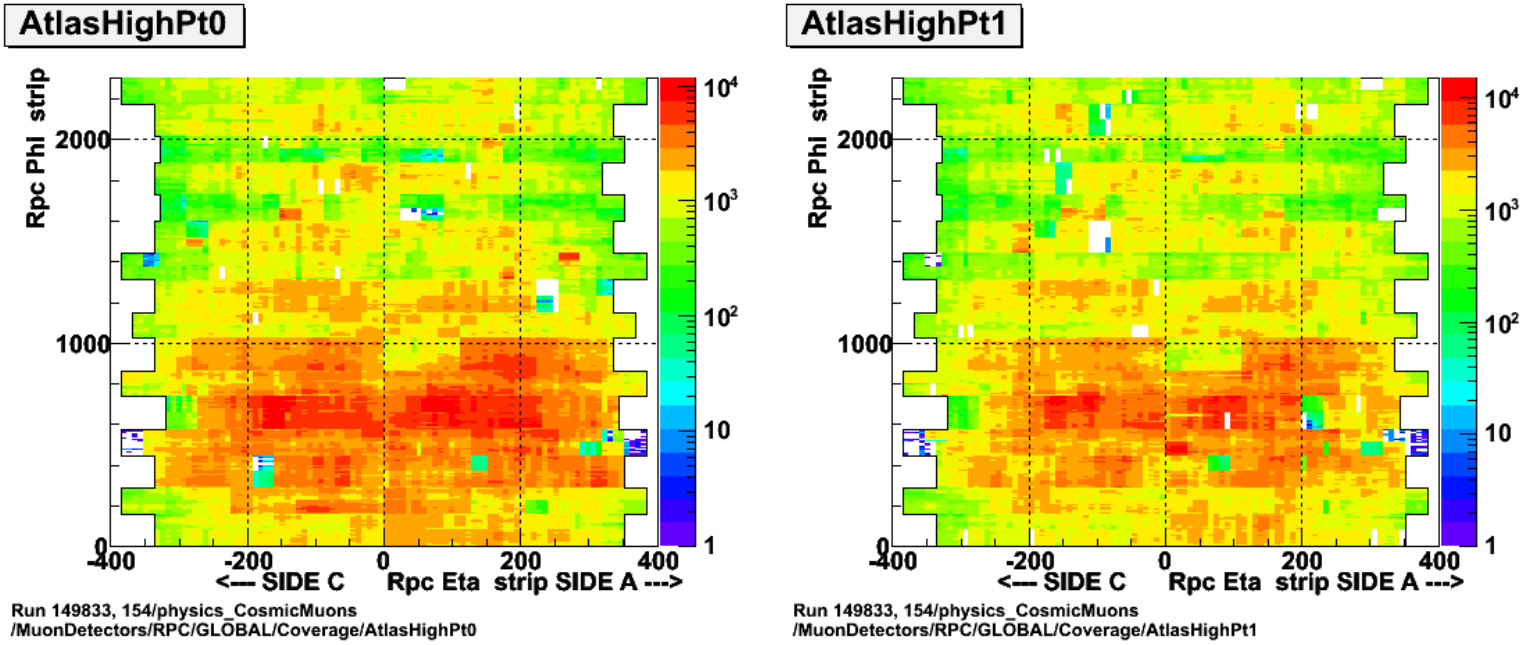

(a) AtlasHighPt0

(b) AtlasHighPt1

Figure 6.4: Detector coverage of RPC Pivot layers in spring 2010 with cosmic muons data.

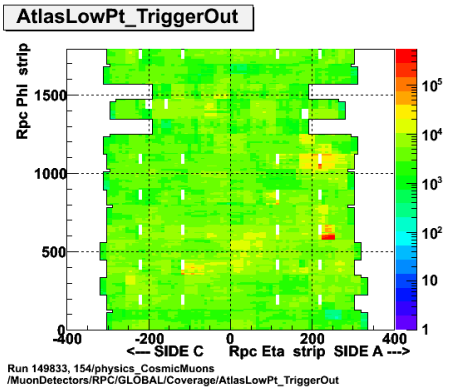

(a) AtlasLowPtTriggerOut

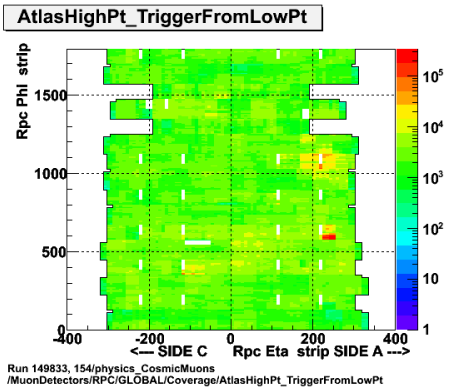

(b) AtlasHighPtTriggerFromLowPt

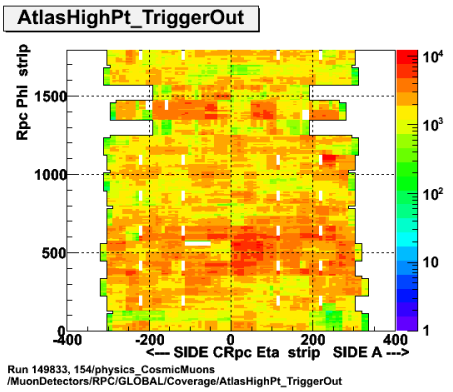

(c) AtlasHighPtTriggerOut

Figure 6.5: RPC trigger coverage in spring 2010 with cosmic muons data.

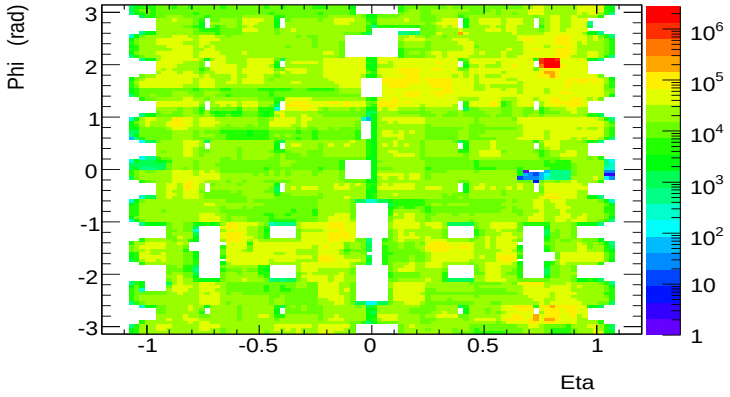

Figure 6.6: LowPt RPC phi and eta trigger hits correlations (in η and ϕ coordinates).

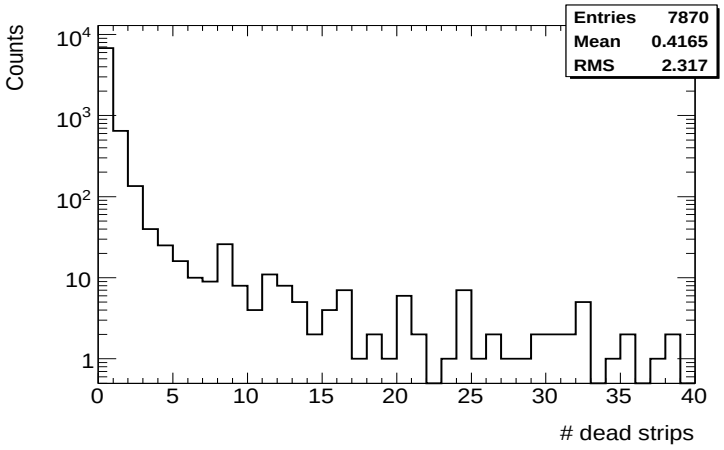

Figure 6.7: Distribution of the number of dead strips for strip readout panel of the RPC detector in December 2009.

electronic panel (or a strip) is declared "efficient" if there is a strip "fired" at a distance smaller than one strip from the extrapolation point. During normal operation periods, not all RPC sectors operate at the same high voltage value, but, because temperature problems, the high voltage of the upper installed sectors (numbered 4, 5 and 6) is set to the lower value of 9400 V (instead of 9600 V). The not uniform conditions have to be taken into account during the data analysis.
Figure 6.8 shows the measured ATLAS RPC panel detection efficiency, each entry is related to a single RPC readout panel. To perform an analysis on a homogeneous sample, only panels with applied high voltage at 9600 V (i.e. all sector except 4, 5 and 6) and with threshold potential equal to 1 V are considered. In addition, to exclude panels not crossed by enough number of cosmic muons to make a significant analysis, a further cut on the statistical sample is applied by requiring a number of extrapolated tracks on the panel greater or equal than 200.

A fit with a Gaussian function performed over the efficiency distribution is superimposed to the histogram distribution and fit parameters are showed inside the figure.

In the same way, we can define the efficiency for the gas gap volumes.
When a reconstructed track is extrapolated on RPC gas volume, we look for a signal on one of the two read-out panels (η or ϕ) located on the opposite side of the gas gap. The *measured* gap efficiency $\overline{\varepsilon}_{gap}$ is defined as the ratio between the number of RPC signals (in at least one of the two panels) and the number of extrapolated tracks.

The efficiency of a read-out panel $\varepsilon^{\eta(\phi)}$ is the product of the gap efficiency ε_{gap} (the probability of occurring an avalanche discharge in the gas when a muon cross it) times the read-out electronic efficiency $\varepsilon_{elet}^{\eta(\phi)}$ (the probability that the avalanche

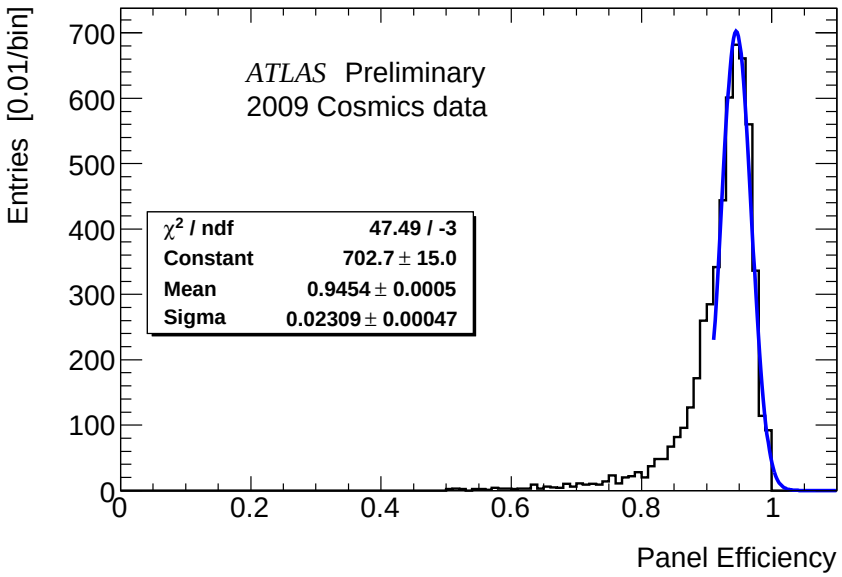

Figure 6.8: Distribution of RPC strip readout panel average efficiency with a Gaussian fit superimposed.

produces a signals in read-out strips):

$$\varepsilon^{\eta} = \varepsilon_{gap} \cdot \varepsilon^{\eta}_{elet} \qquad \varepsilon^{\phi} = \varepsilon_{gap} \cdot \varepsilon^{\phi}_{elet} \,. \tag{6.1}$$

The quantities directly measured are ε^{η} and ε^{ϕ} and therefore is not possible to measure exactly the real gas volume efficiency ε_{gap},

If we define δ^{η} and δ^{ϕ} as the deviations from the unity of electronic efficiency $\varepsilon^{\eta}_{elet}$ and $\varepsilon^{\phi}_{elet}$:

$$\varepsilon^{\eta}_{elet} = 1 - \delta^{\eta} \qquad \varepsilon^{\phi}_{elet} = 1 - \delta^{\phi}, \tag{6.2}$$

we found that the real and the measured gap efficiency are related by:

$$\overline{\varepsilon}_{gap} = \varepsilon_{gap} \left(1 - \delta^{\eta}\delta^{\phi}\right). \tag{6.3}$$

Therefore, when $\delta^{\eta}, \delta^{\phi} \approx 0$ the approximation of $\overline{\varepsilon}_{gap}$ for ε_{gap} is reasonable (in this case δ^{ϕ} and δ^{η} are about 0.015).

The figure 6.9 shows the distribution of ATLAS RPC gas volume average efficiency, fitted with a Gaussian function, which parameters are reported in the box inside the figure. Each entry in the histogram corresponds with a single RPC gas volume. Also in this case, only RPC sectors operating with high voltage at 9.6 kV and threshold at 1 V are considered. As for the panel efficiency, a cut on the number on extrapolated tracks is applied to exclude gaps with low statistics. As

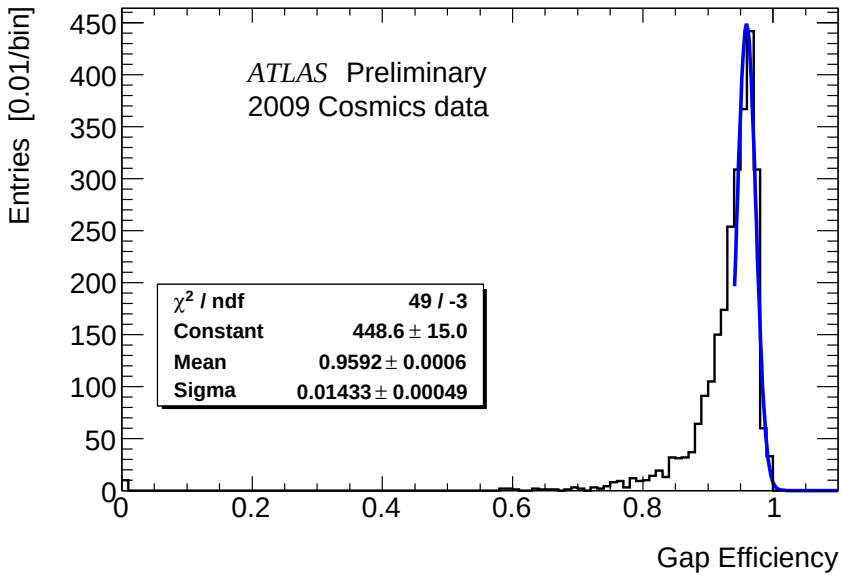

Figure 6.9: Distribution of RPC gas volume average efficiency with a Gaussian fit superimposed.

expected, because both η and ϕ signals are generated by the same avalanche, the gas volume efficiency removes some electronic inefficiency and it is greater than the panel efficiency.

From RPC efficiency, one can make a coarse estimation of the trigger efficiency. If one searches a coincidence of hits in 3 out of 4 layers, the trigger signal probability is (if ε_i is the efficiency of i-th RPC panel):

$$\varepsilon_{3/4} = \prod_{i=1\div4} \varepsilon_i + \sum_{i=1,4} \left[\Big(\prod_{\substack{j=1\div4 \\ j\neq i}} \varepsilon_j \Big) \Big(1 - \varepsilon_i \Big) \right]. \tag{6.4}$$

The formula of the trigger efficiency as function of the RPC panel efficiency is more complicated, because trigger towers not correspond to RPC chambers (one coincidence matrix can read signals coming from more than one RPC chamber, see pag. 52). Assuming that all panels have efficiency equal to average efficiency $\varepsilon_i = 94.5\%$, we can estimate a trigger efficiency (for 3/4 majority) equal to $\varepsilon_{3/4} = 98.3\%$.

In order to determine the RPC intrinsic efficiency a main issues have to be taken into account. The first one is due to the fact that the RPCs are actually providing the muon trigger thus resulting in a trigger bias on the efficiency calculation. The effect of the trigger bias has been removed from the efficiency measurement of an RPC plane by selecting all the events in which the other three

planes (in the case of a Middle Station) were producing hits, since the trigger requirement is a 3 over 4 planes majority logic.

6.2.3 Performance from off-line monitoring

The developed monitoring package analyses also RPC data to check relevant quantities such as the cluster multiplicity, the occupancy and the number of noisy hits.
RPC detector response is strictly dependent from environmental conditions [44], [46]. For this reason, due to the difference of temperature present in the ATLAS cavern, RPC detector are operated at different high voltage values as a function of y position. At the time of writing, the high voltage settings are not yet optimized, sectors 4, 5 and 6 are operated at 9400 V, whereas the other RPC sectors are operated at 9600 V. To perform an analysis over an homogeneous data sample, results presented in this section are obtained from run where all detector was at 9400 V.

RPC cluster size

Sometimes, a single discharge in the gas volume can induce a signal in more than one RPC strip (i.e. occurs a so-called *cluster*), this is due to the charge sharing and eventually to cross-talk phenomena[1]. The number of RPC strips fired in temporal coincidence is called *cluster size*. The cluster size is a relevant parameter for RPC detector and it must be strictly monitored to ensure a full trigger efficiency, it is necessary to monitor the presence of strip panels with an abnormal average cluster size, that generally is due to front-end electronic problems, rather than to avalanche discharge in the gas volume.

Figure 6.10 shows the distribution of average cluster size of all ATLAS RPC read-out strip panels, referred to 2009 December cosmics data. All panels operate at same conditions of applied high voltage (9400 V) and front-end threshold potential (1 V).

In figure 6.11 the average panel cluster size is plotted as a function of sector number. Each point in the plot represents the average of sector distributions and the error lines are the spread of the distributions.
A dependence of average cluster size on sector angular position with respect to the vertical cosmics is clearly visible. This is due to the fact that, when a charged particle cross a RPC detector not orthogonally, the charged produced by gas ionisation is greater than in case of orthogonal tracks, due to the longer pattern in gas and, mainly, because the space charge effect are reduced. A greater electric

[1] A RPC strip is large 30 mm and, between two strips, a 0.3 mm wire is interposed to reduce cross-talk phenomena.

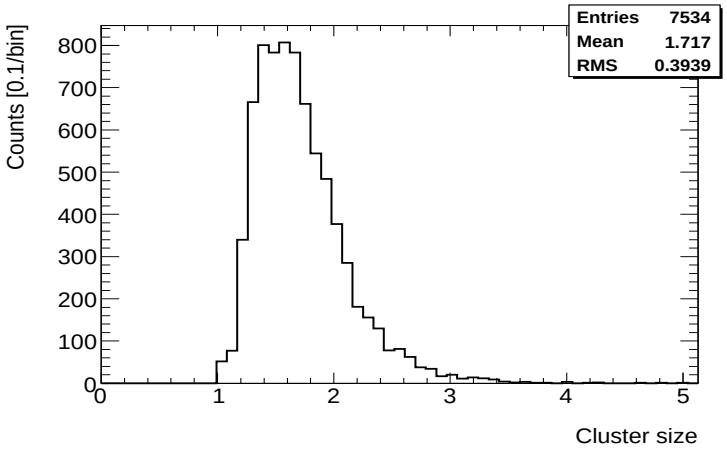

Figure 6.10: Distribution of the average cluster size of RPC strip readout panels in December 2009.

charge collected on the bakelite surface can induce a more intense signal on readout strip.

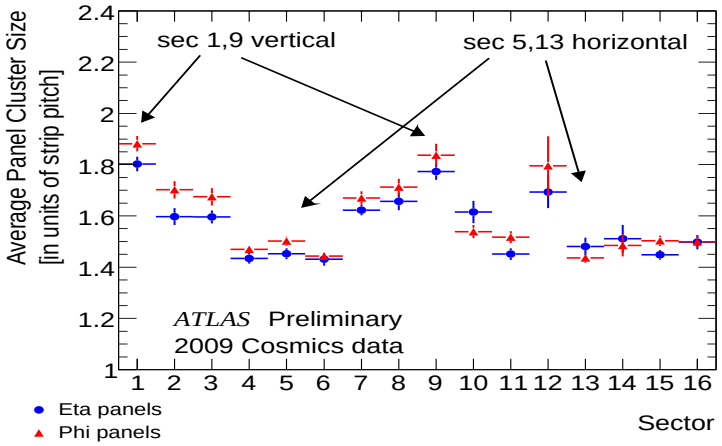

Figure 6.11: Average cluster size of RPC strip readout panels as a function of sector number showing a clear dependence with respect to track inclination. Data are separated for η and ϕ panels.

For muons coming from the interaction point (almost orthogonal to RPC surfaces of all sectors) a flat behaviour is expected with a average value close to the minimum of the present plot. Eta (Blue) and Phi (Red) panels are shown separately. Phi panels show a slightly higher cluster size than eta panels, it is expected from detector construction: an additional PET (Polyethylene-Teraphtalate) sheet is inserted in between the gas volume and the eta readout panel.

RPC Noise

Noise hits are hits that is not possible to associate to any RPC track. We define two different type of noise: the *correlated* noise and the *uncorrelated* noise. As shown in fig. 4.16, hits present in both read-out panels of the same RPC doublet and not associated to any reconstructed track, are classified as *correlated* noise, instead, isolated signals present only in one layer of the RPC doublet are defined *uncorrelated* noise.

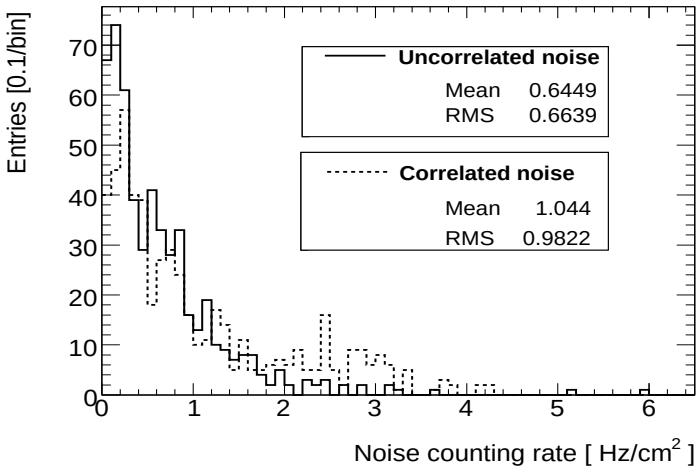

Figure 6.12: Distribution of the average correlated and uncorrelated noise counting rate per unit area of RPC strip readout panels of sector 5.

Figure 6.12 show the distribution of average noise counting rate of RPC strip read-out panels belonging to sector 5. The rate is normalized for the area of RPC read-out panels and the distributions of the two noise type are superimposed in the plot. The uncorrelated noise is directly related to the front-end electronic noise and cavern background, whereas correlated noise hits are likely produced by charged particles crossing one RPC doublet, but not the other doublets.

In the figure 6.13 is reported a map of hot points of the gas volumes (located in Pivot layer 0 of sector 13). The map is obtained by using data taken with *random* trigger.

RPC time

The time of RPC hits, in read-out data, represents the time position in the read-out window relatively to the level-1 latency. The internal CM timing is crucial for the trigger behaviour, each element of CM must be aligned, in order to generate the trigger coincidence signal. A perfect trigger alignment do not imply a good

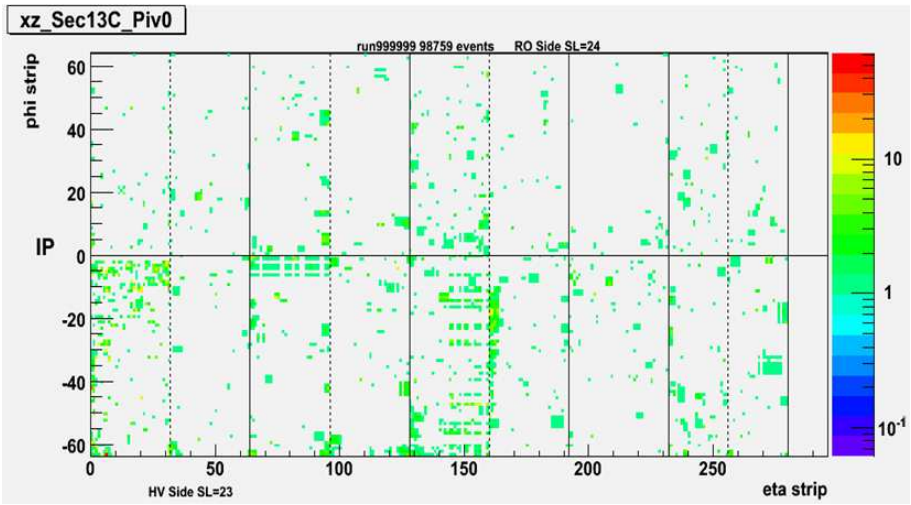

Figure 6.13: Map of the uncorrelated noise of RPC gas volumes of sector 13 side C belonging to pivot layer 0. The last two gas volume on the right were not triggered in this run.

read-out alignment, this is due to the fact that trigger and read-out data follow different path in the electronic chain. RPC monitoring package use only read-out information to plot RPC timing.

To this purpose, a dedicated section of the monitoring package checks and analyses timing data of RPC hits. Figure 6.14 shows the time distribution of RPC hits for the η (fig. 6.14(a)) and φ (fig. 6.14(b)) views. At the moment of writing, the RPC detector sections are not perfectly synchronised: the plot reflects this by showing a quite large distribution. When a final synchronisation will be optimized, all entries should stay in a 25 ns window (a bunch crossing).

When the monitoring software reconstructs a track with RPC hits, it also checks the difference of the track hit time with the average of all other track hits time. This value should be compared with the time of flight of muons between different RPC layers. When the time alignment will be completed, this check will be a valid method, for example, to monitor the fraction of fake tracks. Figure 6.15 reports the distribution of this difference, obtained from 2010 February data.

6.2.4 RPC Efficiency and Cluster Size as a function of high voltage

To optimize the RPC working parameters, the efficiency and cluster size behaviour as a function of HV was monitored. All measurements were made through the use of the offline monitoring. In this case RPC was used as trigger detector and detec-

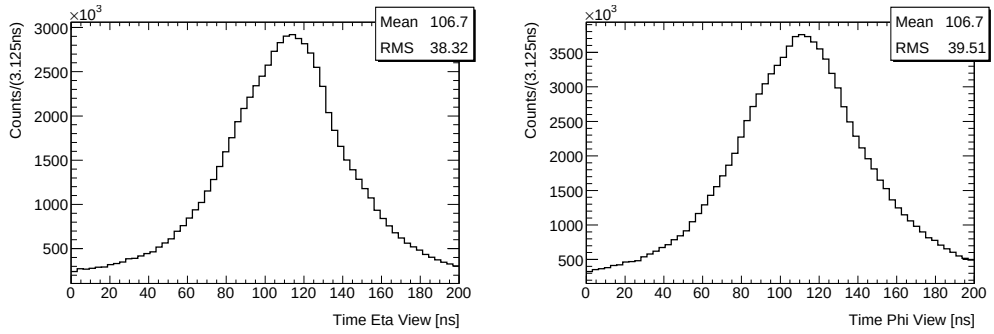

(a) η hits time distribution (b) ϕ hits time distribution

Figure 6.14: Time distribution of RPC signals in February 2010 cosmics run for η and ϕ hits.

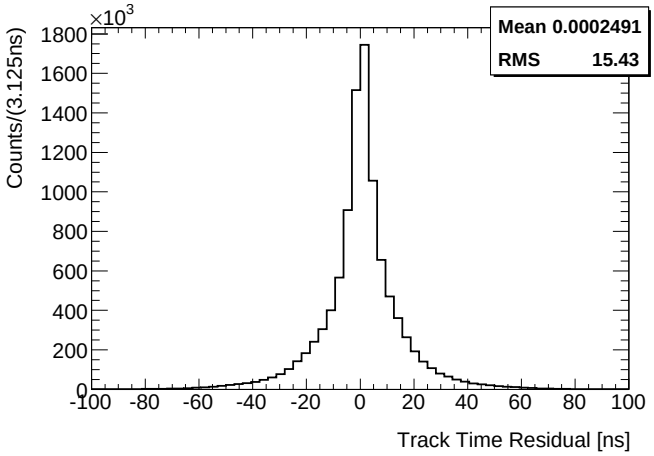

Figure 6.15: Distribution of the differences between hit time and the average time for hits of the same track. Values are not corrected for the time of flight.

tor under measurements. In order to not introduce a bias in the measure due to the trigger selection, during the track reconstruction the layer under measurements was removed and hits in at least 3 layers are always required.

Figure 6.16 shows an example of this measurement: the RPC detection efficiency as a function of HV for two readout panels of separated views faced to the same gas volume. The data are cosmics taken with magnetic field on. The front-end discrimination threshold was set at the standard value of V_{th}=1 V. The gas volume efficiency, as calculated in paragraph 6.2.2, as a function of HV is shown in figure 6.17.

All curves were fitted with the following equation:

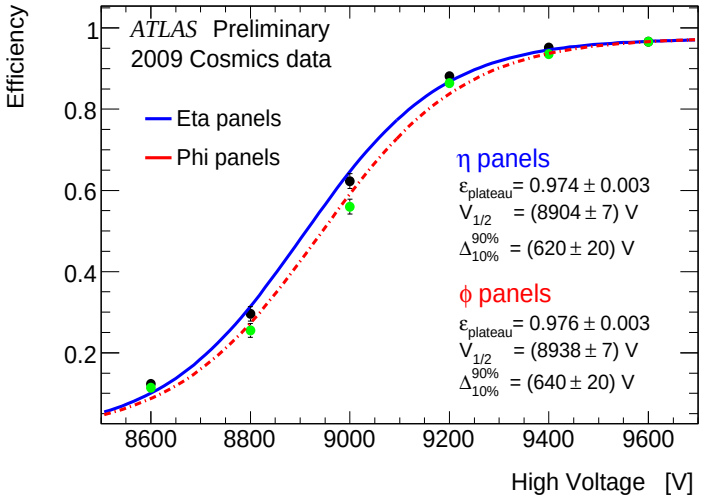

Figure 6.16: RPC average detection efficiency of two orthogonal strip readout panels of the same gas volume as a function of the applied high voltage.

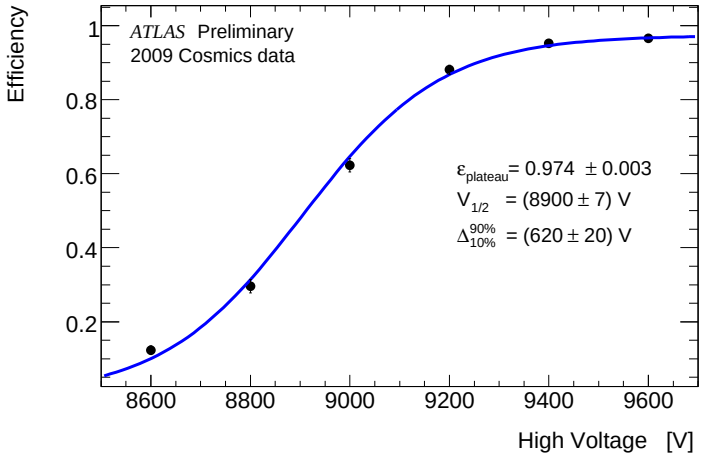

Figure 6.17: RPC average gas volume efficiency as a function of the applied high voltage.

$$\varepsilon(V) = \frac{\varepsilon_{plateau}}{1 + 81^{\frac{V_{1/2}-V}{\Delta_{10}^{90}}}} \quad , \tag{6.5}$$

where $\varepsilon_{plateau}$ is the efficiency reachable for infinite value of HV, $V_{1/2}$ is the voltage values at half value of maximum efficiency and Δ_{10}^{90} measures the voltage difference between the values at 90% efficiency and 10% efficiency.

In order to characterize the performance of the ATLAS RPC, the distributions of the parameters of the curve used to approximate the efficiency as a function of HV were plotted in figure 6.18.

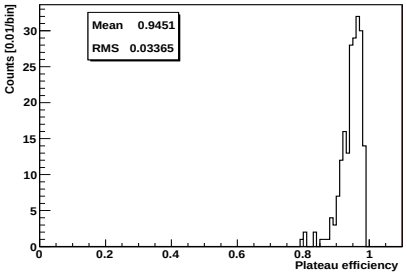

(a) Distribution of plateau efficiency.

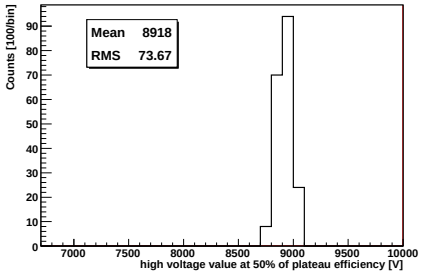

(b) Distribution of high voltage value at 50% of plateau efficiency.

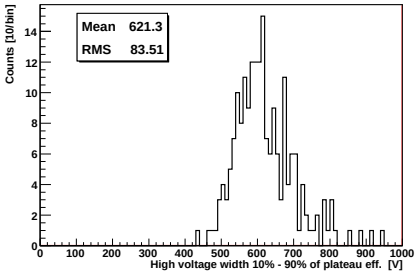

(c) Distribution of high voltage width value at 10% and 90% of plateau efficiency.

Figure 6.18: Distributions of the three parameters of equation 6.5 obtained by fitting RPC strip readout panel efficiency plateau curve like in figure 6.16.

As for the efficiency, also the behaviour of Cluster Size was monitored as a function of HV. As show in figure 6.19, the average Cluster Size increases with voltage reaching an average value of about 1.6 for a voltage of 9600 V. This value was obtained with cosmic data and only for readout panels with the front-end discrimination threshold set at the standard value of V_{th}=1 V.

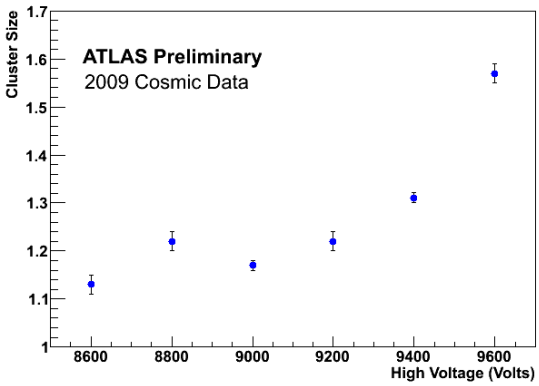

Figure 6.19: Average cluster size of a RPC strip readout panel as a function of the applied high voltage.

6.3 Studies with beam data

6.3.1 Beam collimator scraping events

On the 10-th of September 2008 the first events produced by single proton beams circulating in the LHC were recorded with the ATLAS detector. In those days, just before the 20-th of September LHC disastrous uncontrolled superconducting magnet quenching between sector 4 and 5, RPC detector coverage were about 70%. Instead, after the LHC recovery, on 20-th November 2009, RPC detector coverage reached about 99% coverage and the new colliding beams on collimators were very useful to complete the commission of the RPC detector for operation before collisions and to perform important tasks such as detector time alignment, channel mapping, etc. Selected examples of this colliding beam will be briefly described in this Section.

For reasons of detector safety, during the 2008 beam splash period the RPC were operated at a high voltage value of 9200 V. From this first experience was possible to assure that RPC could be operated safely during these events. In fact, in the second beam splash period of November 2009, the RPC detector were operated at the nominal high voltage value of 9600 V.

These so-called beam splash events were produced by colliding the protons on the closest collimators located at 140 m upstream and down stream of the ATLAS detector. These collisions generated a large quantity of particles reaching all parts of ATLAS and illuminating the whole detector at once (a schematic representation is shown in figure 6.20).

As an example, figure 6.21 shows the spatial correlation between eta and phi hits firing on the middle station of RPC detector during a “beam splash” event hit-

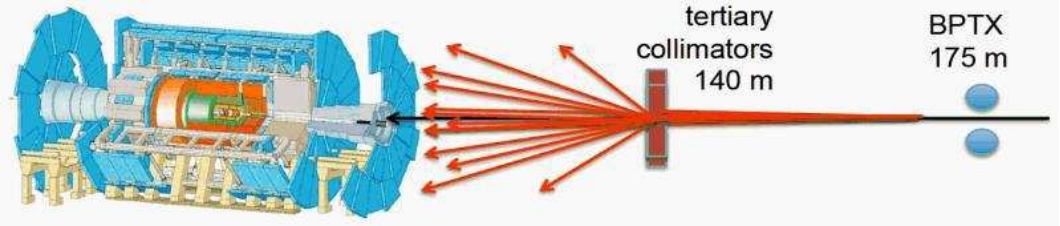

Figure 6.20: Schematic representation of a "beam splash" event produced in the ATLAS detector by beam induced collimator scraping.

ting the whole volume of the ATLAS detector. In this event, the beam was coming from the right side and an attenuation along the negative z axis direction is clearly visible due to the particle flux absorption by ATLAS material. In particularly, in the region near the feet the particle flux absorption is even more pronounced with respect to the other parts. In fact, the most massive objects traversed by the muons are around the ATLAS feet.

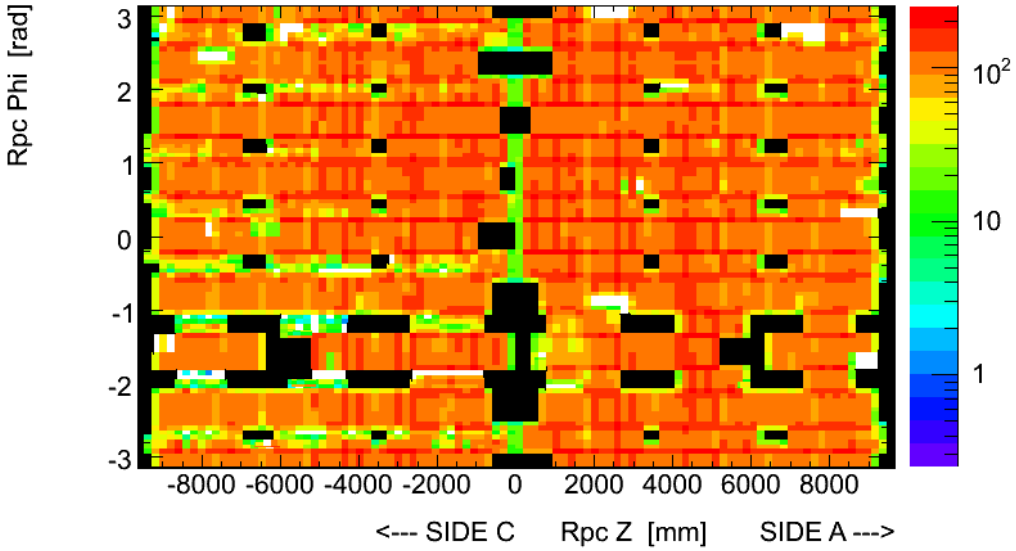

Figure 6.21: RPC hit map during a "beam splash" event in December 2009 with single beam from side A.

Important information for the detector start-up can be extracted from such events. For example, the timing setting for each channel of the electronics readout, determined beforehand from cable length and from cosmic rays, can be compared to those obtained from the beam-splash particles. The large amount of secondary particles produced by interactions of protons with collimators and traversing the

detector allows to have an instantaneous snapshot of the overall detector, after time of flight correction. Since the incident particles had a direction almost parallel to the beam axis, they crossed many detector elements and were very useful for synchronization of the individual RPC readout units.

These comparisons are shown in Figure 6.22 where the different points correspond to the arrival timing of different eta view readout channel along the z-axis for single beams coming from the two opposite direction.

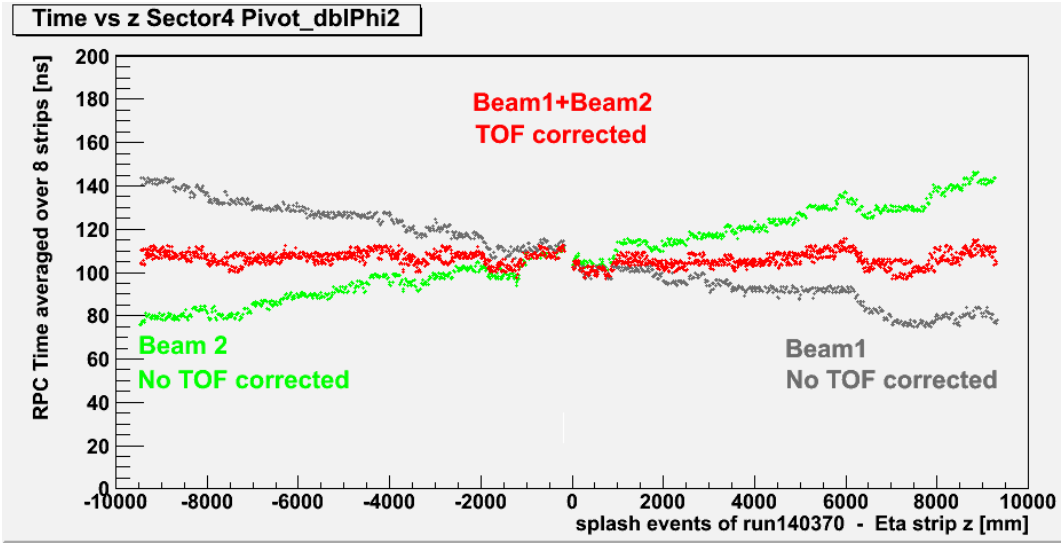

Figure 6.22: RPC average eta strip time versus z position during "beam splash" events in December 2009. The three scatter plots correspond to beam 1 events, beam 2 events and beam 1+ plus 2 events with time of flight corrections.

After corrections for the different time-of-flights expected for beam-splash events, the predictions for the two beams overlap with a precision better than 5 ns. The same is true for the Outer stations where within each section, the timing results are also uniform to better than 5 ns. It is also possible to observe few station not yet properly aligned in time showing that the RPC timing was still under finalization. The beam splash events were important in order to spot these not perfectly time aligned RPC trigger towers.

Finally, verification of operational stability were also possible analysing and comparing different beam splash events. In Figure 6.23 the distribution of the number of RPC hits per beam splash for all of them is shown. It is possible to see how the number of hits fluctuation is compatible with the statistical variation and with an average occupancy of about 90 %.

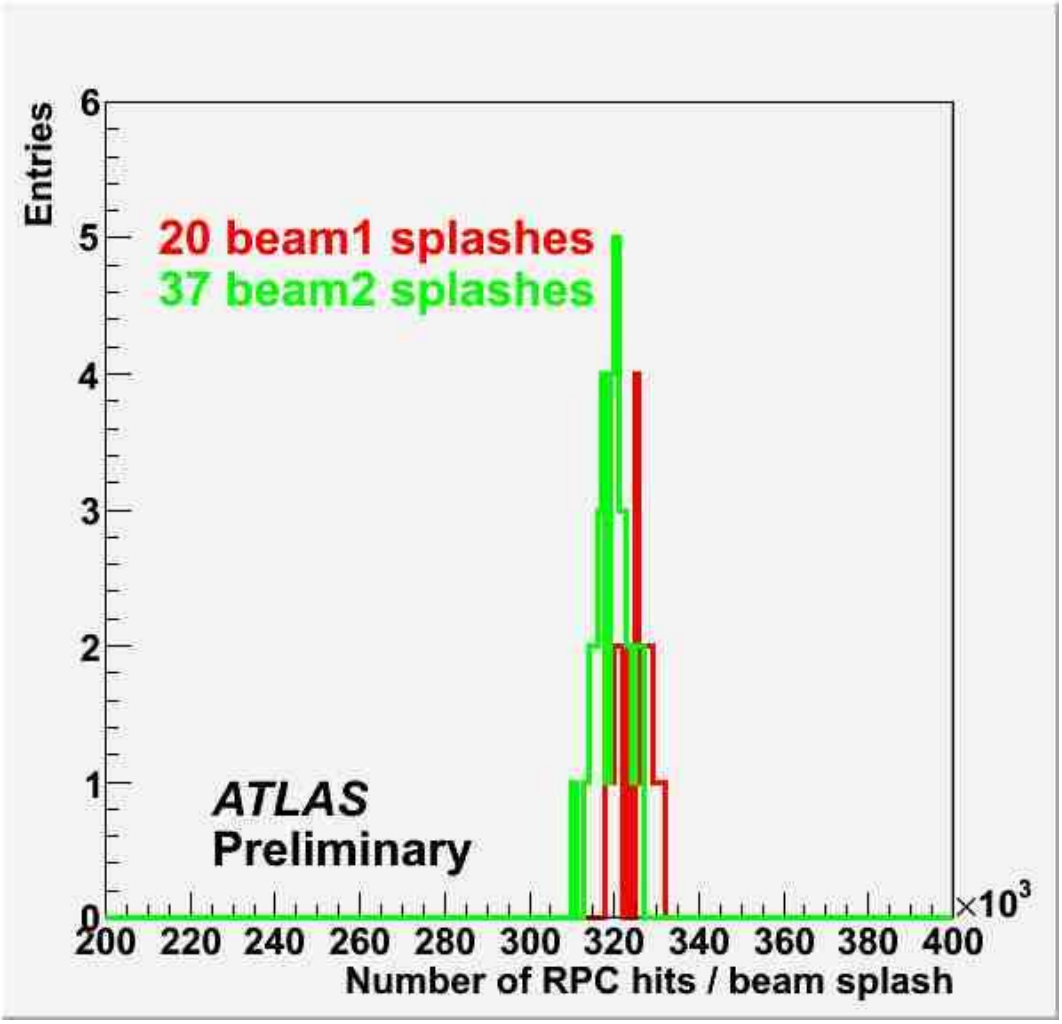

Figure 6.23: RPC hit multiplicity distribution during "beam splash" events in December 2009.

6.3.2 Beams collisions

This section briefly illustrate the RPC response during the December 2009 proton-proton collisions at 0.9 TeV centre of mass energy.

The spectrometer identification algorithms were optimized, for the reconstruction of high-p_T prompt muons and the rejection of the soft components which are dominant in the sample collected at 0.9 TeV. The MDTs, TGCs and RPCs were all operating normally during beam collisions.

The algorithms used for muon reconstruction combine tracks from the muon systems and the inner detector, but for the results presented here, two indepen-

dent algorithms are used and only candidates selected by both are accepted. The kinematic distributions for these candidates are presented in 6.24.

The muon spectrum observed is soft and strongly peaked in the forward direction, where the momentum is significantly higher for a given p_T and more easily exceeds the average energy loss in the calorimeters of about 3.2 GeV. The obtained kinematic distributions are compared to the predictions from minimum bias simulation with the Monte Carlo normalized to the number of muons found in data. Within the large statistical uncertainties good agreement is found indicating a reasonable understanding of the initial performance of the ATLAS muon spectrometer [47].

The momentum range is problematic for the muon trigger, whose acceptance is limited for muons in this low p_T region, especially in the barrel region. Nevertheless, a clear correlation could be seen between RPC trigger hits in the η and ϕ view and the muon track reconstructed by the inner detector alone. This correlation is reported in the Figure 6.25.

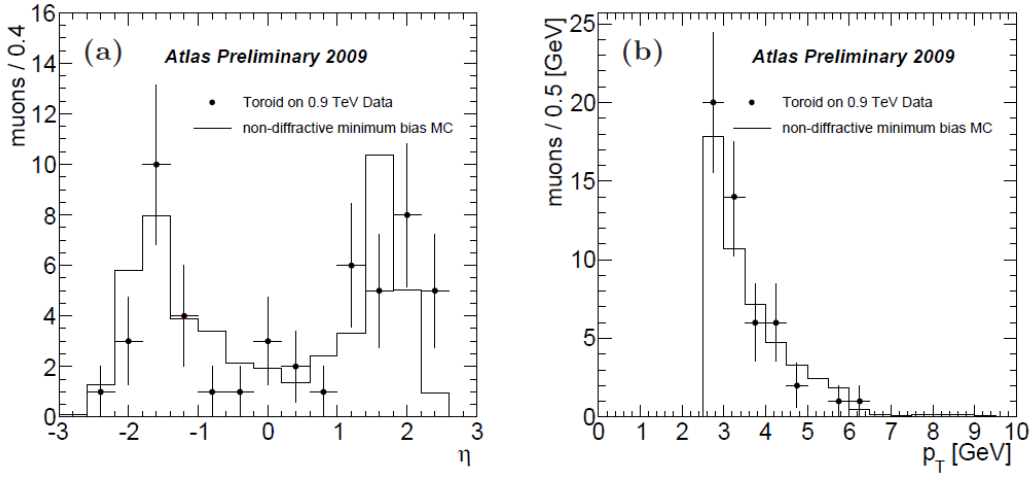

Figure 6.24: The distribution of eta and pt of reconstructed muons in December 0.9 TeV collisions in data and simulation.

In April 2010 LHC started its first long term run at half design energy of 7 TeV centre of mass energy accumulating integrated luminosity up to few fb^{-1} until the end of 2011. The ATLAS detector early data analysis will consist in "re-discovering" standard model physics in order to calibrate and extract detector efficiency and performance from real data. The most important particle 'candle' for the muon spectrometer and the electromagnetic calorimeter is the Z boson decaying in muons and electrons respectively and, in general, charmonium and bottomonium resonances. During the writing of this thesis the accumulated integrated luminosity is about an order of magnitude too low to detect the Z boson in

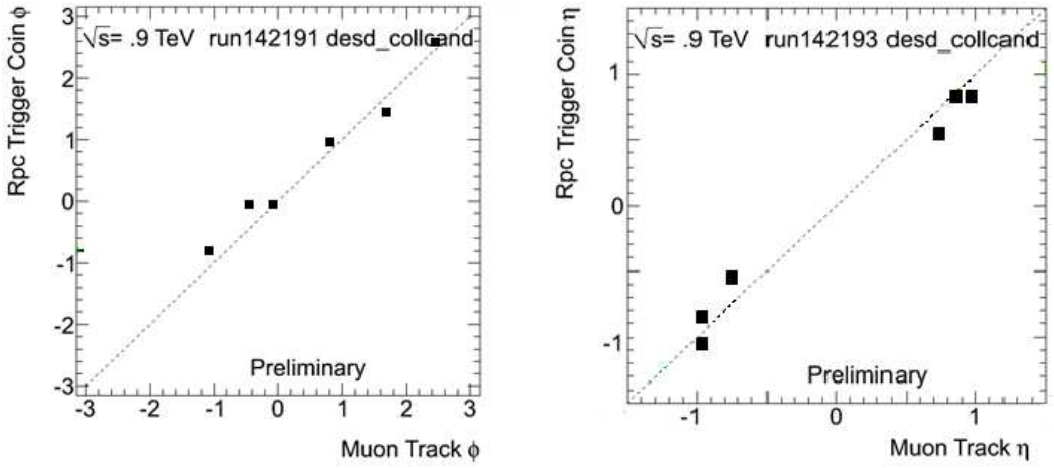

Figure 6.25: Azimuthal correlation (a) and in pseudo-rapidity (b) between RPC trigger hits and inner detector tracks in a sub-sample of December 2009 collisions at 0.9 TeV centre of mass energy.

one of the lepton channels taking into account also background suppression cuts. Nevertheless, this allows for about one W boson event in one vent in both leptons channel. In fact, a W boson candidate for the muon and for the electron channel was recorded. In Figure 6.26 the first W boson candidate in the muon channel is shown with two different visualization packages. The clear W signature is evident in this event display: in the transverse plane a back-to-back muon and missing energy of about one third of the W mass.

6.4 Conclusions

The end of the installation of the ATLAS RPC detector in August 2008 was followed by a period of commissioning and calibration with cosmics in 2008 and 2009.

During this period the detector took data with high efficiency first with cosmic rays then finally with LHC single beams and collisions. These data allowed full tests of trigger, data-acquisition, and reconstruction algorithms and monitor the system. Many detector properties were measured such as: occupancy, efficiency, cluster size and noise. The different RPC detector modules were timed in with a precision of few nsec inside modules and of few bunch-crossing between modules.

The observed performance on this early data showed that the ATLAS RPC Detector is fully operational and will provide high-quality triggering and tracking for LHC collisions.

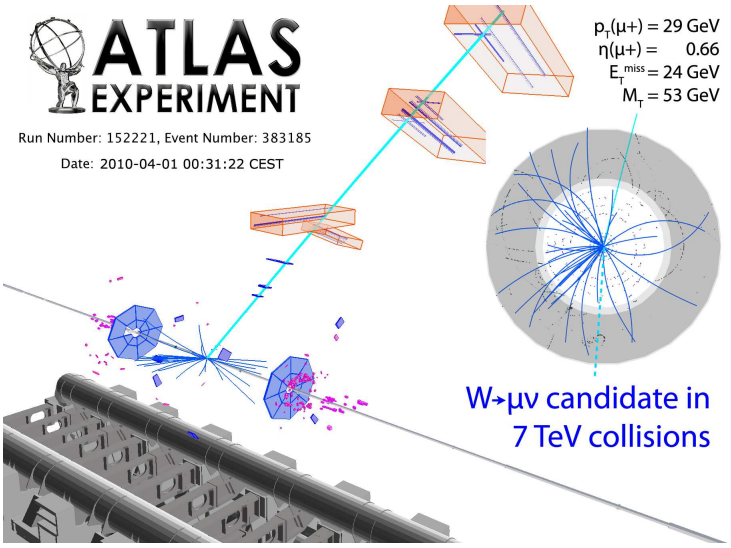

(a) Event display from VP visualization package.

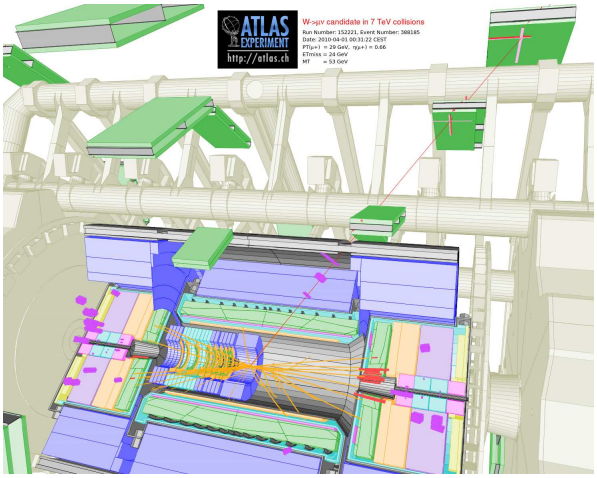

(b) Event display Persint visualization package.

Figure 6.26: Event display of the first W boson muon-neutrino decay candidate found in April 2010 7 TeV collisions leaving a clear muon track in the Muon Spectrometer and transverse missing energy in the calorimeter. The two pictures correspond to the same event represented graphically by two different visualization software.

Summary and Outlook

ATLAS is a general purpose experiment designed to discovery new phenomena at the proton-proton collisions of the Large Hadron Collider built at CERN in Geneva. The ATLAS collaboration designed and built a high performance Air Core Toroidal Muon Spectrometer, in order to minimize the muon multiple scattering. In the barrel region of the Muon Spectrometer Resistive Plate Chambers (RPCs) are used as trigger detectors. The RPC detector was installed and operated during the last three years. The deep knowledge of the 4000 m^2 RPC detector and the complete control and understanding of its performances are essential to provide a reliable muon trigger.

For this work thesis a versatile software was developed to provide a detailed detector monitoring, to perform an accurate detector characterization and to asses detector data quality. The RPC off-line monitoring covers basic aspects of the ATLAS RPC detector, such as: electronics channels and readout strip response, standalone tracking capability, trigger related quantities (timing, trigger coincidence pattern and trigger road) and correlations between trigger and tracking chambers. In addition, main RPC detector performances, such as: efficiencies, cluster multiplicity, residuals and noise, are measured without relying on the full ATLAS reconstruction.

A big effort was also devoted to develop a coherent Data Quality framework based on the information provided by the RPC off-line monitoring. Data quality is a crucial issue for detector maintenance and physics analysis.

RPC Data Quality is done both in the on-line and off-line monitoring. This thesis is focused on RPC off-line Data Quality. The RPC off-line Data Quality framework perform checks mainly on the following quantities:

- Trigger Coverage
- Detection efficiency
- Cluster multiplicity
- Noise level
- Time alignments

- Stability

Automatics quality checks are based on histograms and applying specific algorithms. To allow an easy and fast data quality evaluation, the histograms and algorithm results are displayed on-line by a common ATLAS framework based on dynamic web pages. A subset of dynamic pages specific to RPC detector was realized in this work thesis. This allowed also to store automatically the RPC Data Quality flags in the common ATLAS Database.

Finally the analysis of RPC cosmic data collected at the end of the commissioning phase is also presented together with the first beam scraping test and collisions events. In particular, a complete detector efficiency scan is shown in great details and the best working point "in situ" found. The results of these studies shown the good performance of the RPC detector as muon trigger in the LHC environment with high coverage, high efficiency and low noise.

Bibliography

[1] F. Halzen and A. D. Martin. *QUARKS AND LEPTONS: an introductory course in modern particle physics*. John Wiley and Sons, New York, 1984.

[2] C. Amsler et al. (Particle Data Group). The Review of Particle Physics. *Physics Letters*, B667, 2008.

[3] S. L. Glashow. Partial Symmetries of Weak Interactions. *Nucl. Phys.*, 22:579–588, 1961.

[4] P. W. Higgs. BROKEN SYMMETRIES AND THE MASSES OF GAUGE BOSONS. *Phys. Rev. Lett.*, 13:508–509, 1964.

[5] C. Amsler et al. (Particle Data Group). The Review of Particle Physics. *Physics Letters*, B667, 2008.

[6] V.M. Abazov et al. A combined search for the standard model higgs boson at $\sqrt{s} = 1.96$ TeV. *Physics Letters B*, 663(1-2):26 – 36, 2008.

[7] Combined CDF and D0 Upper Limits on Standard Model Higgs- Boson Production with 2.1 - 5.4 fb-1 of Data. 2009.

[8] CERN. *oai:cds.cern.ch:1021125. PHYSTAT-LHC Workshop on Statistical Issues for LHC Physics*, Geneva, 2008. CERN.

[9] *ATLAS detector and physics performance: Technical Design Report, 2*. Technical Design Report ATLAS. CERN, Geneva, 1999. Electronic version not available.

[10] J. F. Gunion, Howard E. Haber, and C. Kao. Searching for the cp-odd higgs boson of the minimal supersymmetric model at hadron supercolliders. *Phys. Rev. D*, 46(7):2907–2917, Oct 1992.

[11] D. Cavalli, D. Froidevaux, F. Gianotti, L. Poggioli, S. Resconi, and E. Richter-Was. Minimal supersymmetric standard model higgs rates and backgrounds in atlas. Technical Report ATL-PHYS-96-074. ATL-GE-PN-74, CERN, Geneva, Apr 1996.

[12] E. Richter-Was and D. Froidevaux. Mssm higgs bosons in sugra model: observability in sm decay modes with atlas. Technical Report ATL-COM-PHYS-98-012, Nov 1998.

[13] T. S. Pettersson and P. Lefèvre. The large hadron collider: conceptual design. oai:cds.cern.ch:291782. Technical Report CERN-AC-95-05 LHC, CERN, Geneva, Oct 1995.

[14] The ATLAS collaboration. The ATLAS Experiment at the CERN Large Hadron Collider. *JINST*, 3:S08003, 2008.

[15] *ATLAS magnet system: Technical Design Report, 1*. Technical Design Report ATLAS. CERN, Geneva, 1997.

[16] *ATLAS inner detector: Technical Design Report, 1*. Technical Design Report ATLAS. CERN, Geneva, 1997.

[17] S. Haywood, L. Rossi, R. Nickerson, and A. Romaniouk. *ATLAS inner detector: Technical Design Report, 2*. Technical Design Report ATLAS. CERN, Geneva, 1997.

[18] M. S. Alam et al. The atlas silicon pixel sensors. *Nuclear Instruments and Methods in Physics Research Section A: Accelerators, Spectrometers, Detectors and Associated Equipment*, 456(3):217 – 232, 2001.

[19] *ATLAS liquid-argon calorimeter: Technical Design Report*. Technical Design Report ATLAS. CERN, Geneva, 1996.

[20] *ATLAS tile calorimeter: Technical Design Report*. Technical Design Report ATLAS. CERN, Geneva, 1996.

[21] ATLAS Muon Collaboration. Atlas muon spectrometer technical design report. 1997.

[22] *ATLAS detector and physics performance: Technical Design Report*. Technical Design Report ATLAS. CERN, Geneva, 1999.

[23] W. Blum. High-recision drift tubes. Technical Report ATL-MUON-93-024. ATL-M-PN-24, CERN, Geneva, Jul 1993.

[24] N. C. Benekos, D. G. Drakoulakos, C. W. Fabjan, V. P. Falaleev, Z. Krumshtein, F. Lejal, J. M. Maugain, S. Rangod, F. Rohrbach, Y. V. Sedykh, and L. S. Vertogradov. Xtomo2, stereo-measurements of the mdt muon chambers using a high precision x-ray tomograph. Technical Report ATL-MUON-97-155. ATL-M-PN-155, CERN, Geneva, Apr 1997.

[25] V. Paschhoff and M. Spegel. Ageing studies for the atlas mdt's using ar-co2 90-10. Technical Report ATL-MUON-2000-004, CERN, Geneva, Jun 1999.

[26] M. Dikken. The rasnik in-plane alignment system. Technical Report ATL-MUON-97-184. ATL-M-PN-184, CERN, Geneva, 1997.

[27] E. Duchovni, T. Kobayashi, D. Lellouch, L. Levinson, N. Lupu, T. Mashimo, G. Mikenberg, and M. Shoa. Possible utilization of thin-gap chambers in the atlas muon system. Technical Report ATL-MUON-93-023. ATL-M-PN-23, CERN, Geneva, Jun 1993.

[28] K. Nagai. Thin gap chambers in ATLAS. *Nucl. Instrum. Meth.*, A384:219–221, 1996.

[29] V. Smakhtin. Testing TGC detectors in a high rate environment. *Nucl. Instrum. Meth.*, A494:500–503, 2002.

[30] R. Santonico and R. Cardarelli. Development of resistive plate counters. *Nuclear Instruments and Methods*, A(377):187, 1981.

[31] R. Cardarelli, V. Makeev, and R. Santonico. Avalance and streamer mode operation of resistive plate chambers. *Nuclear Instruments and Methods*, 1996.

[32] G. Aielli, P. Camarri, R. Cardarelli, A. Di Ciaccio, L. Di Stante, B. Liberti, A. Paoloni, E. Pastori, and R. Santonico. Test of atlas rpcs front-end electronics. *Nuclear Instruments and Methods in Physics Research Section A: Accelerators, Spectrometers, Detectors and Associated Equipment*, 508(1-2):189 – 193, 2003. Proceedings of the Sixth International Workshop on Resistive Plate Chambers and Related Detectors.

[33] F. Giannini, E. Limiti, G. Orengo, and R. Cardarelli. An 8 channel GaAs IC front-end discriminator for RPC detectors. *Nuclear Instruments and Methods in Physics Research Section A: Accelerators, Spectrometers, Detectors and Associated Equipment*, 432(2-3):440 – 449, 1999.

[34] *ATLAS computing: Technical Design Report*. Technical Design Report ATLAS. CERN, Geneva, 2005.

[35] G. Barrand et al. Gaudi – a software architecture and framework for building hep data processing applications. *Computer Physics Communications*, 140(1-2):45 – 55, 2001.

[36] P. Jenni, M. Nessi, M. Nordberg, and K. Smith. *ATLAS high-level trigger, data-acquisition and controls: Technical Design Report*. Technical Design Report ATLAS. CERN, Geneva, 2003.

[37] A. Corso-Radu, S. Kolos, H. Hadavand, R. Kehoe, and M. Hauschild. Data quality monitoring framework for the atlas experiment at the lhc. Technical Report ATL-DAQ-CONF-2008-006. ATL-COM-DAQ-2007-033, CERN, Geneva, Oct 2007.

[38] *ATLAS level-1 trigger: Technical Design Report*. Technical Design Report ATLAS. CERN, Geneva, 1998.

[39] V. Bocci, E. Petrolo, A. Salamon, R. Vari, and S. Veneziano. The design of the coincidence matrix asic of the atlas barrel level-1 muon trigger. 2002.

[40] N. Benekos, M. Bianco, G. Chiodini, I. A. Christidi, J. Coggeshall, A. Cortes-Gonzalez, E. Gorini, D. Fortin, J. Griffiths, A. Guida, et al. Muon offline monitoring at tier0 using cosmics and fdr data. Technical Report ATL-COM-MUON-2009-042, CERN, Geneva, Nov 2009.

[41] M. Baak, C. Guyot, M. Hauschild, R. Hawkings, B. Heinemann, A. Hocker, M. Martínez-Pérez, D. Malon, P. Onyisi, and E. Torrence. Data quality status flags and good run lists for physics analysis in atlas. Technical Report ATL-COM-GEN-2009-015, CERN, Geneva, Mar 2009.

[42] A. Corso-Radu, S. Kolos, H. Hadavand, R. Kehoe, and M. Hauschild. Data quality monitoring framework for the atlas experiment at the lhc. Technical Report ATL-DAQ-CONF-2008-006. ATL-COM-DAQ-2007-033, CERN, Geneva, Oct 2007.

[43] L. W. Alvarez. A proposal to "X-Ray" the egyptian pyramids to search for presently unknown chambers. *LBNL Physics notes, 544*, 1965.

[44] M. Bianco. *ATLAS RPC certification and commissioning with cosmic rays*. PhD thesis, Lecce University, 2007.

[45] G. Chiodini et al. Rpc cosmic ray tests in the atlas experiment. *Nuclear Instruments and Methods in Physics Research Section A: Accelerators, Spectrometers, Detectors and Associated Equipment*, 581(1-2):213 – 216, 2007. VCI 2007 - Proceedings of the 11th International Vienna Conference on Instrumentation.

[46] M. Bianco, G. Chiodini, E. Gorini, F. Grancagnolo, R. Perrino, M. Primavera, and S. Spagnolo. Temperature dependent performance of ATLAS RPC. *Nuclear Physics B Proceedings Supplements*, 158:204–207, August 2006.

[47] G. Aad et al. Charged-particle multiplicities in pp interactions at $\sqrt{s}$ = 900 GeV measured with the ATLAS detector at the LHC. 2010.